2013

The Design and Validation of a Computational Rigid Body Model for Study of the Radial Head

Cassandra Woodcock
Virginia Commonwealth University

THE DESIGN AND VALIDATION OF A COMPUTATIONAL RIGID BODY MODEL FOR STUDY OF THE RADIAL HEAD

A Thesis submitted in partial fulfillment of the requirements for the degree of Master of Science in Biomedical Engineering at Virginia Commonwealth University

by

CASSANDRA ALAN WOODCOCK
B.S. Biomedical Engineering, Virginia Commonwealth University, 2009

Director: JENNIFER S. WAYNE, Ph.D.
Departments of Biomedical Engineering & Orthopaedic Surgery

Virginia Commonwealth University
Richmond, Virginia
December, 2013

ACKNOWLEDGEMENTS

Much gratitude is due to a number of people whose support has made this thesis possible. First and foremost I thank Dr. Jennifer Wayne for providing me the opportunity to work in the Orthopaedic Research Laboratory. Her guidance, patience, and tireless time and direction have been priceless in the development of this research. Her mentorship not only in graduate school but also in my undergraduate studies helped guide me throughout my years at VCU. My lab mates in the Orthopaedic Research Lab also provided me with keen insight, many laughs, and an addiction to caffeine. For that, special thanks are extended to Meade Spratley, Ruchi Chande, Sean Higgins, Erika Matheis, Afsarul Mir and Johnny Owen.

This journey would not have been complete without the love of my family and friends, whose steadfastness supported me outside of academia. Thank you to my parents Alan and Tammy as well as my sister Katey for their lifelong enthusiasm for my education, encouraging me through successes as well as frustrations. They have been constant supporters of each and every endeavor, and for that I am always grateful. I am also thankful for my close friends who encouraged me, offered advice, and occasionally provided a much-needed distraction; they go beyond the call of duty regularly and teach me often the true meaning of friendship. Finally, I thank my boyfriend Kendall for his patience and wisdom, his soft shoulder and the occasional late-night dinner delivery to the lab. He has always seen more in me that I could possibly see in myself and I push daily to live up to the person he believes me to be. Without the blessing of these incredible people in my life, I could never have reached this goal.

TABLE OF CONTENTS

List of Tables

List of Figures

Abstract

THE DESIGN AND VALIDATION OF A COMPUTATIONAL RIGID BODY MODEL

FOR STUDY OF THE RADIAL HEAD

By Cassandra Alan Woodcock, B.S.

A Thesis submitted in partial fulfillment of the requirements for the degree of Master of Science in Biomedical Engineering at Virginia Commonwealth University

Virginia Commonwealth University, 2013

Director: Jennifer S. Wayne, Ph.D.
Professor, Biomedical Engineering & Orthopaedic Surgery
Director, Orthopaedic Research Laboratory

Rigid body modeling has historically been used to study various features of the elbow joint including both physical and computational models. Computational modeling provides an inexpensive, easily customizable, and effective method by which to predict and investigate the response of a physiological system to in vivo stresses and applied perturbations. Utilizing computer topography scans of a cadaveric elbow, a virtual representation of the joint was created using the commercially available MIMICS™ and SolidWorks™ software packages. Accurate 3D articular surfaces, ligamentous constraints, and joint contact parameters dictated motion. The model was validated against two cadaveric studies performed by Chanlalit et al. (2011, 2012) considering monopolar and bipolar circular radial head replacements in their effects on radiocapitellar stability and respective reliance upon lateral soft tissues, as well as a comparison of these with a novel anatomic radial head replacement system in an elbow afflicted with the “terrible triad” injury. Rigid body simulations indicated that the

computational model was able to accurately recreate the translation of forces in the joint and demonstrate results similar to those presented in the cadaveric data in both the intact elbow and in unstable injury states. Trends in the resulting data were reflective of the average behavior of the cadaveric specimens while percent changes between states correlated closely with the experimental data. Information on the transposition of forces within the joint and ligament tensions gleaned from the computational model provided further insight into the stability of the elbow with a compromised radial head.

1. INTRODUCTION

1.1. Overview of Computational Modeling

Biomechanical function of the musculoskeletal system relies upon multiple physiological components, including articular anatomy, ligamentous constraints, and muscle activation. Classically, biomechanical research has focused on the utilization of cadaver tissues to study these components as well as the effects of joint repair procedures. Through hardware advances and the development of sophisticated software, computational modeling has become increasingly popular for the study of these features to further understand and characterize joint function. Computational techniques provide repeatability, preservation of resources, and a method to quantify parameters difficult or impossible to measure experimentally. They also allow for simultaneous measurement of myriad physiological entities. Once these models are validated against experimental results, they may be utilized to not only further understand joint mechanics, but also to study surgical techniques, develop individualized rehabilitation strategies and implantable devices, and study functional changes resulting from traumas, pathologies, or implantable devices.

Currently, two primary methods of computational modeling have been accepted as comparable to experimental data: continuum finite element analysis (FEA) and rigid body modeling (RBM). Though

both are robust tools for modeling with various strengths, traditionally one option is chosen over the other depending on the desired quantifiable elements.

Continuum finite element analysis has a long history of solving problems in various engineering fields including biomedical engineering and musculoskeletal biomechanics. FEA involves defining a region of interest or geometry whose mechanical behavior is governed by explicit conservation statements (i.e. conservation of mass, conservation of linear momentum, etc). This region of interest is subdivided into individual tetrahedral bodies, or elements, which are connected to one another through nodal points. Element properties and boundary parameters, including experimentally-derived material properties such as stiffness, are assigned to each element [1]. The unknown parameters, or field variables, of the problem (i.e. displacement or pressure) are assigned to each nodal point and assembled into an array of field variables that must be solved. FEA has been used recently to observe the force distribution and contact stresses of loaded joints, as well as implantable devices [2–6]. However, due to the lengthy processing time required to compute unknowns, these models have been described as sometimes too complex [7] when observing a large number of variables in a study. This can at times become prohibitive in biomechanical computational modeling.

Rigid body modeling is a versatile method of simulating joint kinematics that presents main bodies of the model as both inelastic and incompressible, thus prohibiting deformations. This is an approximate methodology for kinematics research because of the tissue's inherent high stiffness, and is ideal in situations when bone stress computations are not the desired outcome. Recently in the literature, rigid body modeling and FEA have been combined for a more thorough description of joint function [5]. However, difficulties remain in integrating both techniques, including the collection of all physiologic and morphometric data such as segment lengths and muscle moment arms about joints [8,9].

RBM is seen frequently in literature to both measure ligament and surface forces as well as to predict motion [3,6,10–13]. These studies utilize computed topography (CT), magnetic resonance imaging (MRI), or laser scans to derive their simulations, and sometimes employ a user interface that allows easy manipulation of a model to simulate geometries and model parameters to recreate a variety of procedures. Though containing highly advanced features, many disregard the effects of ligaments and their respective in situ strains. Even those that account for viscoelastic ligament properties often rely upon simplified joint approximations, such as simple hinges to simulate the elbow, thereby constraining the possible degrees of freedom to idealized situations [13]. Others only employ inverse dynamics, a methodology in which a particular kinematic parameter (e.g. angle of flexion/extension or pronation/supination) is applied and the resultant stabilizing forces are measured accordingly [14]. These modifications affect the complexity and accuracy of the model, while undermining the results as they would be applied in a clinical setting.

In comparison, some of the most recent RBM examples are implementing models which do not idealize joint motion, but allow 3D articular anatomy, ligamentous constraints, muscle forces, and external perturbations to dictate overall biomechanical function [12,15–20]. These models utilize a modeling approach that can simulate almost any joint condition, including osteotomies, fixation devices, prostheses, and ligament or bone injury. Liacouras' early research using rigid body modeling in this manner considered the lower extremity. Despite software limitations, this lower leg computational model accurately reflected the results of two distinct cadaveric studies, including syndesmotic injury and repair and a post-ligament transection ankle inversion. Data also reflected in vivo force re-distributions following injury and showed the predictive nature of RBM [18]. This methodology has been since updated and modified for further research on the elbow, shoulder, wrist, and ankle [15,16,19–21].

1.2. Rigid Body Modeling of the Elbow

Rigid body modeling has been used to study various features of the elbow joint including both physical and computational models. Lemay et al. designed a physical construct to simulate elbow motion which used a fixed flexion axis and assumed that the ulna was fixed throughout forearm rotation. Neither bony articulation nor elbow capsuloligamentous constraints were considered, though muscles were simulated as springs [10]. Early computational models did not include 3D model creation, but instead focused on mathematical techniques to create a rigid body simulation for joint motion. Reich et al. considered the motion of individual voxels, based on MRI scans, to predict the motion of the radius as it rotated about the ulna in forearm rotation. A number of errors were cited to cause the inconsistencies in the results of the study, including deformation of the arm in MRI scans, inhomogeneities in the magnetic field during scanning, and the assumption of a fixed axis of rotation about the ulna [11]. Fisk and Wayne created a unique rigid body model that incorporated the effects of 3D bony anatomy, muscle forces, and ligamentous constraints to dictate motion of the elbow [15], moving past previous models with idealized joint motions, and studied the osteoarticular contributions to varus joint stability. Expanding upon this, Spratley and Wayne utilized more sophisticated modeling techniques to create a model with improved bony anatomy to study the effects of bony and soft tissue trauma on varus elbow stability [17].

1.3. Radial Head Injuries and Treatments

A brief review of elbow anatomy and motion is now provided for understanding of radial head injuries and subsequent treatments, as well as elbow joint modeling and the purpose of this work (Figure 1.3-1). Expanded upon in Chapter 2, the humerus articulates with the bones of the forearm, the ulna and radius, to cause elbow flexion, while the radius and ulna interact in forearm rotation [22]. The

distal humerus contains two primary articulating bony features. The pulley-shaped trochlea, located on the medial portion, articulates with the proximal ulna. The proximal ulna includes the anterior coronoid process and the posterior olecranon process, bony prominences which rotate about the trochlea. Lateral to the trochlea on the humerus is the capitellum, a round feature that articulates with the slightly concave proximal radius, called the radial head [9,23,24]. The elbow flexes about the humeroulnar articulation, causing the forearm to arc in the sagittal plane approximately 140° around this axis from full extension to full flexion [25]. The second major motion of the elbow is forearm rotation, which involves the distal radius rotating around the ulna about a pivot point in the proximal radioulnar articulation [22]. This results in the palm facing downward (pronation) or upward (supination) and a total range of motion of approximately 180° [25].

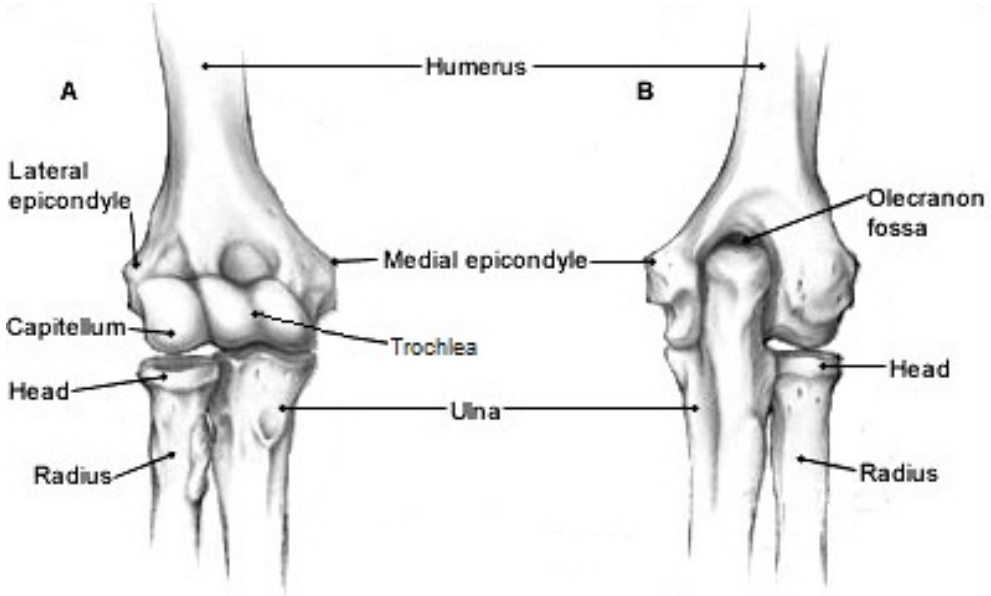

Figure 1.3-1: Anterior (A) and posterior (B) views of elbow bony articulation [22]

Research on the quantitative effects of radial head excision and/or replacement has generally been overlooked in experimental studies in favor of emphasizing the medial collateral ligament (MCL) and ulna, as the MCL is the primary stabilizer against valgus stresses while the ulna articulates with the humerus to provide bony stabilization of the joint. Contributions of the radial head (RH) to elbow

stability are well documented, however research regarding treatment of radial fractures is still rudimentary with widely differing opinions [9,26–29]. The radial head is considered the secondary resistance to valgus stresses in the elbow, providing up to 30% of valgus stabilization even in the presence of the MCL [9,25]. With a transected radial head and intact MCL, there is an average decrease in valgus stability of 25%. However, when the MCL is released, the elbow becomes 100% unstable without the radial head in valgus motion, indicating that injuries to the MCL leave the radial head as the primary stabilizer against valgus displacement. Regarding force distributions in the elbow, studies indicate that up to 90% of body weight can be transmitted across the radial head. This effect is exaggerated under forearm pronation because the axis of this rotation pivots about the ulna, causing proximal radial head migration and possible abutment against the capitellum of the humerus [9].

The prevalence of radial head fractures lends import to the research around radial head excision and prosthetic replacement. Breakages of this structure occur in almost 20% of all elbow trauma cases and in 33% of elbow fractures [9,30], making it one of the most common injuries to the elbow [31]. Between 1.7-5.4% of all fractures in the body are attributed to injuries of the radial head. These fractures are particularly seen in axial loading of the pronated forearm [9] and in the extended elbow [26], as the posterolateral margin of the RH abuts the capitellum and results in anterolateral fractures. Despite acknowledgement that an injury to the coronoid process of the ulna may lead to a gross lack of elbow stability, the arc of possible injury to this feature only includes the first 35° of flexion. In contrast, the radial head and neck have an arc of injury spanning from full extension to 80° of flexion, with the latter 45° of flexion selectively damaging the radial head. Thus, the opportunities for proximal radial fracture are vastly greater than those for the proximal ulna [9].

The Mason classification of RH fractures, considered the standard for labeling injuries to this structure, distinguishes four main types of breakage [9,32,33] (Figure 1.3-2). Type I injuries consist of

non-displaced fractures while Type II features a displaced fracture, often a single fragment less than 30% of the head. A non-complex, comminuted fracture constitutes Type III. Type IV injuries involve complex comminuted fractures, indicating damage to other associated structures in the elbow and/or displacement. One in three RH fractures is associated with other injuries, including fractures of nearby bony features, soft tissue damage, or both. Ligament attenuation or rupture has been noted to occur in all levels of radial head injury, but in up to 85% of Type III fractures and almost always in Type IV [9,33]. One such Type IV injury is the terrible triad, a debilitating injury with a high rate of complications which encompasses damage to the lateral ulnar collateral ligament, radial head, and coronoid process alongside elbow dislocation [9].

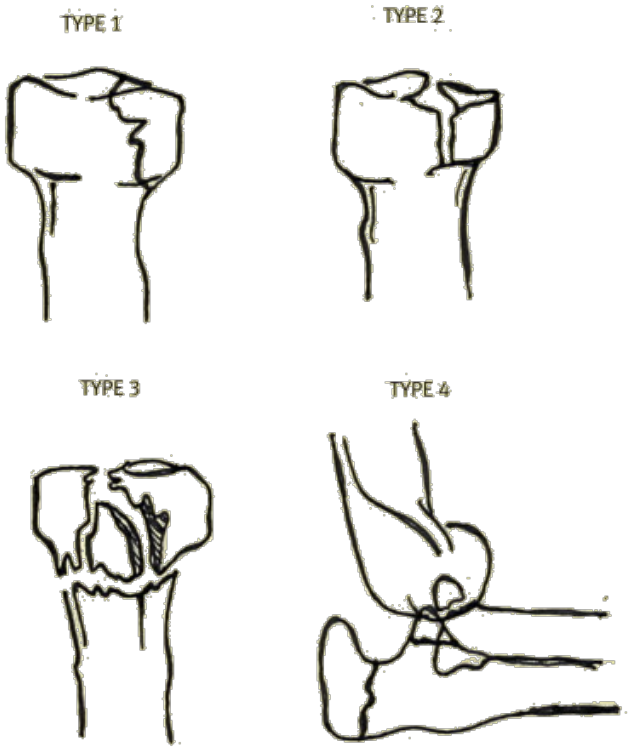

Figure 1.3-2: Mason classification of radial head fractures [33]

Type I radial head fractures are considered the most easily treatable as they rarely constitute invasive operative methods [9]. Conservative methods of brief immobilization followed by early motion are considered to produce excellent results, though in a small percentage this technique can result in

displacement or nonunion [26]. This is of particular note for injuries that include damage to the radial neck, as blood supply to the radial head runs within the intramedullary canal of the neck. Disruption of this supply can lead to tenuous results regarding bone union [33]. Depending on the presence of ligamentous injury, these complications may require subsequent radial head excision [9].

Type II fractures are considered the most controversial with regards to treatment, with both nonoperative and operative methods. Sometimes, nonoperative treatment similar to that in Type I fracture is recommended for Type II injuries, though if further displacement is imminent then several weeks of immobilization may be necessary. However, this particular method of treatment is performed under the assumption that delayed radial head excision is an option upon such complications as motion loss, significant pain, and RH deformation [9]. Three types of operative treatment are also suggested for those with Type II fractures: open reduction with internal or external fixation, radial head excision, and prosthetic radial head replacement. Open reduction and fixation is best utilized in cases of a large single fragment of the anterolateral margin, consisting of at least 30% of the radial head [9,34]. This lends ease to fixation techniques as well as prevention of impingement between implanted hardware and the ulna [9,33]. For radial head excision, early action within the first 24 hours is preferable, but remains a possibility for up to ten days [9]. Radial head replacement is rare for Type II injuries [34].

Determining the correct form of treatment is critical for Type III and IV fractures because of the loss of stability inherent in these injuries. Though radial head excision has been shown clinically to have satisfactory results [9], recent research has emphasized preservation of the innate kinematics of the joint and has thus suggested open reduction with internal fixation or arthroplasty [27,31,34]. Because of the breadth of injuries and potential comminution of the radial head in Mason III and IV fractures, reduction and fixation is not always possible [34]. Resection is suggested in cases of multiple radial head fragments, in gross, multi-millimeter displacements, or in examples of a large decrease in the arc of

flexion or rotation. Preferred protocol for excision of the radial head involves cutting at the level of the annular ligament, and within 24 hours of the initial injury for optimal healing [9].

Though a dichotomy of opinions exists in the literature regarding efficacy of removing the RH [35], several complications occur with treatment by radial head excision. Valgus forearm angulation can expand between 5 to 20 degrees post-surgery [9,27]. Some individuals experience a loss of strength in pronation or supination, and/or loss of motion [27]. Other complications include early degenerative arthritis of the ulnohumeral joint, calcification around the osteotomy site, and myositis ossificans. Carpal tunnel syndrome is sometimes reported [9]. In cases where the ligaments of the wrist are compromised, the radial stump can migrate toward the capitellum and destabilize the elbow [9,31]. A review of patients after RH excision also indicated that the radial stump tends to misalign medial and posterior, possibly leading toward radioulnar impingement and complications for future reconstructive treatments [31] as well as distal radioulnar joint subluxation [27]. In one clinical study, radiographic evidence of arthrosis was discovered in 14 out of 16 patients within twenty years after an excised radial head [27]. It is noted that less satisfactory results are seen in Type III fractures by this treatment than in Type II, because of the greater amount of comminution [9].

When a fracture of the radial head results in elbow dislocation, this is considered a complicated fracture, leading to complex instabilities. The radial head component of these complicated fractures is often treated with radial head excision or arthroplasty. Immediate excision of the radial head is standard, and implantation of a prosthetic is normally predicated on the condition that along with the radial head fracture, one of the following conditions is present: elbow joint dislocation, medial collateral ligament or lateral ulnar collateral ligament injury, olecranon or coronoid fracture, or distal radioulnar joint disruption. Radial head arthroplasty prevents gross valgus tilt, stabilizes the radius from proximal migration, and provides stability to the elbow in cases of collateral ligament rupture or ulnar fracture.

Composed of titanium, silicone, vitallium, or cobalt-chromium [32], these prosthetics provide resistance to axial loading and help to transfer loads to the ulna. More satisfactory results are seen in cases after implantation of current prosthetic hardware compared to leaving the radial head excised [9].

Literature also notes the necessity of removing the radial head prosthetic in the years following implantation due to a resulting significant loss of motion. In one study, destruction of capitellar cartilage, which covers the articulation between the humeral capitellum and the radial head, was noted in 2 of 5 individuals who required prosthesis removal [35]. This indicates issues regarding the methodology of radial head prosthetic implantation, including possible misalignment of the radial head or lengthening of the radial neck. Studies also comment on the mismatch of radial head and neck dimensions with those of prosthetics, and raise concerns about potential adverse results after implantation [30,36]. It is noted that prosthetic radial head designs should ideally have several size options, flexibility at the radiocapitellar articulation, and instrumentation to allow accurate and reproducible implantation of the device [9]. This brings attention to the fact that radial head replacement and the development of standardized protocols for implantation is under-researched.

Recent cadaveric research has begun to observe the effects of common treatments to the radial head after elbow injury on the overall kinematics of the elbow, though it is still a minor field in elbow orthopaedics. Two such papers observed the effects of the non-physiologic radial head prosthetic on the motion of the ulna as it moved in active flexion. Van Glabbeek et al. recognized the lack of a reliable method to replicate the length of the native radial neck during prosthetic replacement, and observed the effects of over- or under-stuffing the radiocapitellar joint [28]. By the creation of a telescoping radial head replacement, they lengthened and shortened the radial neck by 2.5mm and 5mm, and found that changing the length as little as 2.5mm affected ulnohumeral kinematics as well as radiocapitellar

joint forces. They postulated that the long term effects of such changes could lead to degenerative arthritis as well as other complications.

Another study performed by Van Riet et al. addressed the concern that the native radial head is ellipsoidal while radial head prosthetics are perfectly circular [29]. The effects of a change in the shape of the radial head were considered by the rotation of the native radial head 90° from its natural position, and the ulna was tracked in active flexion. Ulnar axial rotation was observed to be significantly affected by the change in shape, which could be detrimental to the long-term kinematics of the elbow. These studies provide insight into concerns that the oft overlooked radial head plays a significant role in elbow kinematics. Therefore, accuracy and reproducibility should be given equal consideration in prosthetic design and implantation protocol for the RH as given to other bony structures.

Two other cadaveric studies, the emphasis of this thesis, recently considered the effects of differing radial head prosthetic designs on elbow stability through the consideration of force redistribution in posterior subluxation of the forearm [37,38]. One such study considered the effects of mono- and bipolar radial head prosthetics, both accepted implantable designs, in stability of the elbow with a pronated forearm. Also examined in this study was the dependency of these two differing designs on lateral soft tissues [37]. The focus of the second study considered the biomechanical effects of various radial head prosthetic designs in an elbow afflicted with a terrible triad injury, including a monopolar, bipolar, and “anatomic” monopolar radial head system [38]. It was discovered through both studies that the most kinematically stable prosthetic was that designed to be more anatomically similar to the native radial head. The standard monopolar design decreased stability from the intact state, though the bipolar standard design significantly varied from intact and relied heavily on soft tissue constraints. These studies indicated that radial head replacement design is critical to the stability of the

elbow post-injury, and demonstrated that an emphasis on radial head research in compromised elbows could be a key factor in improving the functionality of the arm in a recovering patient.

1.4. Objectives

It is the objective of this thesis to expand upon previous rigid body models of the elbow [15,17] to explore the effects of different radial head prosthetic designs on elbow stability using cadaver research replication, as well as their dependence on soft tissue integrity, in the intact elbow and under the effects of the terrible triad injury [37,38]. J.P. Fisk and E.M. Spratley both utilized cadaveric computed topography scans to develop accurate three-dimensional surface representations of the elbow, and explored the accuracy of the model via emphasis on the coronoid process and elbow trauma [15,17]. The rigid bodies of this model will be created using the commercially available CAD program SolidWorks while motion will be simulated and analyzed through the COSMOSMotion add-in, equipped with an MSC ADAMS solver. Biomechanical function in the model will be dictated by physiologically represented structures employing accurate 3D articular anatomy, ligamentous constraints, muscle forces, and external perturbation.

2. ELBOW ANATOMY AND PHYSIOLOGY

2.1. Bony Anatomy

The elbow is a joint located approximately at the midpoint of the arm, and consists of three long bones: the humerus, ulna, and radius. The bones of the joint are oriented such that the humerus is located proximally to the ulna and radius, which are aligned nearly parallel to one another with the ulna positioned medially to the radius. Due to a tight fit between the protuberances and concavities of bony features, the elbow has a level of inherent stability, and thus it is commonly described as one of the most congruous joints in the body [9]. For this reason, complete understanding of the osteology of the elbow is critical for a thorough description of the elbow joint complex (EJC).

The humerus comprises the proximal half of the length of the arm, and the humeral head articulates with the thorax through the glenohumeral joint in the elbow. The surgical neck is positioned caudal and slightly lateral to the hemispherical humeral head, which transitions the bony geometry of the humerus into the cylindrical diaphysis of the long bone. Most of the musculature of the arm attaches to this feature, which is characterized by a thick ring of cortical bone surrounding a central shaft called the intramedullary canal. Along the lateral border of the humerus runs a shallow depression that runs obliquely across the surface of the diaphysis, called the spiral groove [24]. Observing a cross-

sectional view of the humeral diaphysis, tracking toward the distal regions of the bone on a computed topography (CT) scan, the intramedullary canal fills with trabecular bone and the cortical bone thins as the overall mass of the bone widens and shifts toward a triangular silhouette in the elbow. The posterior edge of the humerus flattens while the medial and lateral edges shift apart, creating the supracondylar ridges and terminating in the medial (EM) and lateral (EL) epicondyles. The space created in the posterior region of the humerus forms a hollow area referred to as the olecranon fossa. The lateral epicondyle is a small body feature which curves slightly anterior, while the medial epicondyle is a larger, more defined protuberance which is angled dorsal [23].

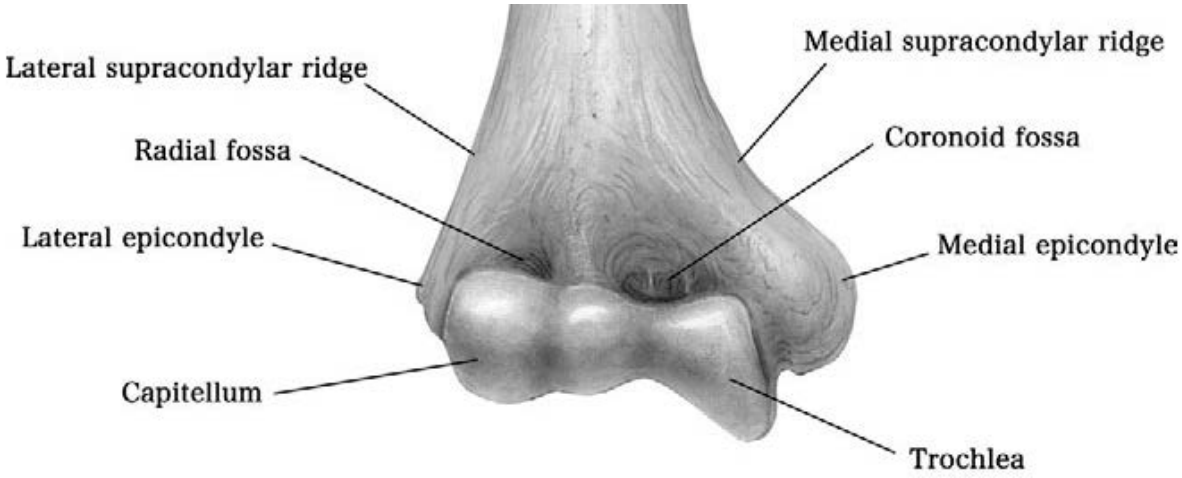

Figure 2.1-1: Anatomy of the distal humerus, anterior view [39]

The distal portion of the humerus is tilted anterior approximately 30° from the axis of the diaphysis and terminates in anatomy critical to the bony congruency of the elbow joint [9]. Slightly distal of the medial and lateral epicondyles are the primary articular surfaces of the humerus visualized in Figure 2.1-1, the trochlea and capitellum. Medial-most is the trochlea, a cylindrical eminence featuring a sulcus along its middle region, aligned such that the long axis of the trochlea is approximately in line with the mediolateral plane. It extends from the anterior to the posterior sides of the distal humerus, starting in the anterior coronoid fossa and terminating in the olecranon fossa posterior. The medial edge of the trochlea is larger and more pronounced than its lateral border, and the posterior

portion of the trochlea has a deeper concavity and wider edges that that at the front of the extremity. Covering an arc of 300°, the trochlea is coated with a layer of hyaline cartilage [40]. Along the central groove of the trochlea, the semilunar notch of the ulna articulates to permit flexion and extension.

Positioned lateral to the trochlea is a spherical feature called the capitellum. Its rounded surface, covered with hyaline cartilage, articulates with the slightly concave proximal surface of the radius during elbow flexion and forearm rotation. The capitellum is positioned on the inferior, lateral region of the end of the humerus, but unlike the trochlea does not extend to the posterior side. Above the capitellum is a small depression called the radial fossa, designed to accommodate the radial head in high degrees of elbow flexion [23]. The trochlear-capitellar articular axis is rotated internally approximately 5°-7° with respect to the humeral epicondyles and tilted valgus approximately 6°-8° from the humeral long axis [40].

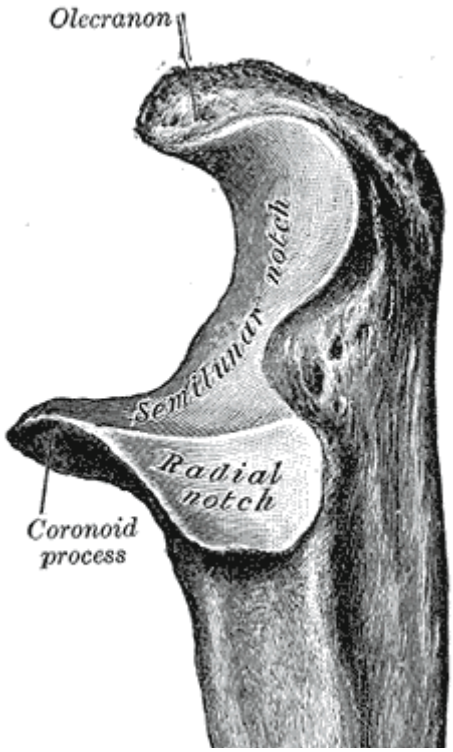

Figure 2.1-2: Anatomy of the proximal ulna, lateral view [24]

Located distal to the humerus and medial in the forearm is the ulna. It is a long bone that is the primary osseous contributor to elbow flexion; accordingly, most of its mass is located in the proximal end of the bone. Its upper extremity is wide and large compared to the rest of the ulna, and contains features that articulate with the humerus closely while also containing most of its muscle attachments. There are two large bony features in this region of the ulna, the olecranon and the coronoid process, demonstrated in Figure 2.1-2. Extending from the posterior half of the proximal portion of the ulna is the olecranon, a large hook-like structure which articulates with the olecranon fossa of the humerus. It has a prominent pointed tip which inserts into the triangular concavity of the olecranon fossa when the elbow is in extension [23]. Designed to withstand high physical forces, this thick bony structure protrudes from the back of the elbow and can be palpated easily. Lying along the most posterior surface of the olecranon where the triceps attach to the ulna, is a bursa which allows the bone to glide and flex smoothly under the skin [9]. The proximal-most surface of the olecranon is triangular in shape when observing from the transverse plane and the dorsal ridge of this triangle is where the triceps connect to the forearm. At the anterior side of the ulna is a triangular feature, the coronoid process, which articulates with the coronoid fossa of the humerus in flexion [23].

Between these two prominences lies a concavity with 190° of articular surface called the semilunar or greater sigmoid notch [40], defined by two deep concave grooves which run medial and lateral from the olecranon to the tip of the coronoid process. At the center of this structure, between these grooves is a thin border referred to as the semilunar ridge. This construct articulates closely with the sulcus of the trochlea in the humerus to stabilize flexion [9]. It opens 30° posterior from the long axis of the ulna, which corresponds to the 30° anterior angulation of the distal humerus to allow improved elbow extension [40]. A small deposit of fatty tissue lies transverse to the grooves of the greater sigmoid notch and divides the structure's olecranon and coronoid process [9]. These features

interplay with the humerus to cause the close bony articulation that identifies the elbow as highly congruous.

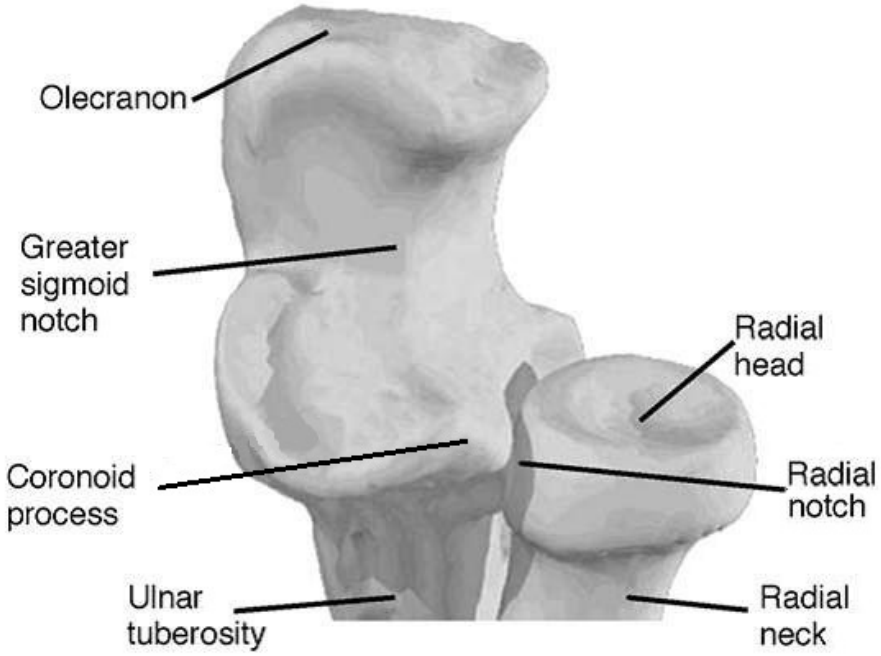

Figure 2.1-3: Proximal radioulnar joint and anatomy [40]

The medial groove is deeper than its lateral counterpart, and the lateral groove blends with a depression along the lateral-most border of the proximal ulna with highly defined anteroposterior ridges called the radial or lesser sigmoid notch (Figure 2.1-3). This feature is the location where the radial head and annular ligament interact with the ulna proximally and laterally. From the coronoid process, just beneath its slightly convex shape lays the ulnar tuberosity, which serves as a connection for the brachialis muscle. The diaphysis extends distal from the tuberosity, and has a triangular cross section, of which the lateral border is referred to as the interosseous crest. This surface provides attachment sites for the interosseous membrane. The shaft of the ulna tapers off toward the distal end [23].

In contrast to the upper portion of the bone, the lower extremity of the ulna is small and minimally involved in motion. On the lateral edge of the ulna is a rounded eminence, the head, which

articulates with the radius at the distal radioulnar joint. A narrow, pointed bony prominence referred to as the styloid process lies medial and slightly posterior on the bone. This feature extends further than the head of the ulna and is non-articular. Physical articulation with the wrist is prohibited by the presence of a triangular articular disk that extends from the distal border of the radius and connects to the ulnar styloid, but there is some soft tissue constraint between the two entities [23].

The third bone involved in the elbow joint is the radius (Figure 2.1-3). Located lateral and somewhat parallel to the ulna, the radius has several key features. The most proximal end, called the radial head (RH) is an ellipsoidal cylinder with a slight concavity of the uppermost face which articulates with the smooth, rounded capitellum of the humerus. This cavity is referred to as the fovea, which averages a depth of 2.4mm [41]. Thick hyaline cartilage covers the surface of the radial head to assist in articulation with the humeral capitellum, as well as 240° of the posteromedial surface for radioulnar articulation [9]. In contrast, the non-articulating anterolateral surface of the head is covered with a thin, yellowish cartilage [42]. The medial border of the head, which is somewhat thicker than the lateral edge, interacts with the radial notch of the ulna (Figure 2.1-3), while the lateral side is encapsulated by the annular ligaments [23]. Supporting the head and attaching it to the diaphysis of the bone is the neck, a slender region with an average offset of 4.2mm from the articular surface of the radial head [41]. The radial head is positioned eccentric to the neck [9]. The central axis of the radial head and neck forms an angle between 12°-17° from that of the diaphysis. Additionally, in neutral forearm rotation the major axis of the RH is oriented posteromedially to anterodistally, resulting in the radial head being torqued around the radial neck approximately 55° with respect to the distal radius [43].

Distal to the radial neck is a bony prominence on the medial side of the radial shaft called the radial tuberosity. This construct provides an insertion for the biceps brachii muscle. Starting posterior to the tuberosity, the interosseous crest of the radius descends prominently along the medial edge of

the diaphysis and provides attachment for the interosseous membrane. The diaphysis of the radius, almost triangular in nature, widens distally and displays a small degree of lateral curvature [23].

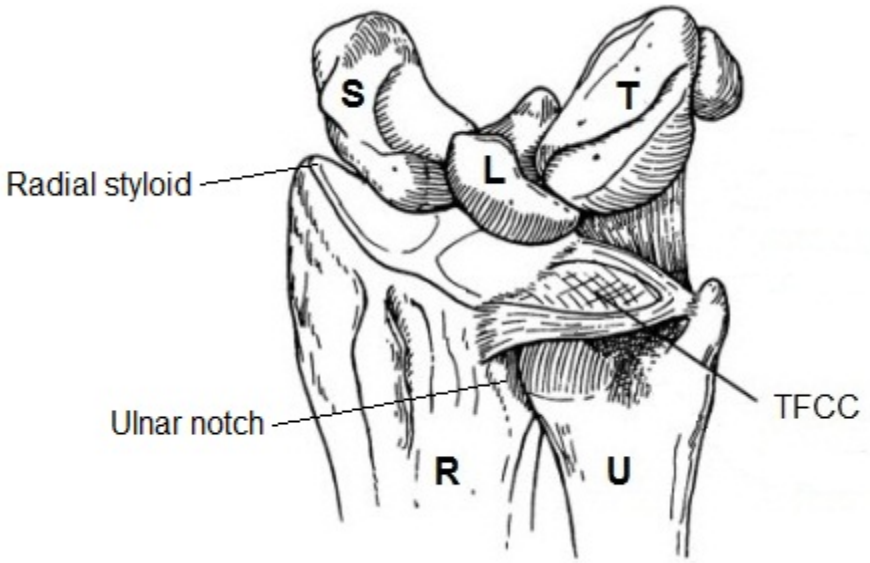

Figure 2.1-4: Distal radioulnar joint, dorsal view
(R- radius, U- ulna, S- scaphoid, L- lunate, T- triquetrum) [44]

The distal radius terminates in the widest surface of the bone with two main articular surfaces (Figure 2.1-4). On the medial edge is the ulnar notch, also referred to as the sigmoid cavity, a narrow area that accommodates the head of the ulna in the distal radioulnar joint (DRUJ). The bottommost surface of the radius interacts directly with the scaphoid and lunate bones of the wrist. Attached to a ridge along this bottom surface is the base of the triangular articular disk (TFCC), protecting the DRUJ from articulations of the wrist (Figure 2.1-4). Along the lateral edge of this region an eminence protrudes obliquely downward, creating the radial styloid [23].

2.2. Soft Tissue Anatomy

Despite the bony structures of the EJC being highly congruous, soft tissues greatly contribute to stability during the regular motions of the elbow. Three characterizations of soft tissues cooperate in

the elbow to support motion of the arm: active muscles, passive collateral ligaments of the EJC, and passive distal joint ligaments. Each plays a vital role in elbow joint stabilization.

2.2.1. Muscle Constraints

Four primary groups of muscles function to create elbow motion: the anterior bicep group, the posterior triceps group, the lateral extensor-supinator group of the anconeus and supinator, and the flexor-pronator group of the pronator teres and an assortment of smaller muscles [39]. Of these, cadaveric data by Morrey and associates indicate that the primary musculature contributing to elbow motion are the biceps, brachialis, and triceps [45]. These muscles can be characterized by two primary functions, elbow flexion and extension. These structures work antagonistically to control elbow motion and to maintain forearm location in space.

The flexors work in concert to cause flexion and to stabilize the elbow in extension (Figure 2.2-1). The brachialis is the primary flexor, which spans along the entire anterodistal surface of the humerus to insert through an aponeurosis onto the ulnar tuberosity and coronoid process. This insertion acts to restrain the elbow from posterior subluxation [39]. It has a larger cross-sectional area than the biceps brachii [23], but is disadvantaged mechanically because of its proximity to the axis of rotation for flexion [9,39]. The biceps brachii has two heads which both originate in the shoulder; the short head attaches to the coracoid process of the scapula, while the long head connects to the supraglenoid tubercle and follows the intertubercular groove of the humerus. These two distinct heads converge into a single muscle, and this biceps tendon inserts in the posterior margin of the radial tuberosity. The lateral edge of the tendon sweeps out into a thin sheet of fascia called the bicipital aponeurosis, and thus becomes a part of the deep fascia of the forearm. Via the aponeurosis, the biceps is provided an indirect connection to the ulna despite its discrete attachment to the radial tuberosity [39]. The biceps brachii is

a major flexor of the elbow despite its smaller cross-sectional area than the brachialis because of its insertion further from the joint center, giving it a greater moment arm. Its attachment to the radius also makes the biceps a strong supinator [9,39]. Because of this, when the forearm is in pronation, elbow flexion is achieved by action of the brachialis [39].

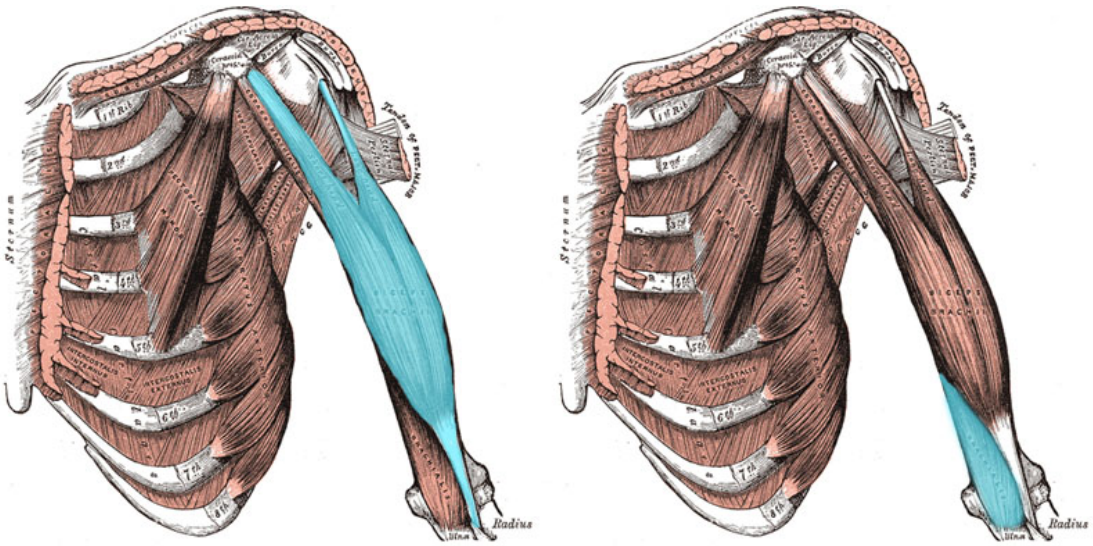

Figure 2.2-1: Highlighted biceps (left) and brachialis (right), anterior view [24]

The triceps is considered the major extensor in elbow motion, and comprises the entire posterior musculature of the arm (Figure 2.2-2). The term "triceps" refers to the muscle's three heads, two of which originate from the posterior surface of the humerus. The long head has a small, discrete connection to the infraglenoid tubercle of the scapula, while the lateral head arises from the proximal lateral border of the spiral groove. This origin spans a distance comprising of approximately one third of the length of humerus in a linear fashion. The medial head extends the entire posteromedial distal surface of the humerus from the medial margin of the spiral groove. It is the deepest of the three components, lying subordinate and distal to the long and lateral heads. These distinct portions blend together into a single triceps tendon, which inserts onto the entire proximal and posterior margin of the olecranon. A layer of fascia blends with the distal 40% of the triceps [9].

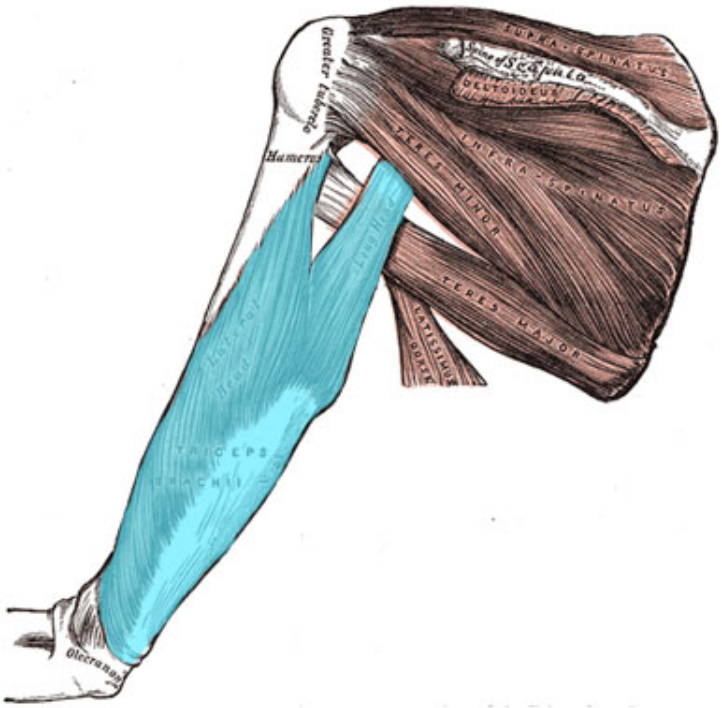

Figure 2.2-2: Highlighted triceps, posterior view [24]

2.2.2. Collateral Ligamentous Constraints

The collateral ligaments are specialized thickenings of the elbow joint capsule. This joint capsule, the primary contributor to soft tissue stabilization of the elbow, spans proximally from the coronoid and radial fossae of the humerus to attach to the distal coronoid process medially and lateral annular ligament. It wraps about the olecranon fossa on the posterior humerus and around the supracondylar ridges and connects anteriorly on the trochlea [23]. The posterior and transverse portions of the capsule are thick and involve a collection of ligaments critical to elbow motion. The anterior portion of the capsule is thin and mechanically weak, and contributes little to the stability of the elbow despite its tautness in extension [9].

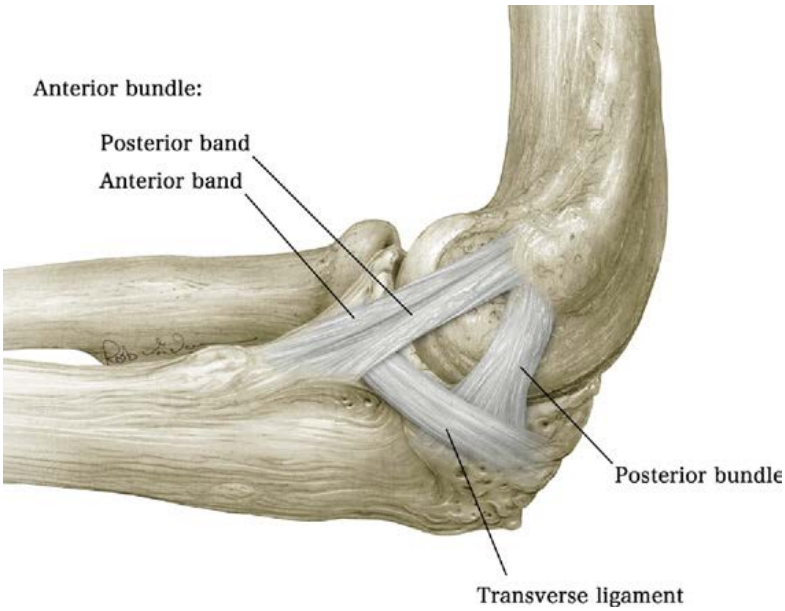

Figure 2.2-3: The medial collateral ligament complex, medial view [40]

The medial collateral ligament (MCL) consists of three separate bands: the anterior, posterior, and transverse. Located on the medial side of the elbow and extending from both the anterior and posterior sides of the medial epicondyle to diverse insertions on the ulna, it is the primary stabilizer against valgus motion (Figure 2.2-3). The transverse bundle, or ligament of Cooper, is poorly distinguishable [24] and has been shown by experimental evidence to contribute negligible support to elbow stability [45]. In contrast to the transverse band, the anterior bundle is the most physically discrete band of the MCL. Its origin spreads along the anteroinferior surface of the epicondyle, while it inserts on the ulna in a broad band on the medial margin of the coronoid process, creating two subsets to the anterior band: the anterior-most anterior band and a more posterior portion. Because of its size and position across the ulnohumeral joint, the anterior portion of the MCL has experimentally shown that it is the main valgus stabilizing factor out of the bands of the ligament [22,39]. There is indication that the MCL provides elbow stability in extension, supported by the observation that the MCL is taut when the elbow is in extension but becomes lax with increased flexion angle [39]. The collagen fibers of the anterior MCL have an additional layer which is confluent with the muscle fibers of the flexors [40].

The posterior component of the MCL is a wide series of fibers that are but a thickening of the posterior portion of the capsule surrounding the elbow joint, and is only distinguishable at 90° of flexion. It crosses from the posterior surface of the medial epicondyle and fans out across the medial margin of the semilunar notch. At its widest, the posterior bundle has a width of 8mm, and is active in higher flexion angles [40], acting as an antagonist to the anterior band regarding elbow flexion. However, these two bundles of fibers act in concert for valgus stability.

The lateral side of the elbow contains the lateral collateral ligament complex, comprised of several ligaments that contribute to stability though are less discrete than the medial collateral ligament. It contains three separate bundles: the radial collateral ligament, lateral ulnar collateral ligament, and annular ligament. The radial collateral ligament (RCL) originates from the lateral epicondyle and becomes indistinguishable from the annular ligament around the radial head at its insertion [23] (Figure 2.2-4). The structure fans out anterior, medial, and posterior across the radial head and generally remains taut throughout the flexion arc. Thus, it can be extrapolated that the origin of the RCL is located near the axis of flexion. The lateral ulnar collateral ligament (LUCL) originates blended with the radial collateral ligament on the lateral epicondyle and inserts discretely on the supinator tubercle of the ulna. Because of its contralateral placement to the medial collateral ligament, the LUCL is the primary lateral stabilizer of the ulnohumeral joint [9].

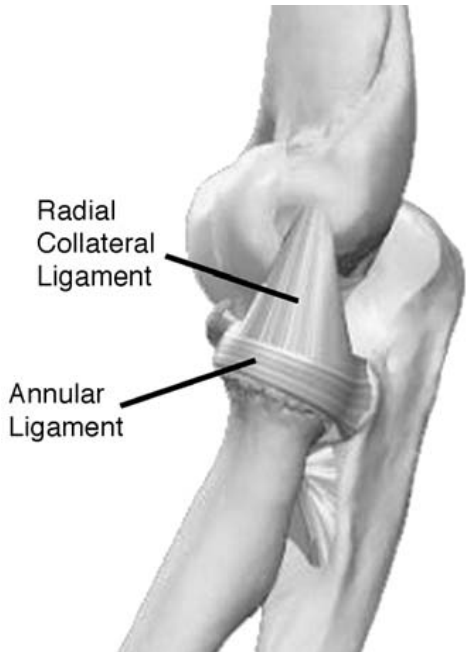

Figure 2.2-4: Radial collateral and annular ligament, lateral view [40]

The annular ligament, also part of the lateral ligament complex, is a thick circular band of tissue made of circumferential fibers, which wraps around the head of the radius and attaches to the anterior and posterior margins of the ulnar lesser sigmoid notch (Figure 2.2-5). Its function is to maintain the proximal radioulnar articulation, particularly in supination [22,40]. Because of its insertions on the ulna, it is responsible for approximately four-fifths of the fibro-osseous ring, while the lesser sigmoid notch contributing the remaining one-fifth of the structure. Because the radial head is not perfectly circular, the anterior aspect of the annular ligament becomes taut in supination, while the opposite holds true of the posterior portion. A small band of fibers which extends from the annular ligament to the ulnar tubercle is sometimes distinguished as the accessory lateral collateral ligament, but is often considered a portion of the annular ligament [9].

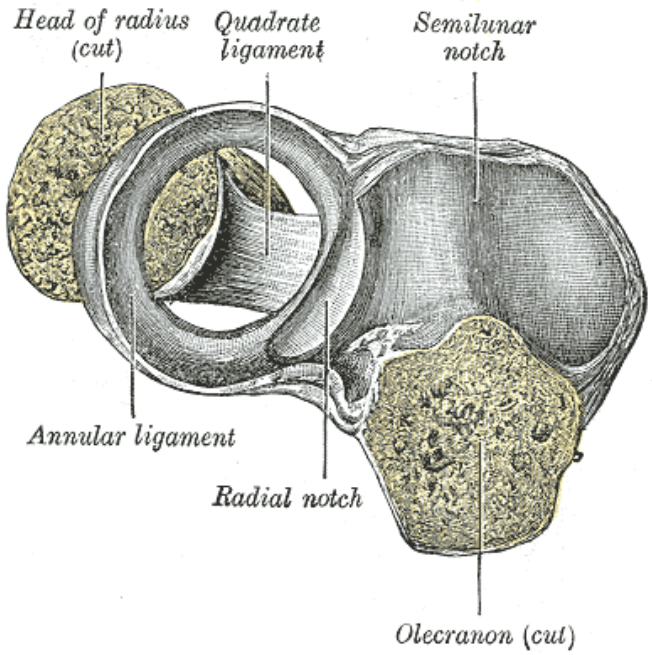

Figure 2.2-5: Transverse, superior view of the annular ligament [24]

2.2.3. Articular Joint Capsule

Surrounding the elbow joint and containing lubricating synovial fluid is the articular joint capsule. It is a thin fibrous sheet of tissue which attaches to the proximal and distal ends of the elbow, protecting and encapsulating the joint.

Anteriorly the capsule attaches on the humerus proximal to the ulnar and radial fossae, while its distal insertions expand the breadth of the joint, laterally blending with the annular ligament and medially inserting on the anterior margin of the coronoid. The posterior capsule expands distally from the mediolateral margin of the sigmoid notch of the ulna and again combining with the annular ligament. It originates on the humerus proximal from the olecranon fossa and extends along the supracondylar ridges both medially and laterally. Distal from the annular ligament, the capsule attaches to the radial neck to contain synovial pockets that lubricate the fibrous ring (Figure 2.2-6) [9,46].

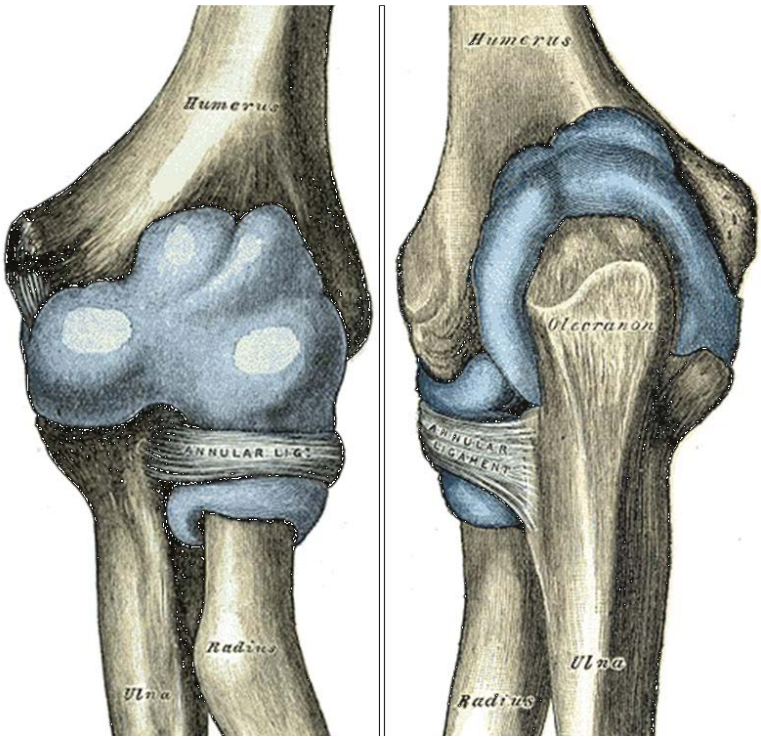

Figure 2.2-6: Anterior (L) and posterior (R) views of the elbow joint capsule (blue) [24]

Due to its thin structure and lack of distinct bands, the posterior capsule is ignored in kinematics studies, though the anterior capsule (AC) is noted in literature for its contribution to elbow stability. It is described as a thin, translucent structure which has defined thickenings, implying that it serves a resistive role in joint motion. Its thickness varies, though morphological studies have indicated the average thickness of the healthy AC as 0.6 ± 0.2mm [47]. Fibers of the capsule are oriented transverse and oblique, providing strength to the structure [9,46]. It is taut in full extension and becomes more lax throughout the flexion arc, reaching its greatest capacity for synovial fluid at approximately 80° of flexion [9].

While one study described distinct thickenings within the joint capsule, naming them and giving them explicit functions [46], most have described simply the overall cruciate pattern of the capsular fibers [9,47,48]. Despite the general lack of research regarding the capsule because of a greater

emphasis on ligamentous, muscular, and bony contributions to stability [46,49], Morrey and An demonstrated that in extension 85% of the soft tissue resistance to distraction occurs in the anterior joint capsule alone [48]. Valgus stability was divided equally between the AC, bony articulation, and the medial collateral ligament in full extension, with capsular resistance transferring to the MCL throughout the flexion arc. The AC also demonstrated 32% of the resistance to varus instability while in extension. At high flexion angles, the capsule contributed little or no stabilizing effects, less than 13% of overall stability, but the importance of the capsule for elbow joint stability is clear in lower flexion angles and in full extension [48].

2.2.4. Distal Ligamentous Constraints

Though not an immediate part of the elbow joint complex, several distal fibrous joints provide additional stability for the forearm, in turn influencing the kinematics of the elbow. Disruption of these ligamentous constraints can cause laxity at the proximal radioulnar joint, so the understanding of these structures is paramount to the study of elbow motion. The most proximal member of these stabilizers is the oblique band or cord, located just distal to the elbow joint capsule. It is a small and inconsistent ligament formed by the fascia, which connects the distolateral edge of the coronoid process, alongside the insertion of the brachialis, to the distomedial radial tubercle, near the biceps attachment [50]. Though it is shown to be taut in full supination, suggesting some radial stabilizing function, it shows significant morphological variability. Thereby, it is largely considered to be of little functional significance [9,50].

Distal to the oblique band, the interosseous membrane (IOM) is a thin fibrous membrane which extends obliquely between the interosseous crests of the radius and ulna. This structure provides a direct attachment for the entire breadth of the negative space between these two parallel bones. The

IOM contains three bands, or thickenings of the tissue, with fibers directed in opposing directions to provide enhanced stability throughout all forearm rotations [50–53] (Figure 2.2-7). Most proximal in the membrane is the central band (CB), located approximately mid-diaphysis of the two bones and oriented approximately 21°-28° from the ulnar diaphysis, angled toward the proximal radius [54,55]. The band and the long axis of the radius form an angle of approximately 20° [55]. Its average mid-substance depth is 1.1cm [51] and width is 9.7mm, making it the largest and thickest of the bands [50]. The size of the band indicates its importance for radioulnar stability, as studies indicate its restraint against radial proximal migration and importance for load distribution [52,53].

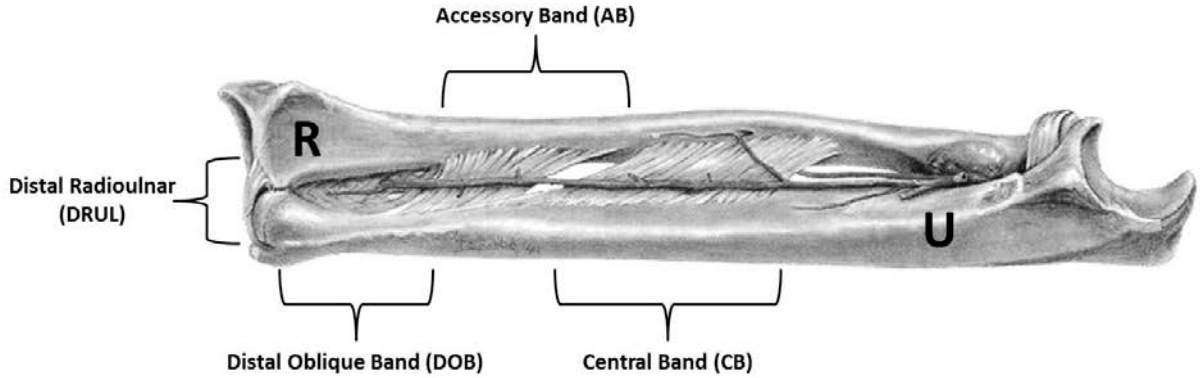

Figure 2.2-7: Sagittal view of the forearm under neutral rotation. U=ulna; R=radius [56]

Distal from the CB and oriented in a similar fashion is a fanned series of fibers called the accessory bands (AB). These are less substantial than the CB, almost continuous with the rest of the membrane, and their exact location and number of bands varies between specimens [50]. Functionally the AB is considered to provide support to the central band. The furthest portion of the IOM from the EJC is the distal oblique band (DOB), a relatively thick bundle whose orientation opposes that of the CB and AB. It blends with the distal radioulnar joint capsule. It originates in the distal one-sixth of the overall length of the ulna, and inserts into the inferior and medial rim of the radial sigmoid cavity. It has a similar thickness to the CB, but is less wide. This portion of the IOM is considered to provide secondary support at the DRUJ in distal and volar directions [50].

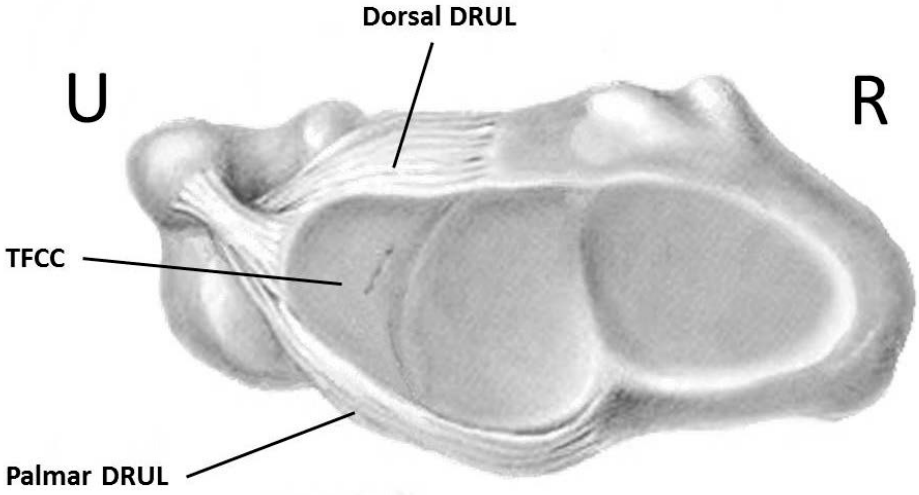

Figure 2.2-8: Distal radioulnar joint with key ligaments, inferior view (R- radius, U- ulna) [56]

Critical to forearm stability is a fan-shaped ligament with two distinct fiber bundles, the dorsal and palmar distal radioulnar ligaments (DRUL) [57]. These ligaments support a triangular fibrocartilage disc (TFCC) spanning the dorsal-most area between the ulna and radius (Figure 2.2-8). They originate in the ulnar fovea and extend to the dorsal and palmar margins of the sigmoid notch [53]. Cadaver studies suggest that the dorsal DRUL stabilizes the DRUJ in pronation and its palmer counterpart becomes the primary restraint under supinating loads [58].

2.3. Local Joint Characterization

Elbow and forearm positioning can be defined by specific articulations, which function collectively to cause two distinct types of motion. Structurally, the elbow is classified as a synovial joint due to the presence of a joint capsule, instead of cartilaginous tissue, connecting articular surfaces. Joint articulation is technically defined as trochoginglymus, describing the two primary motions of the elbow, flexion and forearm rotation [9]. The articulations of the humeroulnar and radiocapitellar joints within

the actual elbow joint share the same axis of rotation, and lead to elbow flexion and extension (F/E). The ulnohumeral joint, which dictates flexion and extension of the elbow, is pseudo-hinge, or a ginglymus joint. This type of motion is the primary movement of the elbow, and the ulnohumeral joint constitutes a majority of bony articulation within the arm. The radiocapitellar joint serves as a secondary stabilizer against valgus motion and provides a majority of the resistance against axial compression [9,40]. The other major rotation of the elbow, a pivoting motion called pronation and supination (P/S), is controlled by the proximal and distal radioulnar joints.

The flexion/extension arc begins in full, slight hyperextension such that the forearm is angled slightly posterior from the long axis of the humerus. The full flexion arc sweeps 150° [40] as the ulnar coronoid process rotates about the trochlea anteriorly [40], approximately in the sagittal plane. Soft tissues prevent abutment of the ulnar olecranon or coronoid against the corresponding fossae on the humerus [40]. Though initial observation would indicate that the ulnohumeral articulation is simply a hinge joint with the axis of rotation passing through the medial and lateral epicondyles [59], there is a greater range of motion for F/E.

Tracking the motion of the ulna shows that it tracks a helical path about the trochlea of the humerus, with the axis of rotation rotated internally 3°-8° from the plane of the epicondyles [9]. This is referred to as the screw displacement axis (SDA) [59,60]. The locus of rotation is located in a several millimeter range at the center of the trochlea [9]. Early electromagnetic tracking research indicated that the SDA translates and pivots as the forearm travels through the flexion arc [61]. Bottlang et al. calculated the SDA by utilizing algorithms described by Beggs in 1983, which predicted the motion of a body as it simultaneously rotated and translated about an axis [59,62]. Ulnar anteroposterior and mediolateral translations were also noted during Bottlang's study (Figure 2.3-1) [59].

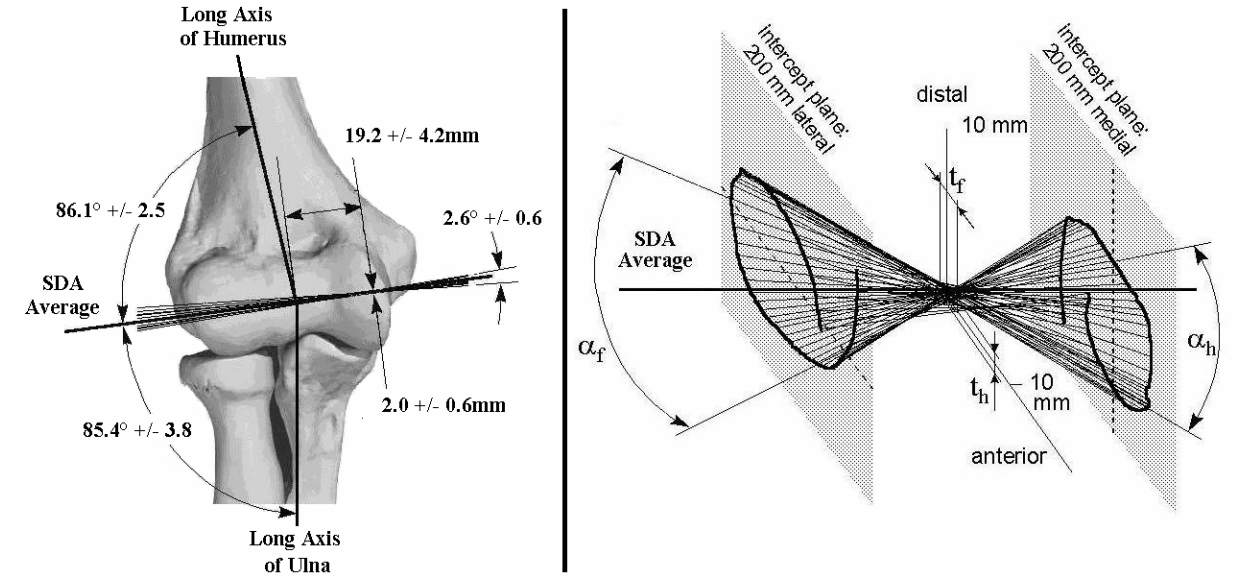

Figure 2.3-1: Visualization of SDA translation and rotation overlaid onto the elbow joint, anterior view (left) and the pathway of the SDA with respect to the humerus during flexion [63]

Forearm rotation is the second motion of the arm, positioning the forearm and hand in space relative to the elbow flexion angle. Supination refers to the anterior turning of the hand such that the palm faces upward when the elbow is flexed at 90°, while pronation turns the palm downward. The radiocapitellar and the radioulnar joints allow 85° of supination and 75° of pronation [40]. Tissue impingement restrains pronation while supination is limited by bony articulations of the ulna [9]. Full supination places the long axes of the ulna and radius nearly parallel to one another. Pronation, conversely, causes the distal radius to rotate about the distal ulna while the proximal migrates proximally against the capitellum, forcing their projected long axes to intersect. There is very little rotation or translation of the ulna [64]. The S/P axis of rotation extends from the geometric center of the radial head to the fovea on the distal ulna [40,64]. Thus, forearm rotation is oblique to the long axes of the radius and ulna and separate from the motion of elbow flexion. Neutral forearm rotation is defined as when the radial and ulnar styloids are aligned parallel to the long axis of the humeral diaphysis [65].

3. THREE-DIMENSIONAL BODY ACQUISITION AND SIMULATIONS

3.1. Overview

In order to create an elbow computational model which utilizes both accurate bony articulations and soft tissue constraints, proper recreation of these features is critical for accurate joint kinematics. Regarding bony anatomy, acquisition of 3D geometry was obtained through computed topography (CT) scans of a cadaveric specimen, thus transcribing the bony features into representative two-dimensional images. These slice images could then be processed using meshing and triangulation techniques in the commercially available medical imaging program MIMICS (Materialise's Interactive Medical Imaging Control System, Materialise, Ann Arbor MI), which extrapolates 2D data into the third dimension and renders it into voxelated solid bodes.

Three-dimensional representations of the humerus, radius, and ulna were then exported into the computer-aided design software SolidWorks (SolidWorks Corp., Concord, MA) for relative positioning in space, maintaining the precise placement of the original specimen. SolidWorks functions were used to identify and label prominent anatomical features, while the program add-in COSMOSMotion was utilized to model solid body conditions such as penetration and body restoration, as well as soft tissue constraints, including constant muscle force vectors and tension-only ligament elements. It also served

to apply perturbations and physical constraints to the model. Iterative analysis of the model was performed by the ADAMS solver inherent to COSMOSMotion, a robust multibody dynamics and motion analysis software. Thus, biomechanical function in this rigid body model of the elbow was controlled solely by accurate bony articulation, ligamentous and muscular soft tissue constraints, and external loading.

3.2. Acquisition of 3D Bodies

Computer topography scans were used from a previously described 91-year-old female cadaver upper extremity [17,66]. Three separate scans were performed on the specimen. A scan with 2mm slice thickness was made of the entire extremity when flexed approximately 30°, captured in 348 slices, as well as two higher-resolution scans of 0.4mm slice thickness of the immediate elbow joint. These two 0.4mm scans, each with 390 slices covered an area approximately 10cm proximal and distal from the joint with the arm, and captured the joint in approximately 30° as well as 90° of flexion.

3.2.1. Masking and Preprocessing

Scans obtained from the cadaver specimen were saved as 2D DICOM (Digital Imaging and Communications in Medicine) images and uploaded into MIMICS, which was used to process these stacked files into three dimensional surface bodies. The DICOM images were stacked according to the order of image capture with respect to scanner orientation. Using algorithms that consider effects of partial volumes created between slice thickness, the program detects pixels located identically between slices and extrapolates edges between them, thus creating voxels from planar data. The region of

interest (ROI) is determined by the designation of a common threshold value and creates sets of images called masks. These masks can be edited individually to create separate solid bodies.

The threshold chosen for mask designation to isolate the bones of the scans was measured in Hounsfield units (HU), based upon the Hounsfield scale which quantitatively describes radiodensity in radiographic images [67]. This scale normalizes the linear attenuation coefficient of scanned bodies relative to distilled water, and indicates the HU of bone to range from +400 to +1000. However, the low density of trabecular bone found in the epiphyses caused the necessary Hounsfield unit to shift down to +225 for inclusion of all bony features of the elbow radiographic images. A threshold of +225 HU is generally higher than that of soft tissues, and thus these features were excluded from the masks. This allowed masking of all desired bony regions of interest, though masks also included some pixels extraneous to osseous tissue. This excess data was filtered from the mask using preprocessing techniques.

The MIMICS software features several functions which allow manual modification of the calculated mask to exclude unwanted information. Multiple slice cropping is the most crude of these features, but allows rapid exclusion and inclusion of information from DICOM image slices not selected by the chosen Hounsfield threshold. This employed a single-slice cropping tool combined with a multiple-slice edit tool, and was useful for two particular actions with creation of the elbow model. First, the humerus, radius, and ulna could each be separated from one another by mass removal of the information regarding the other two bones. The multiple-slice cropping also allowed for rough removal of any extraneous material, including skin and the armature used to support the cadaver arm in the scanner. As such, a solid body could be created for each individual bone, though this approach was too rough of an approximation to perform at the close-fit articular surfaces. At these junctures the single-slice cropping tool was utilized to more specifically exclude, slice by slice, noise discontinuous from bony

tissue, as well as to individualize each bone at the tight articular surfaces. These features allowed for a single bone to be actively selected for processing into a three-dimensional body.

The creation of polylines established a set of contours on each slice, creating closed loops of active selected material in the mask and serving as the framework upon which the three-dimensional body was created. Polylines, however, excluded the negative space of the intramedullary canal and trabecular bone in its closed loop. These gaps were filled utilizing the 'fill polylines' function, encircling the cortical shell of the bone and selecting all material within. This feature provided an avenue to quickly confirm the creation of continuous, non-pitted surfaces. Any discontinuities in the cortical shell of the bone could then be selected slice-by-slice, as these slices would not complete the 'fill polylines' function and thus were easy to identify, and the aforementioned cropping tool could be used to select pertinent information and re-establish the polylines.

In the epiphysis of each bone, porosity and density disparities between cortical and trabecular bone caused pitting in the calculated borders of the masks, though the original outline of the bone could be seen in each slice. It was necessary to rectify these discontinuities for accurate 3D representation, and several functions inherent to MIMICS enabled this action. Two functions, 'dilate' and 'close', projected active pixels onto surrounding inactive space based on user specifications. Dilation of the mask, a coarse method, extended an active pixel onto those surrounding both in 2D and 3D, coarsely filling out holes in articular surfaces. However, the crudeness of this feature and its inclusion of extraneous information caused this to be used sparsely. A more refined method to the same end was the 'close' function, which only dilated areas with apparent discontinuities. Thus, areas with good capture of the bony surface, such as the diaphysis of each bone, were not affected by this action while porous articular surfaces benefited greatly in defining the thin cortical shell.

With the completion of a single continuous mask for each bone and the establishment of polylines, shell reduction was performed, which limited the creation of polylines to the largest user-defined volumetric body, thus removing any final noise remnants from the feature. Having completed this, hundreds of DICOM images were preprocessed to define each individual bone and allow for creation of three-dimensional bodies for the humerus, radius, and ulna.

3.2.2. Characterization of Bony Structures

Modeling of bony surfaces was but one facet of the characterization of these structures. Definitions of joint coordinate systems as well as motion necessitated a quantitative identification of bony geometry. The commercially available MedCad module inherent to MIMICS allowed the application of line-, plane-, sphere-, and cylinder-fits of the bones of the elbow in a reproducible fashion. A fit was generated by isolating the anatomical feature of interest using the aforementioned cropping functions. Isolations of the diaphyses of the three long bones, cropped to emphasize the region of the bones where the silhouette was roughly circular, were utilized to create a best fit line for the long axis of the humerus, radius and ulna. Another of the radial neck and proximal ulna, taken above their respective tuberosities, were used to determine the central axis of both of these structures. A sphere fit of both the humeral head and radial head was created to find their geometric centers, isolating the portions of the CT scans that captured the breadth of these two features; the application of a cylinder fit of the trochlea of the ulna was performed in a similar manner. An example of the radial sphere and radial neck long axis fits overlaid on the proximal radius is shown in Figure 3.2-1.

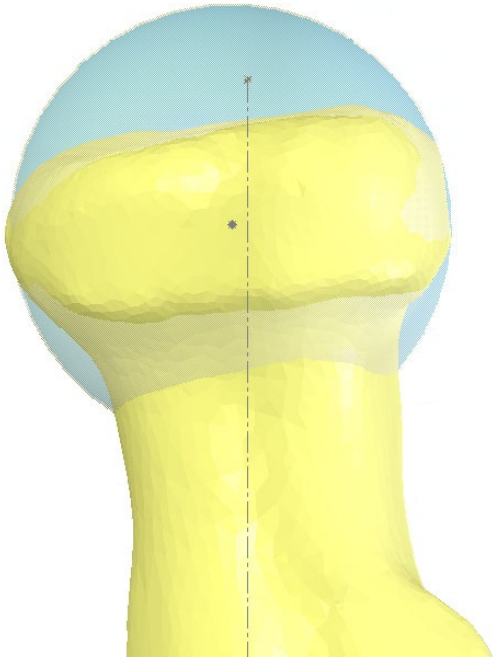

Figure 3.2-1: Radial head with overlaid sphere fit, center of radial head and radial central axis

Each of these fits was reported as a text file from MIMICS listing the fit lines as two Cartesian coordinates with a directional vector. The spheres were described as the coordinates of a central point alongside those of a point on the outside edge of the sphere, such that the distance between the two points was equal to the radius length. The module reported the cylinder fit as the Cartesian coordinates of the two ends of the central axis of the shape, as well as the radius length and the height of the cylinder. The midpoint of this central axis was gleaned as located one-half the distance between the two ends of this axis.

3.2.3. Stereolithography (STL) Files and Their Processing

Solid bodies created in MIMICS were output as a file type known as stereolithography (STL), a file that can be read in both binary or ASCII. This feature enabled the file size to be very compact while

being almost universally accepted by different 3D modeling software packages. STL files describe surfaces via triangulation. Each individual triangle is described by twelve Cartesian coordinates; nine of these coordinates locate the position of the three vertices of each triangle, while three direct the unit normal to the surface pointing out from the body.

When the 3D body is first processed and triangulated after masking of the DICOM images, the created body has tens of thousands of triangular facets that represent the surface. While this rendering is the most accurate representation of the scanned cadaver specimen based on the voxelated surfaces, the quantity of data is prohibitive in creating rigid body models in 3D modeling software. It can lead to dramatic computational time and limitations in importing the file into a specific CAD program. Fortunately these highly detailed surfaces are often unnecessary for RBM, so it is appropriate to simplify the created surfaces without losing critical information. A remeshing feature integrated into MIMICS allowed for selective refinement of the triangulated surfaces while maintaining an accurate representation of the original body, thus decreasing the amount of data associated with the file. This action resulted in a 3D rendering of the bones of the elbow with a functional number of triangles that was reasonably smoothed and free from non-physiologic structures.

Two methods of remeshing were used to simplify the contours of the bones. The first, called smoothing, removes discontinuous cavities and features created due to density fluctuations and porosity in the cadaver specimen. Smoothing is an iterative process which considers each vertex using the weighted contributions of neighboring triangles. Calculations for the translation of a vertex are based on the user-defined Smoothing Factor ratio, which indicates an increased amount of smoothing as it approaches a value of 1.

Triangle reduction is the other primary remeshing tool, and serves to shrink the thousands of triangles representing the body to a number usable to CAD programs while maintaining surface

contours. While each body could have upwards of 100,000 triangles after creation, trial and error indicated the optimal triangle number for export into SolidWorks was twenty thousand, making triangle reduction critical. To achieve this drastic triangle difference while preserving bony features, the first step was definition of a shape-quality threshold, which develops a more uniform mesh by removing highly acute triangles. Though this would not significantly change the number, having uniform triangles would greatly increase the quality of the mesh. The threshold for these models was defined as between 0.15 and 0.30.

The second step to triangle reduction considered the angle of two triangulated surfaces sharing a single edge. A minimum angle, which would warrant preservation of two individual contours, was user defined. Any two triangles meeting at an angle less than this were considered a single facet, and a geometrical error tolerance was applied to this which defined the total translation allowed between the original facets and new surface. The default level of 0.05 defined in MIMICS was considered appropriate to maintain the quality of the contour and the volume of the body.

To create the most accurate models within the triangle limitation, both the low resolution and high resolution CT scans of the cadaver specimen were utilized separately to create the 3D bodies for RBM. The low resolution (2mm) scans created the diaphysis and ends of the bones distal to the elbow joint complex, as emphasis was on the elbow joint. Thus, the less important features could be smoothed and reduced without losing the quality of the articular surfaces. In contrast, the 0.4mm thickness high resolution scans created the articular surfaces and were cropped just beyond the elbow joint, such that a maximum number of triangles could be devoted to each surface. The humerus was cropped just proximal to the supracondylar ridges, while the ulna and radius were cropped just distal to their respective tuberosities. Thus, the articular surfaces could have the largest number of triangles possible

without sacrificing the quality of any other feature, as these surfaces would dictate motion in rigid body modeling.

MIMICS assigned a local coordinate system to each bone relative to one another with respect to the scanning orientation, which enabled accurate rebuilding of the model after export to a CAD program. As mentioned in Section 3.2, two flexion angles were captured using the high resolution scans, approximately 30° and 90°. Processing techniques were performed on both of these separate files and they were registered to each other within the same coordinate system. This was performed so that flexion could be tracked and thus defined quantitatively in a CAD program for accurate representation of motion.

3.3. Model Simulation

Once created in the MIMICS imaging software, it was necessary to import the three-dimensional bodies into a CAD program to build a functional, manipulate-able model. SolidWorks was used to assemble and constrain the separate long bones of the elbow in 3D space, faithfully restoring the scan orientation of flexion, forearm rotation and joint articular space (Figure 3.3-1). The fits of the various bony features were imported into the program and important bony prominences were marked on the bodies. Implementation of the SolidWorks add-in COSMOSMotion enabled the definition of ligamentous constraints and application of muscle forces, as well as boundary conditions for bony contact. Ligaments were modeled as tension-only spring elements with applied pre-tensioning. Muscles were force vectors of constant magnitude. The boundary conditions were defined using stiffness and involved setting parameters to govern contact between bones. Calculations within COSMOSMotion were performed iteratively using the ADAMS solver, utilizing constitutive equations to solve resultant forces and body displacements. The end result was a rigid body elbow model whose

motion was constrained only by bony contact, muscle forces, and ligamentous constraints to accurately replicate cadaver research.

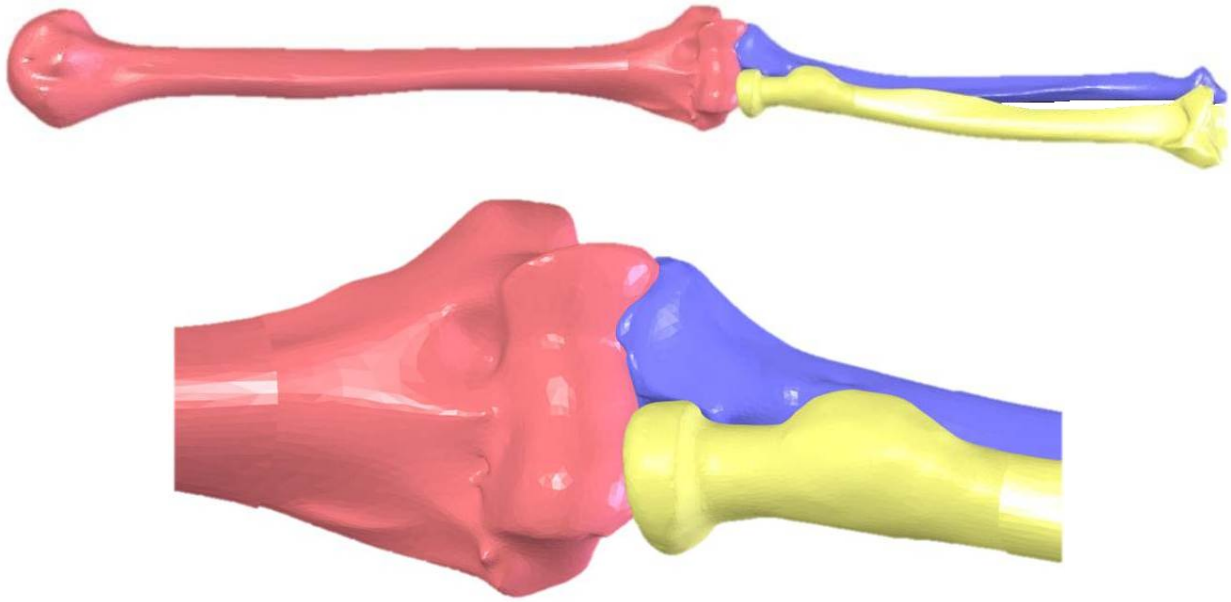

Figure 3.3-1: 3D models of the humerus (red), ulna (blue) and radius (yellow) after importation into SolidWorks, full view and joint close-up

3.3.1. Origins and Insertions

Triangulated surfaces created during the acquisition of 3D bodies resulted in thousands of easily identifiable facets, midpoints of edges, and vertices, each fixed in position on a landmark relative to its respective bone. Thus, multitudes of locations were available to select as origins and insertions for soft tissue. Using anatomic and cadaveric studies, origins and insertions were selected using these triangulated edges and facets [9,23,24,51,52,55,68]. The origins and insertions of ligaments with small insertion sites, such as the LUCL and anterior MCL were modeled as single points on the triangulated surface, positioned at the qualitative center of the attachment to the bone. In contrast, some soft tissue had broader insertion sites, like the interosseous membrane, the triceps insertion on the olecranon, the RCL bands, and the posterior MCL. To accurately simulate this, these structures were represented with

multiple points throughout the breadth of the attachment sites. Applied soft tissue constraints divided between several points simulated these widespread attachments functionally, to most effectively mimic native forces. All ligament and muscle forces were applied as individual force vectors between the designated insertions and origins.

3.3.2. Joint Characterization

Elbow Flexion

After positioning the bones in three-dimensional space as well as defining prominences and soft tissue attachments, it was necessary to implement idealized joints for passive preliminary positioning. Cadaveric experiments often restrain joint position; to this end, proper approximations of motion were required. Two primary motions in the elbow, ulnohumeral flexion and forearm rotation, were simulated. These were defined independent of one another to allow isolated physiologic changes in positioning of the elbow in full three-dimensional space. However, once RBM simulations were begun, these idealized joints were suppressed such that only bony contacts and soft tissue constraints governed the resulting response.

As previously mentioned in Section 2.3, passive elbow flexion was approximated using a screw displacement axis. Though this axis of rotation is qualitatively described as passing through the approximate centers of the trochlea and capitellum, this was quantitatively defined using the high-resolution scanned images of the joint area at 30° and 90° to track the relative movement of the ulna throughout the flexion arc. Two separate assemblies were created using the 30° and 90° scans of the humerus and ulna. Using the MIMICS STL registration feature of Section 3.1.2, the humerus in the 90° scan was overlapped vertex-by-vertex into the exact scan orientation of the 30° file, resulting in complete interference of the two humeri. Following successful registration of the 90° humerus, the

associated ulna was transformed to the coordinate system of the 30° file as well. Thus, when imported into SolidWorks the common distal humerus was used as an anchor to introduce a hybrid assembly of the two ulnas at differing flexion angles.

Three distinct collinear points were defined on each ulna based on geometries characterized by the MedCad module within MIMICS to track the change in position between the two flexion angles. The most proximal point of the coronoid process was marked on each ulna, as well as the centerline of each bone. Another point was defined as the intersection between a line perpendicular to the centerline and another coincident with the tip of the coronoid process. The third defining point was marked 20mm along the centerline proximal from the intersecting point. These three distinct points captured motion of the ulna in 3D space from 30° to 90°, allowing the helical transformation to be determined between them.

Using the methodology described by Beggs (1983), the screw displacement axis was defined using the positions of these three points on each ulna, considered the starting and ending positions to track motion. The calculations behind this ulnohumeral SDA extrapolation were described in detail in previously published work [17,66], using a unique script in MATLAB programming software developed by Fisk et al. (2009). This resulted in the output of a point in Cartesian coordinates intersecting the central axis alongside a directional vector, as well as the pitch of the helix about said axis. The calculated SDA formed an angle of 84.96^{o} with the humeral diaphysis long axis fit. In comparison, the line connecting the medial and lateral epicondyles of the humerus, per ISB recommendations for the axis of flexion for the elbow, created an angle of 83.19^{o}. The MedCAD module also reported the total rotation about the screw displacement axis between the start and end positions as 61.857°, which corresponded well to the flexion angles approximated during scanning. This data was input into SolidWorks to define the ulna's path rotating about the humerus, shown in Figure 3.3-2.

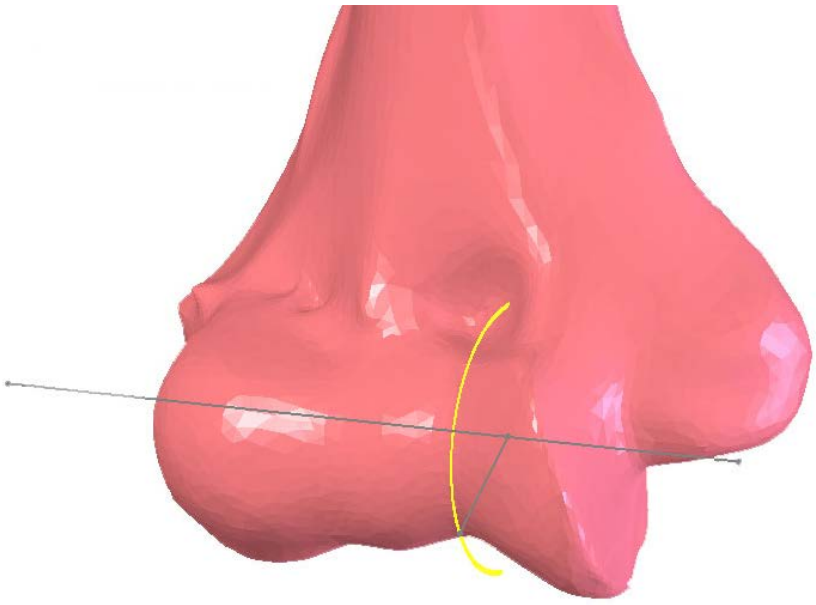

Figure 3.3-2: Distal humerus with SDA axis (grey) and helical path (yellow) visible (anteromedial view)

To position the ulna of the intact joint in discrete flexion angles, the long axes of the humerus and ulna were projected onto a plane normal to the SDA. The angle between the two was measured thereon and thus the ulna was moved about the SDA such that this measured angle equaled the desired flexion angle. Per the International Society of Biomechanics (ISB) recommendations , flexion was defined as positive motion about the SDA [65]. This system indicated that the original position of the 30° specimen had actually been flexed 36.63°, which closely agreed with the approximated motion performed during scanning.

Pronation/Supination

Forearm rotation, or pronation/supination was defined as movement of the radius about an axis which passes obliquely from the center of a sphere-fit of the radial head through the distal ulnar fovea. The MedCad module in MIMICS characterized the geometric center of the radial head as explained in

3.2.3 and the ulnar fovea was determined by inspection. The radius was defined in the model in 3D space with respect to the ulna, as the ulna remains fixed while the radius causes forearm rotation.

ISB recommendations indicated that neutral forearm flexion be defined as when the distal styloids of the radius and ulna are in parallel with the sagittal plane of the body with the elbow flexed at 90° [65]. This definition was implemented in the model as well. Thus, neutral forearm was achieved at 90° such that the palm of the hand would face inward, thumbs turned proximal to the rest of the fingers. Supination required outward rotation of the forearm, causing the long axes of the radius and the ulna to be approximately parallel to one another and the palm facing anteriorly. The converse defined pronation, which resulted in the radius crossing over the ulna so that the palm faced medial and inferior. Pronation is considered as positive forearm rotation. Using these definitions, the scan position of the specimen was positioned in +14.13° pronation.

For positioning of the forearm in specific angles of rotation, the angle was measured between the neutral position and end position of the radius, per ISB recommendations. Points were marked in space defining -80°, 0° (neutral), and +80° to enable fixing of the radius at these specific angles of rotation.

Carrying Angle

The carrying angle is another characterization of position in the elbow, relating the ulnar and humeral long axes projected onto the frontal plane. This angle occurs due to both the tilt of the screw displacement axis, or axis of flexion, and angulation of the ulna, and thus is passive and dependent on the flexion/extension axis [65]. Variation in this motion is referred to as lateral or medial ulnar deviation, or more commonly valgus or varus tilt, respectively, of the forearm.

3.3.3. Local Coordinate Systems

Depending on the cadaveric study at hand and the tools used to implement motion tracking and define axes of motion, sometimes it was necessary to create a novel local coordinate system. Such was the case for the studies replicated using this model, based on the information desired in the cadaveric research [37,38]. This unique joint characterization was first described by Morrey et al. (1989) and described a coordinate system to track the ulna with respect to a fixed humerus using an electromagnetic tracking device. The origin of the system was located at the center of the trochlear groove, which was defined by the cylinder fit outlined in Section 3.2.2 (Figure 3.3-3). A line 'HT' extended from the center of the humeral head to the center of the trochlear groove. The Z-axis was described as normal to the flexion plane, or plane of the SDA, with +z pointed laterally. The cross product of HT and the Z-axis resulted in the Y-axis, which pointed posterior from the joint. Varus/valgus motion of the ulna rotated about this Y-axis. The cross product of the Y- and Z-axes defined the X-axis and completed the orthogonal system; about this axis occurred ulnar internal and external rotation [45].

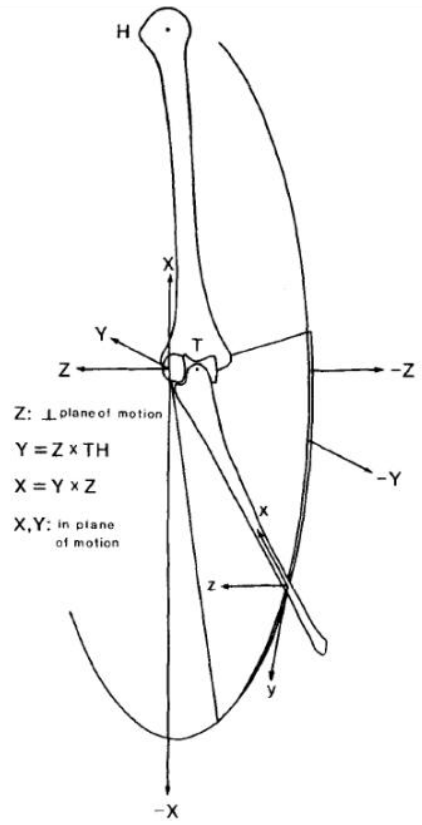

Figure 3.3-3: Local elbow joint coordinate system described by Morrey et al. [45]

3.4. Ligamentous and Capsular Constraints

Because of the stabilizing function of ligaments and their material properties, these soft tissues were modeled as linear tension-only forces with velocity-based damping. Governing equations of function included constant stiffness as well as the application of length-dependent force, per the native function of ligaments. These properties were determined using published cadaveric experiments. Applied ligaments were located in a method similar to the muscles, using defined insertions and origins per anatomical references.

3.4.1. Collateral Ligaments

The lateral collateral ligaments, the RCL and LUCL, shared a common insertion just inferior on the lateral epicondyle (Figure 3.4-1). The RCL was divided into three portions, the anterior, central, and posterior bands, which attached to the midpoint of the thickness of the annular ligament. This expansion of the ligament into three bands accounted for the wide breadth of the radial collateral ligament, as it wraps around the lateral margin of the radial head and incorporates into the annular ligament. The LUCL extended as a single element to the proximal margin of the ulnar tubercle.

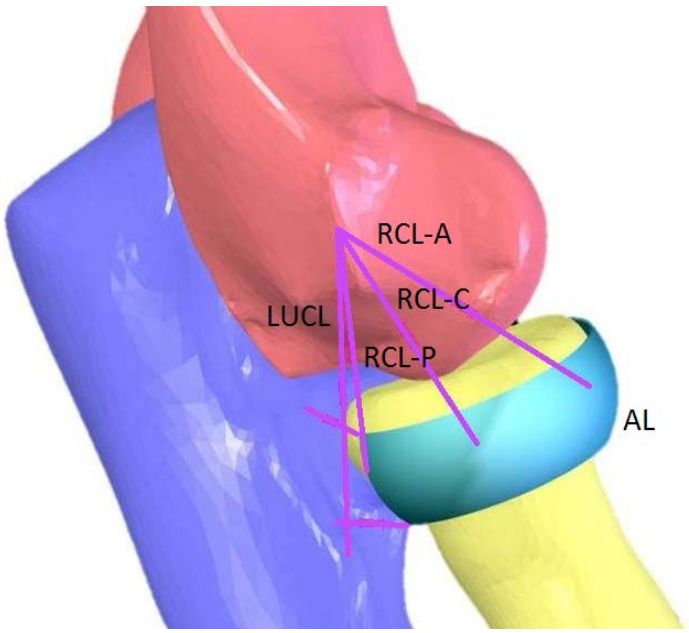

Figure 3.4-1: Lateral ligaments: radial collaterals (RCL-A, C, P), lateral ulnar collateral (LUCL), and annular (AL)

One of the most unique structures in the elbow is the annular ligament: a sturdy ring of ligamentous tissue which wraps around the head of the radius to restrain it to the radial notch of the ulna. It also serves as insertion for several other collateral ligaments, which blend with the tissue to provide stability to the joint. Because of its structure, and the limitations of force wrapping around rigid bodies, the annular ligament was designed by Fisk et al. as a three-dimensional solid structure with ligaments attaching it to the anterior and posterior margins of the radial notch (Figure 3.4-1) [66]. Thus,

full stability could be maintained without the application of artificial restraints to motion, such that the model could be fully governed by soft tissue constraints. This SolidWorks body relied upon a sweep of a silhouette which extended 225° around a central axis, consistent with the length of the native annular ligament. The four solid corners of the body were used as ligament attachments sites to connect the body to the ulna.

The annular ligament body was initially positioned in the elbow by aligning it collinear to the central axis of the radial head, as designated by the MedCad module of MIMICS. However, this mate was suppressed prior to motion simulation, to not apply any unphysiologic constraints to the model. The body was defined with solid body parameters, prohibiting inappropriate interference of the body with the bones of the elbow.

The medial collateral ligament (MCL) was segmented into three distinct bands (Figure 3.4-2). The anterior band of the MCL was applied from the anterior, inferior margin of the medial epicondyle to the medial lip of the greater sigmoid notch. The posterior portion of the MCL was further divided into an anterior and posterior element, originating on the posterior, inferior border of the medial epicondyle and extending to the medial articular rim of the greater sigmoid notch.

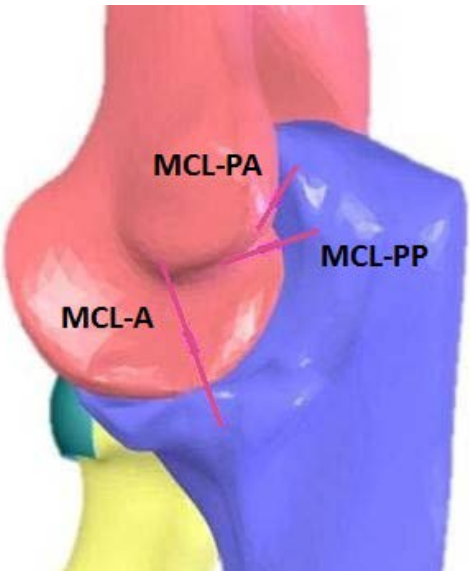

Figure 3.4-2: Medial collateral ligaments: anterior (MCL-A) and posterior (MCL-PA, MCL-PP)

3.4.2. Distal Ligaments

The interosseous membrane of the forearm was defined by further separation of its three bands into five discrete force applications to simulate the diffuse attachments between the diaphyses of the radius and ulna (Figure 3.4-3). The central band of the membrane, located approximately mid-substance between the two bones, was represented as two bands which extended distally from the radius to the ulna. This portion of the IOM was modeled such that the bands met the long axis of the ulna at a 20° angle as according to literature [54], and the perpendicular width of this band was measured as 12.25mm, in accordance with cadaver studies [50]. Dividing the body into two forces allowed a better physiologic representation of the broad attachment of this ligament.

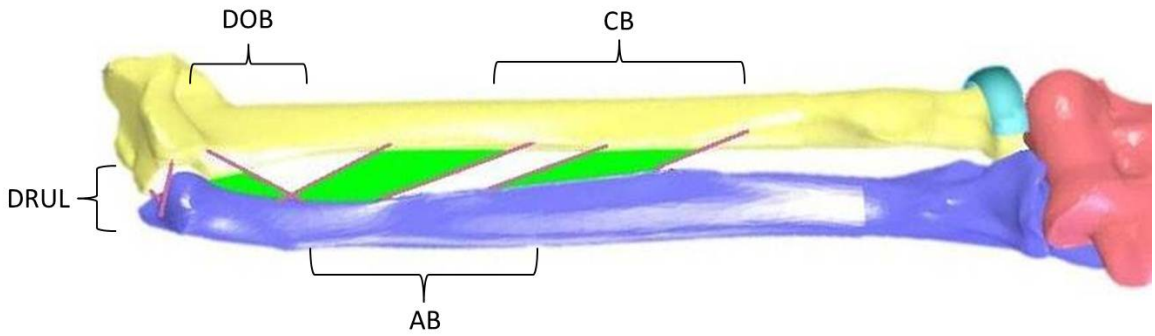

Figure 3.4-3: Distal ligamentous constraints, anteromedial view
(CB: central band; AB: accessory band; DOB: distal oblique, DRUL: distal radioulnar)

The accessory band, in the same coronal plane as the central, was also subdivided into two structures to model its diffuse attachment sites (Figure 3.4-3). Because of its variable location and number of bands in specimens, the portion of the AB modeled was the distal portion, that which appears most consistently [50,54]. This is indicated by the gap between the CB and AB, despite being part of a continuous membrane. The proximal most fiber ran in approximately the same direction as the central band [50] and spanned from the interosseous crest of the radius, distal to that of the ulna. The distal fiber was chosen based on anatomical landmarks, thus the angle became more oblique. Distal to the other bands of the IOM, the distal oblique band (DOB) ran counter to the direction of the CB and AB, passing from the crest of the ulna distal to the inferior margin of the sigmoid notch of the radius (Figure 3.4-3) approximately 30° relative to the long axis of the ulna.

The most distal modeled ligaments were the distal radioulnar attachments (DRUL), divided into a dorsal and palmar band. These are representative of the borders of the TFCC. The dorsal portion extended from the base of the ulnar styloid while the palmar from the ulnar fovea, to insert respectively onto the posterior and anterior radial sigmoid notch.

3.4.3. Joint Capsule

Inclusion of the joint capsule was necessary to impart stability on the model and to fully reflect the soft tissue constraints of an elbow positioned at a low flexion angle. The anterior capsule was added due to its major role in stabilizing the extended elbow, particularly in collateral ligament deficient joints. Conversely the posterior capsule was excluded, as no evidence indicates its role in joint kinematics.

Insertions of the capsule were placed on the annular ligament solid, the coronoid process, and two points on the ulna medial to the coronoid which reflected the expansive coverage that the AC affords to the joint. To determine the effective origins of these fibers, it was necessary to define lines of action for each. Origins on the humerus were determined by demarcating the proximal border of the radial and coronoid fossae and defining lines of action from the insertions, creating a cruciate pattern over the joint. From these, final origins were determined that would reflect the most distal point at which a fiber following this line of action would contact the bony surface of the humerus before crossing joint space to the ulna or annular ligament (Figure 3.4-4). Determination of effective origins as opposed to actual origins was necessary because ligament and capsular forces were applied using mass-less force vectors, and those crossing from the origins bordering the radial and coronoid fossae on the humerus to the insertions on the annular ligament and ulna would result in forces intersecting bony matter. This would result in unphysiologic lines of action and behaviors. Adjusting these origins based upon lines of action allowed for “wrapping” of the capsular forces around the prominences of the humerus, thus ensuring behavior more reflective of the native state.

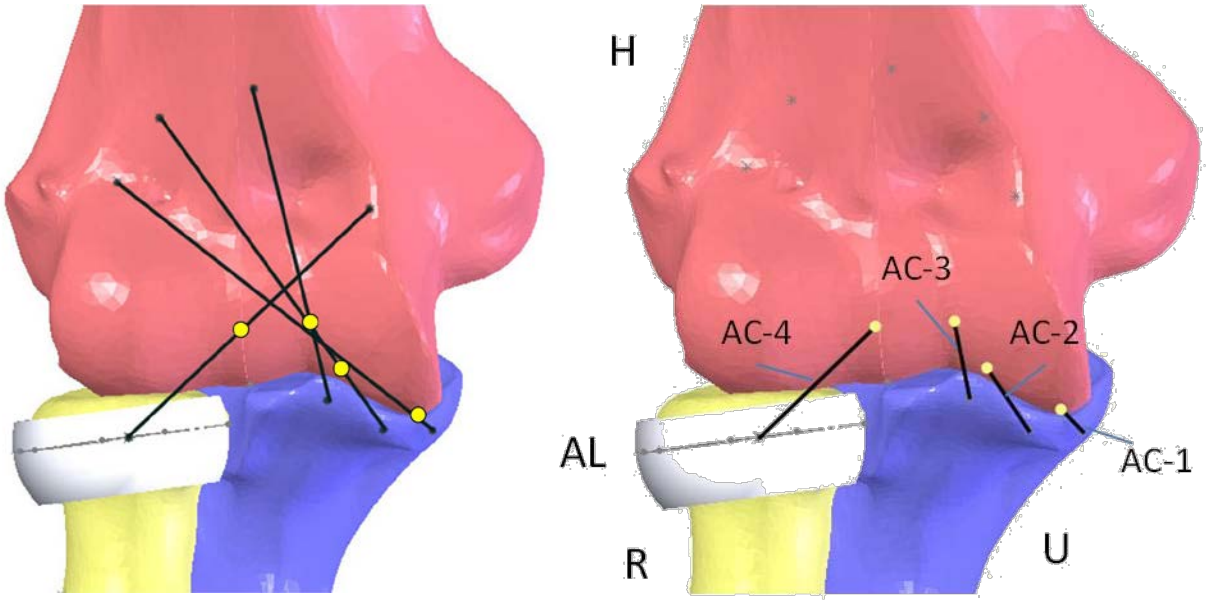

Figure 3.4-4: Lines of action from origin to insertion with marked points for new origins (L) and resultant forces applied to model (R) in the anterior capsule. The R image indicates the humerus (H), radius (R), ulna (U) and annular ligament (AL), as well as each anterior capsule band (AC-x)

These capsular bands were labeled by number, based upon insertion location. Beginning most medial, AC-1, AC-2, and AC-3 inserted on the ulna while AC-4 was oriented transversely to insert on the annular ligament solid (Figure 3.4-4).

Due to a lack of information on biomechanical properties of the capsule, designation of material properties for the anterior capsule involved research of comparative structures. The posterior capsule of the shoulder was deemed a similar tissue in both structure and function. It is described as thin and translucent, much like the anterior capsule of the elbow, and its thickness has been determined as between 0.6-4.47mm [69,70]. Three separate bands within the capsule have been documented and stiffnesses designated for each, described as the inferior, medial and superior posterior bands (PC-I, PC-M, PC-S) [71]. These properties were expanded upon by Elmore (2012) to include width, thickness, length, and modulus of elasticity (E) for each (Table 3.4-1) [20].

Capsular Band	E (N/mm^2)	Stiffness (N/mm)*	Width (mm)	Thickness (mm)	Length (mm)
PC-I	56.8±39.8	15.36	8.47	1.3	40.7
PC-M	44.9±22.8	14.95	8.47	1.6	40.7
PC-S	28.4±16.5	13.59	8.47	2.3	40.7

Table 3.4-1: Posterior shoulder capsule band material properties (Bey 2005*, Elmore 2012)

A study directly comparing the shoulder and elbow capsules considered their structures with electrophoresis and material properties under tensile loading, with muscles excised and ligaments intact. Similarity between the types of collagen bundles and individual fibrils within the shoulder and elbow capsules was found. Upon mechanical testing, the shoulder capsule demonstrated more elasticity, though it was revealed that the force to rupture the capsule decreased significantly in older specimens. In specimens similar in age to the cadaveric specimens used in studies performed by Chanlalit (2011, 2012) with respective mean ages of 82 and 76 years of age, the failure loads were similar between the shoulder and elbow capsule. It was also determined that the shoulder capsule thins with age [37,38,72].

A study performed by Cohen et al. on the structure of the elbow capsule after trauma determined that in control specimens with an average age of 63 years, capsular thickness was 0.6 ± 0.2 mm. Gross examination also described the capsule as “thin and of uniform thickness” [47]. Another determined joint capsule thickness in adults over 15 years of age as approaching 2mm [73].

Using the properties described for the shoulder capsule and the discussed similarities to, and differences from those in the elbow, the mechanical properties for the elbow capsule were determined. A thickness of 0.6mm was assigned to the capsule based upon the results of Cohen et al. and Hogan et al., as well as the comparison between the shoulder and elbow thicknesses in Kaltsas et al. [47,72,73]. Given that in older specimens, the behavior of the shoulder and elbow capsule are similar, the average modulus of elasticity was taken from the moduli of the three shoulder bands equaling 43.3667 N/mm^2 and used as the modulus of the elbow capsule. The width of each band was determined using the

distance which would cover the breadth of the joint capsule effectively and dividing it equally between the individual components. This overall distance was 26.58mm based upon the scanned cadaveric specimen. The bands which inserted most medially were assigned a width of 1/5w. The single band oriented mediolaterally was assigned a width of 2/5w to accurately represent the space assigned to it. The length of each band was taken to be the measured distance between the insertion and origin in the model, such that the bands had 0% strain as no data exists regarding in situ strain within the capsule. Using the given width (w) and thickness (T) to determine cross-sectional area (A), the length (L), and the modulus (E), stiffnesses (k) were calculated using Equation 1, resulting in the properties listed in Table 3.4-2.

$$k = \frac{EA}{L} \qquad \text{Eq. 1}$$

Another component of the joint capsule added was the distal portion of the capsule, which attaches the annular ligament to the body of the radius as described in Section 2.2.3. This was done to ensure stability of the annular ligament and prevent shifting of the solid body over the native radial head as well as the smooth surfaces of the implemented radial head replacements. Two bands originated along the midsection of the annular ligament to represent their absorption into the bands of the AL. These then angled downward and towards each other slightly to insert opposite the most anterior border of the radial tuberosity. A triangular shape was formed between the two bands, as per anatomical texts. They were labeled the anterior and posterior band of the distal capsule (DC-AB, DC-PB), with DC-PB oriented most medially with the forearm in 80° supination (Figure 3.4-5).

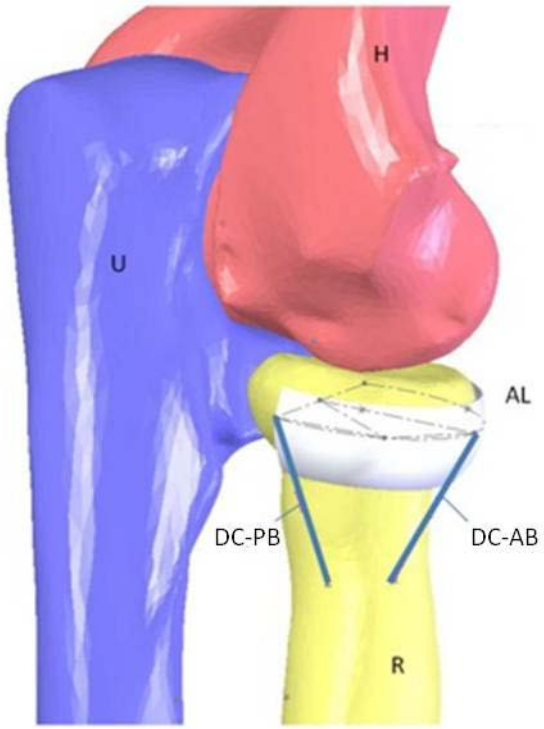

Figure 3.4-5: Posterolateral view of elbow, with humerus (H), radius, (R), ulna (U) and annular ligament (AL) labeled, as well as distal capsules (DC-AB, DC-PB)

Properties for the distal capsule bands had been previously undetermined. Thus, the length for each band was determined as equal to the measured length between the insertion and origin such that the band was under 0% in situ strain. Each band was also assigned a width of 6.82 mm based upon the measured distance between their insertions and appropriate coverage without overlap. Thickness and modulus of elasticity were assumed to be the same as in the anterior capsule, as this was considered a continuation of the capsule distal to the annular ligament. Using these values in Equation 1 resulted in the stiffnesses listed in Table 3.4-2.

Capsule Band	Abbr.	Width (mm)	Thickness (mm)	Modulus (N/mm^2)	Length (mm)	Stiffness (N/mm)
Anterior Capsule (1)	AC-1	5.316	0.6	43.3667	4.58	30.2014
Anterior Capsule (2)	AC-2	5.316	0.6	43.3667	8.14	16.9929
Anterior Capsule (3)	AC-3	5.316	0.6	43.3667	7.68	18.0107
Anterior Capsule (4)	AC-4	10.632	0.6	43.3667	15.8	17.5092
Distal Capsule, Anterior Band	DC-AB	6.82	0.6	43.3667	16.51	10.7484
Distal Capsule, Posterior Band	DC-PB	6.82	0.6	43.3667	17.63	10.0656

Table 3.4-2: Material and Mechanical Properties of Joint Capsule Bands

3.5. Motion Parameters

The COSMOSMotion add-in for SolidWorks was utilized for simulating motion and calculating results for this rigid body model. This feature integrates tools into SolidWorks that allow the application of forces, torques, and displacements to rigid bodies over a defined amount of time in a series of methods. It is also possible to constrain bodies using three-dimensional contact parameters and inter-body connections such as springs to simulate motion. The add-in can define types of joints between bodies to limit degrees of freedom and calculate resultant motions, forces, contacts, velocities, and myriad other results from applied motion. Because of its integration with SolidWorks, no previously defined positioning or orientations were lost in the utilization of this feature.

It was necessary to define several key parameters prior to simulation. The primary step regarded defining bodies as moveable or fixed in the system. The fixed or "grounded" body was a modeled version of the armature of the experimental setup, later described in Chapter 4. This limited the body to no degrees of freedom and maintained its position throughout all rigid body modeling. The humerus, radius and ulna were defined as free, moveable parts and were thus able to move freely throughout all six degrees of freedom, constrained only by soft tissue and bony contact. Gravitational forces oriented with respect to the grounded armature were applied to each bone at its centroid.

The application of mechanical joints in COSMOSMotion limits movement of bodies relative to one another by removing specific degrees of freedom. Though these apply unphysiologic restraints to the bodies, they can be utilized to apply external perturbations or limitations present in a cadaveric experimental setup.

3.5.1. Mechanical Properties

Critical to proper model behavior was the designation of ligament mechanical properties, including the in situ strain, stiffness, and stress-free length. These values were determined based upon published cadaveric data (Table 3.5-1).

Ligament	Abbr.	Stiffness (N/mm)	In Situ Strain (%)	Tension-Free Flexion Angle (α)
Annular, Anterior Distal	AL-AD	28.5	2.0	n/a
Annular, Anterior Proximal	AL-AP	28.5	2.0	n/a
Annular, Posterior Distal	AL-PD	28.5	2.0	n/a
Annular, Posterior Proximal	AL-PP	28.5	2.0	n/a
Lateral Ulnar Collateral	LUCL	57.0	n/a	107°
Medial Collateral, Anterior	MCL-A	72.3	n/a	22°
Medial Collateral, Posterior Bundle, Anterior	MCL-PA	26.1	n/a	80°
Medial Collateral, Posterior Bundle, Posterior	MCL-PP	26.1	n/a	110°
Radial Collateral, Anterior	RCL-A	15.5	0.5-1	43°
Radial Collateral, Central	RCL-C	15.5	0.5-1	30°
Radial Collateral, Posterior	RCL-P	15.5	0.5-1	85°

Table 3.5-1: Ligament Mechanical Properties

The stiffnesses utilized for the model were applied as N/mm of elongation and selected based on cadaver research as described in Spratley et al. (2009) [17]. The medial collateral ligament was modeled such that its bands remained taut throughout the flexion arc, as suggested in Fuss et al. (1991) past its tension-free flexion angle [74,75] using an iterative process to ensure stability. Stiffnesses of other flexion-angle dependent ligaments were derived from Regan et al. (1991) [75].

In situ strains were applied to isometric ligaments based upon published values wherever possible, particularly within the distal constraining ligaments. Ligaments without published in situ strains but known to be isometric were modeled as having 2.0% strain, per Liacouras et al. (2007) [18]. This approximation was applied to the annular and distal radioulnar ligaments. The tension-free flexion

angles were derived from the research of Regan et al. (1991) [75], and the collateral ligaments were pretensioned with 0.5-1.0% strain to dampen the model and resist oscillations.

The stress-free lengths of the elements with in situ strains but no reported stress-free length for a given flexion angle, specifically the annular ligaments were calculated using said in situ strains applied to the Lagrangian Equation 2:

$$L_0 = \frac{L}{1+\varepsilon} \qquad \text{Eq. 2}$$

where L was the distance between the origin and insertion and ε was the in situ strain of the given ligament.

Ligaments that were flexion-angle dependent, particularly the collateral ligaments, had a defined stress-free length at a given flexion angle, as indicated in Table 3.5-1. Thus, the stress-free length was measured manually in the model for each ligament only after the model had reached an equilibration due to applied ligament tension at each collateral ligament's respective active flexion angle, without other applied forces. The model was allowed to settle in order to prevent the inevitable ringing as lax ligaments suddenly became taut. These measured stress-free lengths were then tested by iterative solving of the model at incrementally increasing stress-free lengths to verify that the model was evenly constrained by the various ligaments and reached equilibrium.

3.5.2. Ligament Modeling Expressions

Ligaments were modeled as linear force elements which were initially tensioned through the application of in situ strain and/or a stress-free length. Though the features of COSMOSMotion easily allow the application and measurement of myriad variables within the RBM, it was necessary to find a method of incorporating the mechanical properties of ligamentous soft tissue to accurately predict

behavior of the elements. A single governing equation for the mechanics of ligaments that combines element tensioning, movement, damping, and stiffness in calculating applied resisting force had to be determined. The FORTRAN programming language, recognized for its high-performance computing, was utilized within COSMOSMotion to blend these variables into a single concise entity, which designated the applied force within an element as related to the change in length of the ligament and its inherent stiffness.

Ligaments with a defined in situ strain were modeled using the designated origins and insertions mentioned in Section 3.4 as markers, and the COSMOSMotion resultant expressions measured the 3D distance between these markers during motion simulation. A logic statement was applied to govern the force applied by the ligament based on the change of length of each element, given in Equation 3.

$$T = IF\ \left(DM(P_1, P_2) - L_0 : 0, 0, -S * (DM(P_1, P_2) - L_0) - 0.1 * VR(P_1, P_2)\right) \quad \text{Eq. 3}$$

Thus, the tension within the ligament is applied with respect to the magnitude of the distance between the insertion and origin points, *(DM(P1, P2))*, minus the user-defined stress-free length *(L_0)* for length changes less than, equal to, or greater than 0, such that:

$$T = \begin{cases} 0, & L - L_0 < 0 \\ 0, & L - L_0 = 0 \\ -S * \Delta L, & L - L_0 > 0 \end{cases} \quad \text{Eq. 4}$$

where S is the stiffness in N/mm per cadaveric data and L is the length in millimeters observed between the insertion and origin at a given moment in time. It is of note that the force generated when the length of an element surpasses its L_0 is defined as negative due to the direction of forces defined by convention within Solidworks. The negative definition causes the force to pull the origin and insertion toward one another as opposed to pushing them apart.

The third component of the FORTRAN statement was the inclusion of a velocity-dependent damper on the ligament, preventing a rapid tensioning of the ligaments during motion simulation. This further served to prevent high-frequency ringing of the model and allow faster solving of the motion study. The *VR*, or relative velocity term as seen in Equation 3 as ($VR(P_1,P_2)$) measured the velocity of movement between the origin and insertion of a given ligament, and applied a resistance to motion of the damping coefficient 0.1 N*s/mm. Addition of this feature was intended as linear damping not completely indicative of the time-dependent viscoelastic behavior native to soft tissues. Its inclusion served to bolster the stability of the model in a manner that would have no effect on the results of the computational study.

3.6. Contact Parameters

As this rigid body model was fully reliant on physiological limitations and not approximated joints, contact parameters between bodies were critical to honoring osteoarticular geometry during simulations. Definition of surface to surface contacts was performed for each of the long bones of the arm as well as the modeled annular ligament body, thus limiting motion between these bodies. The 3D contacts feature in COSMOSMotion allowed for user input for material properties and regulated penetration upon contact (Figure 3.6-1). Also enabled in this feature was the containing of contact pairs, thus defining contact parameters between specific bodies while allowing penetration for others, as well as labeling places of interest for results calculations.

Figure 3.6-1: COSMOSMotion interface for 3D contact parameters with user-designated values

The stiffness for the bodies was chosen as 8,000 N/mm to minimize body interference at bony articulations. This value also minimized integration issues, which became prevalent as the stiffness increased due to the method by which COSMOSMotion calculates the restoring force after two bodies overlap. COSMOSMotion iteratively solves for interference between designated bodies and compares the overlap with the maximum allowed penetration. In the occurrence of interference, the program calculates penetration distance as well as the volume of overlap, considering exact triangulated surfaces, and applies an outward force on both intersecting bodies at the geometric centroid of the overlap. The magnitude of this applied force is calculated as the product of the penetration distance in millimeters and the user-defined material stiffness of the body in N/mm. Stabilization for this force is provided by a viscous element utilizing an exponent applied to the penetration distance, and the specified maximum damping is the boundary for the damping applied to the system as a function of the rate of interference, or velocity.

Application of friction was another feature of the contact parameters, but the presence of synovial fluid in the native elbow between the articulating surfaces renders friction nearly negligible [76,77], and thus friction was not added to the model.

3.7. Solver Parameters

The behavior of bodies defined as moveable was calculated iteratively using algorithms of through the MSC ADAMS solver embedded within the COSMOSMotion add-in. The equations of motion were applied to these bodies within the model, utilizing user-defined solver parameters. Though a number of integrators are available within the software package, the “Gear Stiff Integrator” (GSTIFF) is the default method and was selected for its capabilities to solve “stiff” ordinary differential equations

(ODEs) in a concise and robust manner. Stiff ODEs are so named for the extremely small time step necessary to solve these equations by particular numerical methods, especially in systems with high oscillations [78], thus leading to poor and slow solution calculation. The GSTIFF algorithm accounts for this by applying a backwards differential formulation, a variable order method to predict the error of the system within a user-input step size range. Thus, this algorithm is able to more rapidly solve the displacements of the model by dynamically adjusting and decreasing the time step to model short-term events such as body contact, despite oscillations [79].

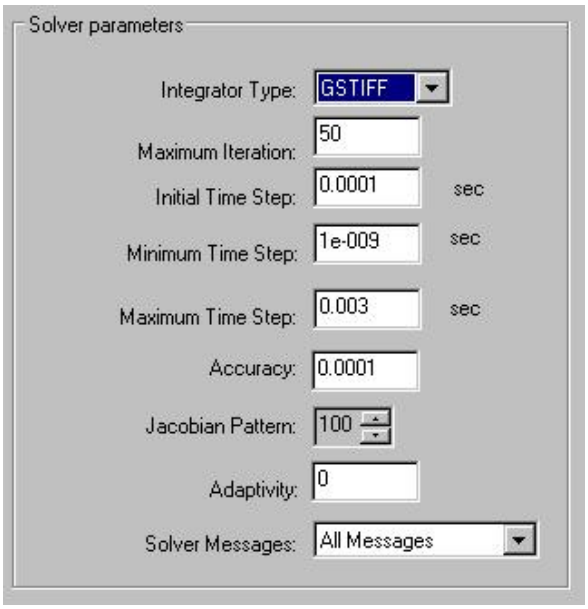

Figure 3.7-1: COSMOSMotion interface for solver parameters with user-defined values

Other user-defined parameters were selected for the solving of the system within the ADAMS package (Figure 3.7-1). These values were chosen based upon those default to the software package, as well as by trial and error for model stability. The minimum time step was set to the minimum possible value to capture any possible movement in the model, as was the accuracy threshold. The Jacobian pattern was set to its maximum, indicating the frequency at which the matrix was re-evaluated to give maximum accuracy, despite the slowing of computational time. Adaptivity was set to its minimum to

allow the inclusion of all rigid body contact in each subsequent time step [79]. The combination of these parameters enabled the integrator to solve for movement of bodies accurately, with the calculation of even the minutest of contacts with the least amount of error in an efficient and time-effective method.

4. RADIOCAPITELLAR STABILITY WITH BI- AND MONOPOLAR RADIAL HEAD PROSTHETICS

4.1. Overview

To demonstrate the capabilities of the developed elbow rigid body model, it was first validated against a cadaver study performed by Chanlalit et al. (2011) entitled “Radiocapitellar stability: the effect of soft tissue integrity on bipolar versus monopolar radial head prostheses” [37] to examine how soft tissues would contribute to stability of the radiocapitellar joint for different radial head replacements. Cadaver specimens were subjected to implantation of a bipolar radial head prosthetic, modifiable into monopolarity via a custom-designed stabilizing cuff. Displacing motions were applied to the radius while axial loading was applied to the humerus, and the subluxating force was quantified in both the intact ligament and lateral tissue insufficient states. It was demonstrated that the force-displacement trends of the monopolar radial head more accurately represented the intact state than the bipolar in both ligament states. The study showed statistically that in the intact state the monopolar prosthetic had greater overall stability. Chanlalit also indicated that the bipolar prosthetic had a greater dependence on lateral soft tissues for stability than the monopolar, further enforcing the evidence that the monopolar prosthetic is superior in enhancing elbow stability [37].

4.2. Experimental Method

Twelve fresh frozen cadaver elbows were utilized, including six male and six female specimens with an average age of 82 years. Skin and muscles were removed, maintaining integrity of the full joint capsule around the elbow. A sagittal step-cut osteotomy of the lateral condyle was performed to allow radial head replacement, and was rigidly fixed with two compression screws. Replacement of the radial head prosthetics was achieved by removal of the screws and lateral condyle for access, and fixing the osteotomy once again. Radiocapitellar stability was tested before the osteotomy as well as after the specimen was reduced and fixed to compare these states and to isolate the effects of the radial replacements.

The common press-fit Tornier SA bipolar radial head system (RHS) implant (Tornier SA, Saint-Ismier, France) was chosen for the experiment, designed to allow ±10° bipolar tilt. The head of this system is considered non-anatomic due to its circular shape and the evenly distributed concavity on its proximal surface, the depth of which reaches 1mm. The bipolar prosthesis was converted by Chanlalit into monopolar by way of a removable custom-designed metal collar, attached to the radial neck region to prevent tilt of the radial head component. Though the RHS is available in a variety of radial head lengths, the appropriate size was selected by measuring and matching the short radius of the native head to the manufactured head size closest to but not surpassing this length. Accurate radial neck length was replicated by measurement of the collar and prosthetic size, and resection of the corresponding amount of native bone [37].

To properly align the specimen, the humerus and proximal radius were potted using polymethyl methacrylate (PMMA) and affixed to a custom-designed materials testing apparatus [80]. The humerus was rigidly attached to the device mounted on a vertical slide in the Y-direction while the proximal radius was allowed to hang freely within an aluminum tube mounted on the load cell beneath.

Alignment of the radiocapitellar joint was established as the position to which the radius settled due to gravity, and the radius was then attached from this position to a 6-axis load cell. The definition of motion axes was determined based on the proximal surface of the radial head, so the radius was potted in a position such that this surface was positioned along the horizontal. The humerus was then positioned and fixed in 30° flexion with respect to the radial head proximal surface and the radius was aligned such that the radial tuberosity was oriented medially with the forearm in supination. The stage to which the radius was fixed allowed motor-driven and computer-controlled translations in the horizontal XZ-plane.

For radial head comparison, a mono- or bipolar replacement was selected at random and inserted into the specimen, the osteotomy was fixed again and testing progressed. The untested radial head replacement was utilized for a second run, and results were compared. Random selection of the radial head replacement prevented variation as a result of the testing sequence. Comparison of the dependence of bi- and monopolar RH prosthetics on soft tissue integrity was derived from cutting and surgical repair of the lateral ligaments. The lateral collateral ligament complex, involving the LUCL, RCL, and the overlying extensor tendon were detached from the lateral epicondyle; these were repaired using an Arthrex 5.5mm corkscrew suture anchor and two sutures. Radial head prostheses were modified by untying the sutures for access, after which they were retied and testing resumed. Thus, the study was performed upon eight separate specimen states: pre-operative intact (control), native radial head post-osteotomy fixation (surgical control), bipolar and monopolar radial head replacements with reduced and fixed osteotomies, bipolar and monopolar replacements with lateral soft tissues detached, and the two radial head replacements with lateral soft tissues repaired.

Testing was performed by applying axial loading of 50 N upon the humerus with simultaneous translation of the radius 6mm from starting position at a rate of 2mm/s. After each translation, motion

was reversed to return the radius to its original position and continue 6mm in the opposite direction, limiting motion to the sagittal plane. Two cycles of subluxating motion were applied to the specimen and resisting forces were measured at a sampling frequency of 45 Hz. The second cycle was utilized for data analysis [37].

4.3. Computational Method

4.3.1. Overview

The design of the computational model in 3-D space replicated that of the Chanlalit et al. cadaveric study. Within the SolidWorks design space, components were created that reflected the materials testing apparatus of the experimental setup and the radius, ulna, and humerus were attached relative to these structures in the same orientations described. Ligaments present in the cadaveric study as well as a joint capsule were activated, which included the annular ligament bands, the LUCL, posterior and anterior MCLs, and RCLs. Reflected in the modeled humerus was a fixed-in-place humeral osteotomy like that in the experimental design. The Tornier SA radial head replacement system (RHS) was also modeled and affixed to the radius per manufacturer's instructions, such that it could be incorporated to model the elbow after implantation or removed to model an intact joint with the native radial head. Force and displacement were applied to the humerus and radius respectively, and the restraining loads in the X-direction, i.e. the direction of displacement, were collected for the intact, monopolar RHS, and bipolar RHS states. The rate at which the model was displaced was identical to that in the experiment, though only posterior displacement was performed as results were not published for applied motion in the anterior direction [37].

4.3.2. Materials Testing Apparatus

Experimental specimens were mounted into a testing apparatus to ensure alignment and control motion, which was replicated in the computational study using two structures as shown in Figure 4.3-1. The primary structure was a base representing the overall apparatus, providing a definition of posterior displacement and axial loading using its local coordinate system. Its position also defined the direction of gravitational forces applied to the bony components. This construct consisted of a simple platform measuring 268mm x 200mm x 30mm, across the surface of which a second feature slid and displaced. The platform was fixed in space based upon the inherent coordinate system defined within the design space of SolidWorks. The second component, referred to as the stage, consisted of a smaller platform as well as a hollow cylinder representing the XZ stage of the experimental setup and the fixture for retaining the radial shaft in the Y-direction. This was done in contrast to the design of the cadaveric study, which placed the stage in the XY-plane. The stage was constrained onto the surface of the fixed platform to translate only in the X-direction. Using this stage, displacement of the radius was defined [37].

The experimental setup of the cadaveric study also included a restraint for the humerus which limited it to axial translation. Due to the available motion constraints within the SolidWorks COSMOSMotion module, it was unnecessary to create this structure. The humerus' appropriate position was determined based upon positioning of the radius within the stage, and its axial translation was defined and constrained with respect to the platform (Figure 4.3-1) [37]. Its motion was defined in the Y-direction, which differed from the cadaveric study defining this as the Z-direction, though it did not affect the results of the model read in the X-direction.

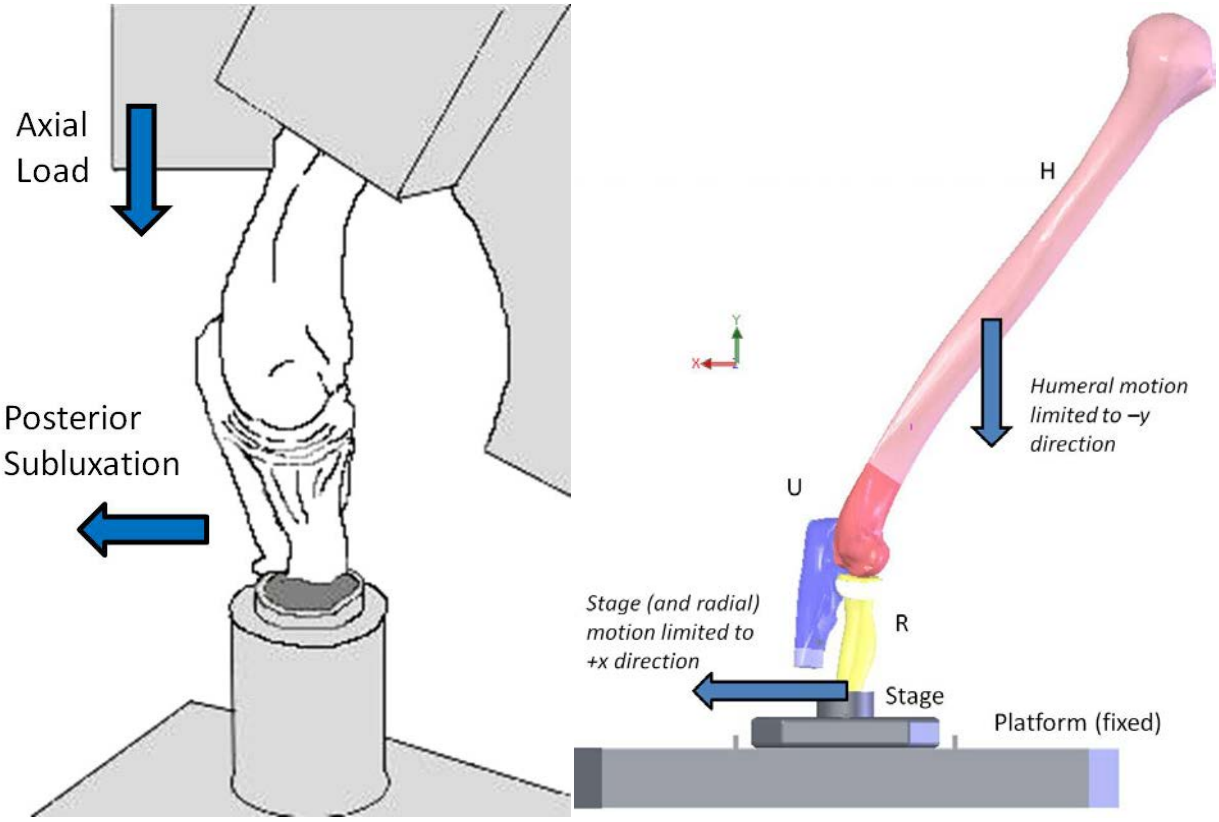

Figure 4.3-1: Rendering of experimental setup (right) (Chanlalit 2011, 2012) and computational Materials Testing Apparatus platform and stage with radius, ulna, and humerus in position (left)

4.3.3. Radial Head Replacements

A key component to the experimental design was the Tornier RHS, a radial head prosthetic. It has been designed to maximize the contact between the radial head and the capitellum of the humerus by implementing a bipolar head, allowing ±10° axial tilt on its straight neck. The head is perfectly circular, modular and composed of cobalt chromium (CoCr) with an internal polyethylene liner. There are four possible options for head diameters, ranging in two millimeter increments from 18-24mm. The radial head height was limited to 12mm, the only option in this particular RHS. Also critical to the design was the symmetrical concavity on the proximal surface of the radial head, which reached a maximum depth of 1mm. The short press-fit stem, used in the cadaveric experiment, is also CoCr but coated with a titanium (Ti) spray to provide purchase to the bone. An array of possible stem diameters range from

6-10mm in 1mm increments with stem lengths between 21-24mm. This, according to manufacturer's surgical instructions, accommodates neck resection levels of 13mm and 16mm. Using the provided dimension charts within the manufacturer's surgical technique pamphlet, a stem and radial head were created as individual parts (Figure 4.3-2). The appropriate radial head and stem diameters were selected based upon manufacturer's instructions, resulting in a head diameter of 20mm, a stem length of 22mm and a stem diameter of 6mm. The concavity on the component's proximal surface was modeled as well [81].

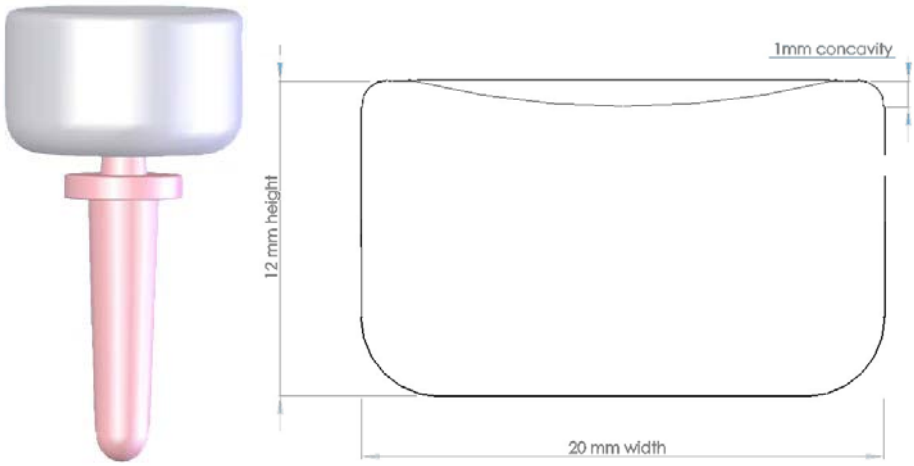

Figure 4.3-2: Tornier RHS stem and attached head (left) and isometric view of head with dimensions (right)

Within the cadaveric study, both a mono- and bipolar radial head system was implemented by the creation of a metal collar attached to the bipolar Tornier RHS between the stem and the articulating head, restricting its motion [37]. To accomplish this in the model, the radial head was fixed in position relative to the stem, creating monopolarity by prohibiting its motion. In modeling the ±10° of tilt within the bipolar design, a conical structure with 10° angulation was created and fixed relative to the stem with its tip coincident to the center of the distal side of the head (Figure 4.3-3). Motion of the head was limited by solid contact parameters to the surface of the cone, allowing the head to tilt in any direction

that resulted in an angle less than or equal to 10°. This cone did not affect any other components of the model, as contact parameters were defined only with respect to the radial head and not to any other feature.

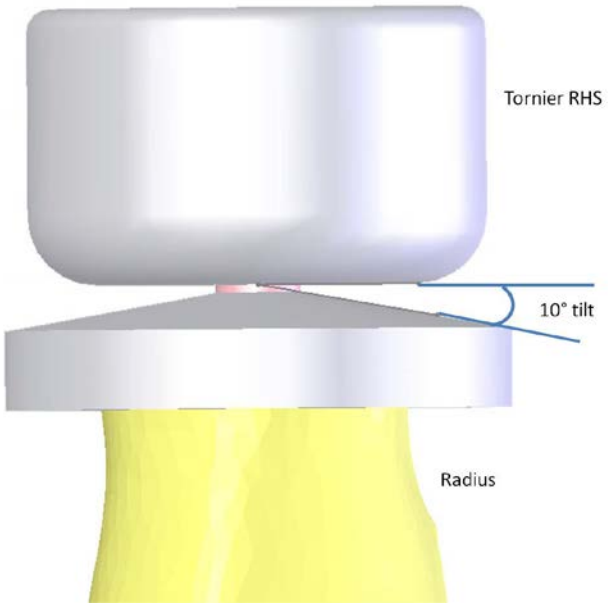

Figure 4.3-3: Tornier RHS, bipolar set-up with ±10° shown

To implant the radial head replacement, an axis fit to the shaft of the radial neck was implemented using the MIMICS MedCad module and a plane normal to this axis was created at the most proximal point of the radial head (MPPRH). A cut plane was defined parallel to this plane and positioned 17mm distal from the MPPRH. The Tornier head long axis was aligned with the long axis of the neck, and the collar portion of the stem was fixed to the cut plane. The radial head replacement was positioned vertically such that its most distal surface was 5mm from the cut surface, ensuring with a 12mm head height that the overall height of the replacement construct equaled 17mm. This differs from the suggested cut plane within the manufacturer's surgical procedure in that the stem is designed for a cut plane at either 16mm or 18mm from the MPPRH, though the suggested determination of the

plane is the same. Though this specific specimen's head and neck would clinically call for a 16mm cut height, 17mm was utilized for the purpose of visualization; the radial head replacement however was positioned such that there was no shortening or understuffing of the radial head replacement, achieving an identical end for computation as with a 16mm cut.

In the monopolar experimental design, the RHS was fixed in place to the radius and combined into a single assembly. Thus, the construct behaved as a single entity with continuous contact parameters, and the head was prevented from moving relative to the radius. In contrast, the bipolar RHS was assigned as a distinct part in the model, separate from the assembly of the radius, and a spherical joint was implemented to allow full tilt of the head while maintaining its position relative to the radial neck. Fixing the conical structure restricting the bipolar head's motion to 10° tilt to the radius provided the RHS with its tilt limitations while moving as one single body with the radius.

4.3.4. Computational Implementation of Experimental Setup

The humerus was subjected to a fixed step-cut osteotomy within the SolidWorks design space, approaching from the lateral side 60 mm from the most distal point of the capitellum and cutting to the midsection of the medial body of the trochlea to maintain the integrity of the capitellum. A total of 1.2 mm of bony tissue was removed from the vertical cut to represent the kerf of the average small sagittal or oscillating bone saw. The experimental method involved the pre-drilling of screw holes to maintain the intact height of the capitellum, so the fragment was fixed at its original height and not shortened the width of a saw blade (Figure 4.3-4).

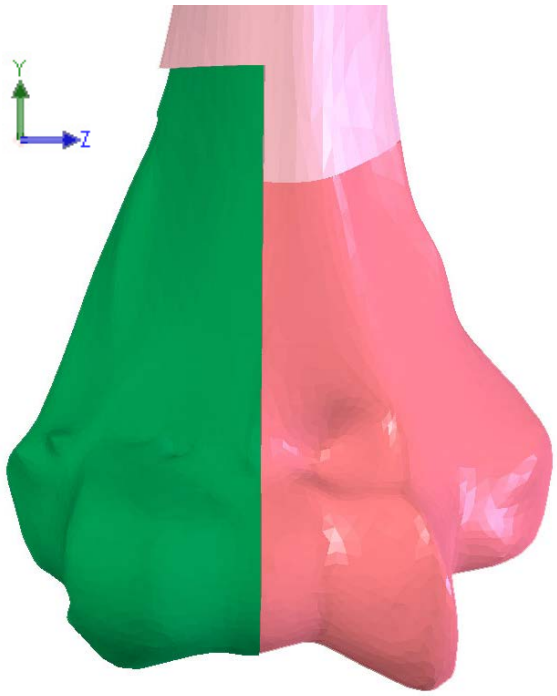

Figure 4.3-4: Anterior view of humerus with post-osteotomy lateral fragment (green) fixed in position 1.2mm medial to the body of the humerus (pink), with height maintained

The radius was attached to the stage at a level that, by visual inspection, reflected the positioning of the radial fixation in the cadaveric experiment. The radial shaft was cut at the same level as in the study to prevent interference between the distal radius and the stage or platform. The radius was positioned into 80° of supination, orienting the radial tuberosity medially per the experimental setup. A planar fit of the proximal surface of the radial head was aligned parallel with the XZ-plane, reflecting the note in Chanlalit et al. that the radial head surface was aligned with the capitellum, thus ensuring its displacement in the X-direction [37]. Both the ulna and humerus were positioned relative to the radius; the humerus was angled using the screw displacement axis such that the forearm was in 30° flexion. The diaphysis of the ulna was cut at such a level as to allow it to move beside the radius without interacting with the stage.

Mechanical testing within the experiment involved a 50N axial load applied to the humerus while a 6mm displacement was applied to the radius via the platform at a rate of 2mm/s, moving

posteriorly said distance first then displacing 6mm anterior for two cycles [37]. In the computational analysis, a 50N load was applied to the humerus in the Z-direction over one second followed by a one second rest period, allowing the computational model to reach equilibrium before the application of the radial displacement. A mathematical function governed this motion in COSMOSMotion, as designated by an equation controlling force application, STEP (0, 50, 0, 1). Movement in the radius was defined as 6mm displacement in the posterior direction at the given rate of 2mm/s governed by the expression in equation STEP (0, 2, 6, 5). This statement harkened the STEP feature embedded within COSMOSMotion which determines the slope between the initial value, 0mm at 2 seconds, and the designated end value, 6mm over the period of time designated, 3s. This resulted in a 2mm/s displacement of the radius in the X-direction for a total of 6mm, at which time motion ceased and a one second equilibrating period occurred.

In contrast to the experimental design, the anterior displacement was not modeled. Results of anterior motion were not published in this paper as interest for the authors lay in posterior subluxation of the radius after radial head replacement. Also, the cyclical nature of the cadaveric study, used to eliminate hysteresis in the viscoelastic ligaments and provide accurate data in the second cycle, was unnecessary in the computational model due to the exclusion of viscoelastic behavior.

In running the computational model, it was discovered that a laxity existed in the ulna's constraints such that it was able to move posteriorly an unphysiological amount. To provide additional stability, a band of soft tissue was modeled between the shafts of the radius and ulna. Descriptions of the cadaveric experimental method and images contained therein suggest that soft tissue related to the interosseous membrane was maintained between the radius and ulna, despite cutting of the bones proximal to the explicit IOM-CB. This membrane was represented by a tether, which was positioned such that it would not cause unnecessary twisting of the ulna (Figure 4.3-5). Its stiffness was derived

based upon a series of published cadaveric studies relating the tensions and thicknesses of the respective bands of the IOM, which determined that the central band of the IOM has a stiffness of 65N/mm [51,82]. The stiffness assigned to the tether was set to be identical to the central band based upon its proximity to this band and its identical function. Stress-free length was determined as 11mm through an iterative process used to affirm that the force generated in the band would not exceed 1N so as not to skew the computational test results.

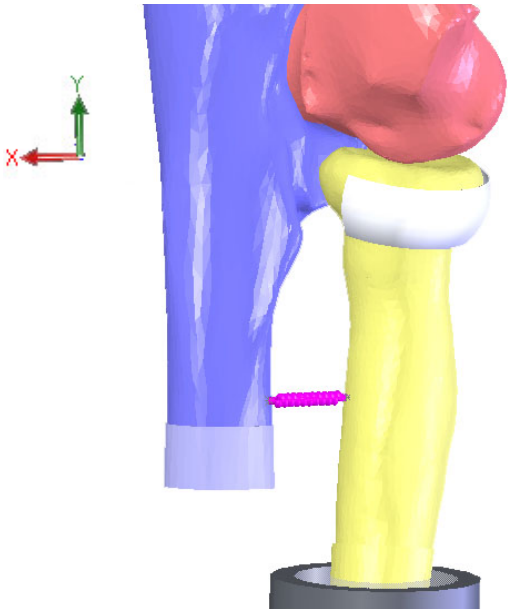

Figure 4.3-5: Ulnar tether (pink) positioned between the radial (yellow) shaft and ulnar (blue) shaft. Posterolateral view.

The resulting forces in the X-direction which resisted motion of the radius under a compressive load were measured from the stage at a rate of 100 data points per second, resulting in a spreadsheet output of Force (N) vs. Time (s) with approximately 700 data points. Differences between this number and the overall number of reported data points were due to periodic actions by the GSTIFF integrator solving the model under the user-prescribed default length of the initial time step (Section 3.7), resulting in the program decreasing the time step to enable solving.

Upon testing the intact, monopolar, and bipolar radial head states, the dependency of stability and these radial heads replacements with detached soft tissues was explored. The cadaveric study included a separation of the lateral collateral ligament complex, including the LUCL, all bands of the RCL, and its common extensor tendon from the humerus. In the computational study, the common extensor tendon was not included. The LUCL and RCL were effectively removed by suppression of their action-reaction forces, and the mono- and bipolar states were run once again. It was not possible to accurately represent the repaired state in this model despite its inclusion in the cadaveric study, as the ligaments were repaired directly to their insertions and no artificial method of pre-straining the ligaments was described by the authors.

4.4. Results

Force resisting motion in the direction of the displacement was measured throughout the breadth of the study and tabulated into spreadsheet form. A number of other quantities not observed in the cadaveric study were also measured, including forces within specific ligaments and capsular bands, as well as contact forces between bodies for further understanding of the behavior of the model. Universally across the radial head states there was a short period of great variations in magnitude over the initial time steps. This was caused by high-frequency oscillations within the model between 0-0.1 seconds which then dampened, leading to an equilibrated period after the 50N humeral loading. When radial posterior (+X) displacement began at t=2s, these forces ramped smoothly in the +X-direction and then reached another steady-state plateau after the full displacement at t=5s. Peak loading was seen consistently at the most extreme displacement before a slight decay, followed by another steady-state plateau for the final 5-7 seconds (Figure 4.4-1).

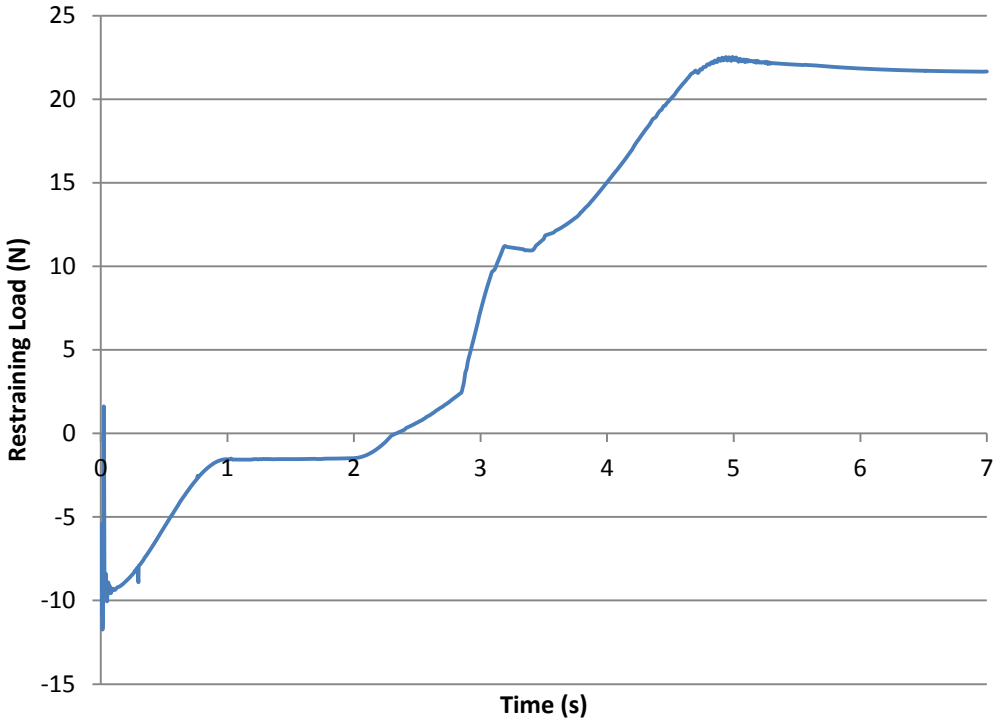

Figure 4.4-1: Intact RH run with displacement applied from 2-5s

Loading was measured at a point at the center of the stage during the breadth of the study, representing a sum of the loads in the direction of displacement experienced by the radius during subluxation. This included forces in the X-direction for all ligaments, capsular bands, and contacting surfaces. Positive X-forces were directed posteriorly. Results within Chanlalit et al. (2011) were reported as the average peak load during displacement with standard deviations based upon the twelve cadaveric specimens. Comparisons between the cadaveric and computational studies for both intact and resected lateral collateral ligaments (LCLx) with a single standard deviation indicated in error bars are shown in Figures 4.4-2 and 4.4-3. For further understanding of the model's behavior over time, forces resisting subluxation throughout the posterior displacement were tracked and are displayed graphically in Figures. 4.4-4 and 4.4-5.

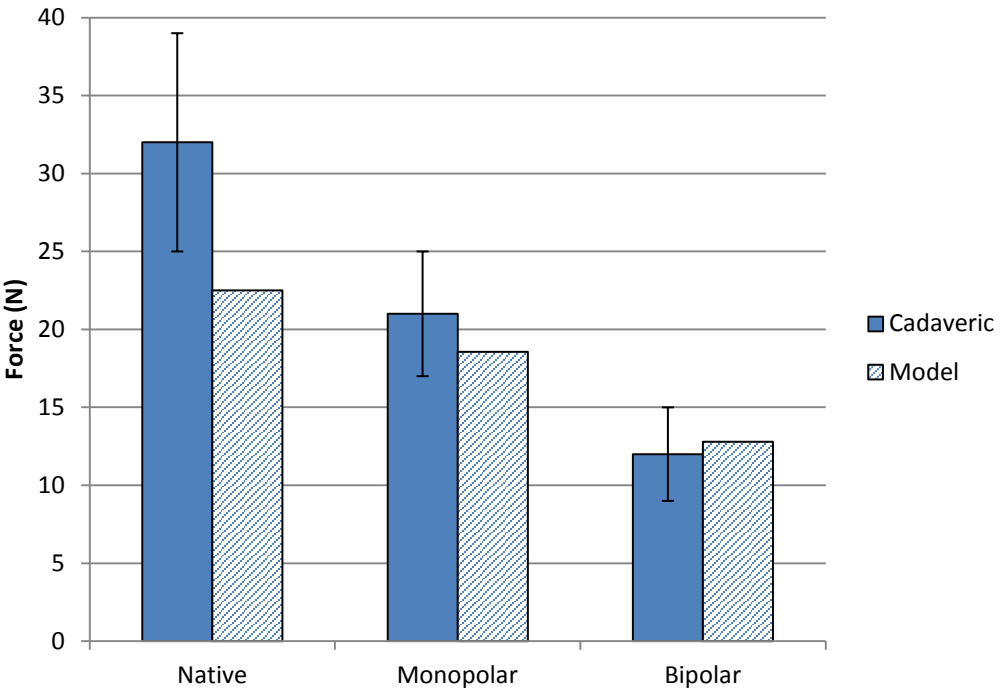

Figure 4.4-2: Peak resistive forces for intact, monopolar, and bipolar model compared to cadaveric data for intact ligaments

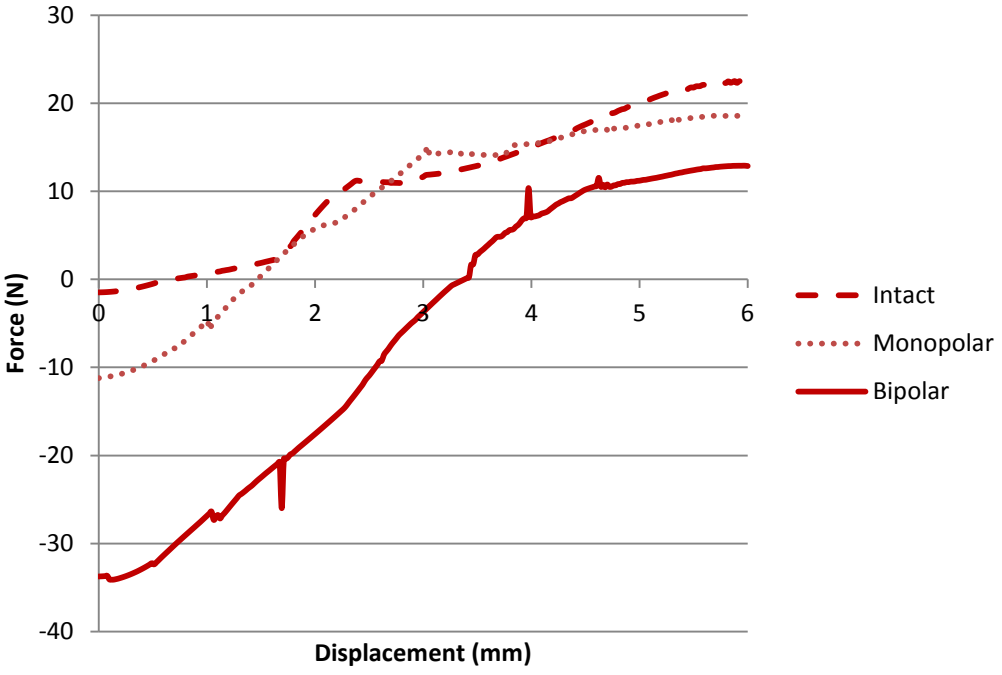

Figure 4.4-3: Forces resisting subluxation across displacement in model for all radial head states with intact ligaments

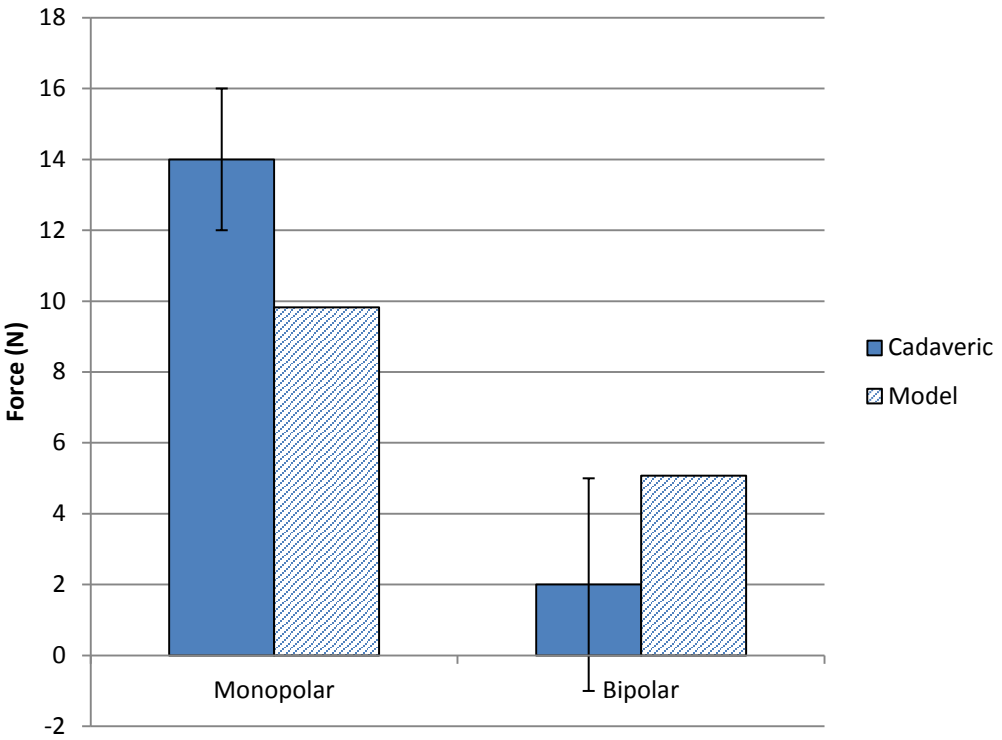

Figure 4.4-4: Peak resistive forces for intact, monopolar, and bipolar model compared to cadaveric data for LCLx (resected LUCL, RCLs)

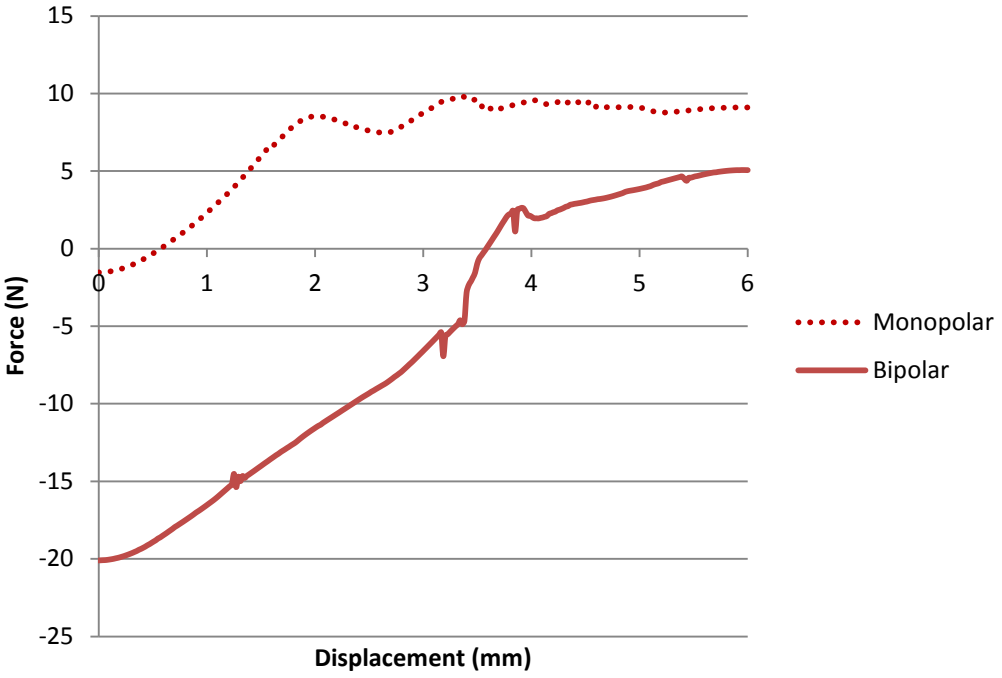

Figure 4.4-5: Forces resisting subluxation across displacement in model for all radial head states with LCLx (resected LUCL, RCLs)

The results of the computational model correlate well with those of the cadaveric study. The constraining forces decreased in the ligament-intact state from the native head to the monopolar, while the bipolar head provided the least resistance to subluxation. The monopolar and bipolar states fell within one standard deviation, as seen in Figure 4.4-2. The intact state reported forces lower than those in cadaveric testing with peak forces just outside of a single standard deviation. Chanlalit et al. demonstrated that the restraining load of the monopolar radial head is only 65.6% of the intact, while the bipolar results in a significant decrease from the intact at 37.5% of the total. The computational model experienced similar decreases. The monopolar radial head state was 82.5% as stable as the intact. Comparatively, only 56.9% of the subluxating force was seen in the bipolar state. Also in the cadaveric study, the bipolar radial head resulted in 42.8% less constraining force than the monopolar, while a 31.1% decrease was seen in the model. These similar results support the hypothesis that stability would decrease with implantation of a bipolar radial head.

Regardless of radial head state, each model began with overall magnitude of loading in the –X-direction, opposite the direction of displacement. The intact radial head began with loads near zero, indicating a stable environment with little natural pull by the ligaments and capsule toward distraction of the radius. The monopolar state experienced more negative loading at the start of displacement, indicating the capitellum interacted with the radial head on the posterior curvature of the concavity. These anteriorly-directed forces were aggrandized in the bipolar state with forces significantly higher in the negative X-direction.

When observing the less stable, excised ligament state for the mono- and bipolar radial heads, the data well reflects the behavior demonstrated in the cadaveric study. Results for the computational model were just outside of one standard deviation for the bipolar state, and within two standard

deviations in the monopolar, though the peak subluxating force in the monopolar state was lower than indicated in the experimental study. However, the trends of the data were very similar to those reported. Compared to when the lateral ligaments were intact, the monopolar head state experienced a 33.3% decrease in constraining forces with the experimental study, while a 47.1% decrease in the computational model. The bipolar head was significantly more dependent on the lateral ligaments than the monopolar. In the cadaveric study this less-stable state experienced an 83.3% decrease in stability from the bipolar state with ligaments intact. Likewise, a 60.4% decrease was indicated by the computational model. A larger decrease between the two states of ligaments intact and excised with the bipolar head shows an inherently greater dependence of this design on these lateral soft tissues as opposed to the monopolar. Though the numerical peaks in data were outside of one standard deviation for the LCLx portion of the study, trends in data and percent decreases reflect a computational model accurately predicting the results of a cadaveric experiment.

4.5. Discussion

Chanlalit et al. (2011) made efforts to show that the bipolar radial head system, used clinically as a replacement for resected radial heads, does not accurately restore stability of the elbow, while the monopolar more readily reflects native function. The cadaveric study also showed that the bipolar radial head replacement is more dependent on lateral tissues than the monopolar, indicating its unsuitability for elbow injuries involving ligament damage. The described rigid body model of the elbow accurately predicted the behavior of the cadaveric specimens throughout various radial head states and with lateral soft tissues intact and resected. It demonstrated that the bipolar head is the least stable of the replacement states, redirecting forces anteriorly in a severe manner and resulting in low resistance to posterior subluxation in comparison to the native head and monopolar replacement. The monopolar

head behaved similarly to the intact, though it more easily allowed extreme subluxation than the intact head. Also, the monopolar and bipolar testing resulted in peak loading within one standard deviation of the cadaveric data. The experimental model further demonstrated its efficacy in a more unstable state, observing the decreases in resistive forces in the mono- and bipolar replacements with lateral collateral ligaments excised. Furthermore, the model reflected a greater dependence of the bipolar radial head on lateral ligaments than the monopolar.

Though prior experimental studies have emphasized the coronoid process and lateral ligaments as the primary stabilizers of the elbow, it becomes clear that the radial head is an important character which requires further exploration. Upon the application of a posterior displacement, the native radial head affords significant stability; more than 20N of force were exhibited with the intact radial head and ligaments, resisting subluxation, and over 30N were shown in the cadaveric study. Though the computational intact state fell outside of a single standard deviation, a large standard deviation of 7N with a sample size of only twelve specimens affords a focus on data trends across the various radial head states as opposed to raw results. The monopolar and bipolar states further exemplify the radius as a key stabilizer and fell within a single standard deviation of the cadaveric data. Replacement of the radial head with a monopolar prosthetic, which is structurally symmetrical, has a shallow cup and is not reflective of the native anatomy, resulted in a decrease in resisting forces of approximately 4N, almost 20% of the intact. The elbow with a bipolar prosthetic experienced a significant decrease in forces resisting subluxation, falling 10N below the intact state. This decrease in stabilization by 40% clearly indicates that despite intact lateral ligaments, a destabilizing factor was demonstrated by only replacing the radial head, thus providing further evidence that the radial head is a key contributor to elbow joint contact forces and stability.

It was also evident that the bipolar state granted less stability than the monopolar. Its ability to tilt, designed with the intent of allowing for accidental incorrect alignment during implantation, in fact enables the direction of contact forces to shift in non-physiological ways. This is most evident in Figure 4.4-3, which graphically demonstrates a shift in forces in the anterior direction under zero loading as well as axial loading. While the native radial head experiences only slightly anterior forces, its loading is nearly centered over the proximal concavity. This inherent alignment begins the elbow in a stable position prior to the application of axial loading or displacement. The bipolar head experiences significant anterior loads approaching 35N, resulting in an unstable environment. During the posterior displacement, the bipolar head results in the largest shift in loads from anterior to posterior, and the bipolar head tilts downward anteriorly as the head pulls away from the capitellum. The tilt allows for an inappropriate freedom of motion that inherently flaws the design, as it does not accurately represent the functionality of the radial head and creates a state prone to subluxation. The radial head tilt also decreases overall radiocapitellar joint contact forces, further destabilizing of the elbow.

As was addressed in the cadaveric study, a coincidence between the resistive forces experienced with the intact and monopolar radial heads over the course of displacement occurred. Between 2-4mm of displacement, the X-direction output similar results and the graphs reflected like curves. The monopolar head, though more symmetrical than the intact, affords significantly more stability to the system than the bipolar. In the non-distracted state, the symmetrical concavity of the monopolar head forced greater anterior loads than the intact, possibly due to the shallower cup shape. However, low displacements resulted in the capitellum of the humerus interacting with the proximal, anterior slope of both the intact and monopolar heads in similar manners. As the heads interacted with the ball of the capitellum, loads increased in a posterior direction and resulted in results between 10-15N; however, at larger displacements greater than 5mm, the stability created in the intact state increased accordingly while the monopolar head leveled off in its contribution. This can be attributed to its symmetrical

shape. The intact head has a greater radius in the anteroposterior direction than the monopolar, and thus the capitellum interacts more closely with its geometry and the resistive loads increase.

The second portion of the experiment considered the reliance of the two prosthetic designs upon lateral soft tissues. It is considered a standard approach to repair lateral ligaments and leave radial heads resected or replaced in cases of injuries where both structures are severely damaged. This experiment demonstrated that in the absence of lateral soft tissues, the monopolar head still afforded stability to the joint that resisted displacement. Almost 10N of force resulted, a decrease by one-half of the ligament-intact state but a stabilizing force nonetheless. In contrast, the bipolar head granted little in the way of resistance to posterior motion. When compared to an elbow with intact ligaments and radial head, restraining loads decreased by almost 57% in the case of the monopolar head and 78% with the bipolar implant. In consideration of the forces over displacement, the bipolar head resulted in a state where loading remained opposite the intact and monopolar, directed in the anterior direction until more than half of the displacement was complete. Together, these resistive loads clearly indicate a greater dependence of the bipolar state on lateral soft structures than the monopolar. Though the behavior of the computational study accurately reflected the behavior of the cadaveric specimens, the results fell outside of a single standard deviation. It is necessary to mention the exclusion of the common extensor tendon in the model, which has not been the subject of studies to determine its mechanical properties. The high standard deviations, particularly in the case of the bipolar head, could also indicate inconsistencies in the cadaveric data which may be represented in the model.

Further investigation into the distribution of loads in all directions indicated that the greatest forces were exhibited in the X-direction. Forces in the Z-direction were generally consistent based upon the 50N axial load applied through the humerus, while the Y-direction experienced low forces. This

provides further support that the results in the X-direction are the greatest contributors to resistance against posterior subluxation.

Exploration of the loading across various ligaments throughout the computational study validated the behavior of the overall model. Those flexion-angle dependent ligaments which are yet inactive in an elbow under 30° of flexion, such as the LUCL, RCL-A, RCL-P, and posterior bands of the MCL experienced zero loading throughout the breadth of the displacement. The RCL-C and MCL-A, which are considered active in this position, exhibited appropriate loads. The peak load in the central RCL band was achieved in the intact state, with 11.3N of force in the positive X-direction. Loading decreased in the elbow with the monopolar replacement to 7.71N, but a more significant drop was discovered in that with the bipolar head. Only 5.15N, less than half of the force restraining subluxation in the intact elbow, was read in the RCL-C in the unstable bipolar head. At 30° of flexion, the RCL-C is the primary soft tissue stabilizer against varus motion, and though varus laxity was not considered in this experiment, it can be gleaned that at low flexion angles the bipolar radial head would provide less support than what is physiologically necessary to resist varus distraction.

The bands representing the annular ligament, which attached the ligamentous solid body around the head of the radius, are not flexion angle dependent and experienced loading throughout the breadth of the study. It was validated that the ulnar tether maintained less than 1N of loading throughout the displacement, and the capsular ligaments experienced less loading than the active ligaments. This is an expected outcome, as the explicit contribution of the capsule in kinematics is unknown, though it is known to afford some stability in low flexion angles and full extension. It can be assumed that the capsule experiences less loading than ligaments, as its structure is less specified to resist motion than ligamentous tissue.

Observing ligament loading also brought to light an increased load for the MCL-A when lateral soft tissues are resected compared to the intact state. A significant increase in forces was reported by the computational model for both radial head replacements. As the lateral tissues release, the stability of the annular ligament about the radial head is lessened alongside the pull of the LUCL, which is antagonistic to the MCL-A. This enables more freedom of movement for the largely unconstrained ulna, causing unnecessary strain on the MCL during posterior subluxation. Other than the redirection of forces from the RCL-C to the MCL, joint contact forces also redistributed across the joint. In the intact joint under an applied posterior displacement of the radius, ligament loading is the primary resistance. However, the radial head also interacts with the ulna during subluxation, creating almost 20N of force on the posterior ridge of the radial notch, resisting the displacement. With mono- or bipolar radial head displacements, this resisting contact decreases slightly in the monopolar case and by almost half in the bipolar. Resecting the lateral tissues aggrandized the issue, allowing more motion of the radius and thus allowing it to pass the radial notch without significant contact. Ulnohumeral joint contact forces also increased with the suppression of lateral tissues, which afforded freedom to the annular ligament and permitted the humerus and ulna to abut each other during the displacement and applied humeral loading. The ability to observe ligament tensions as well as joint contact forces which are difficult to measure experimentally is a key strength to computational modeling and allows an enriched understanding of the behavior of a joint under various stresses.

One limitation in this study is the exclusion of the extensor tendon, whose inclusion could affect the overall forces. This tendon originates on the lateral epicondyle and attaches the extensor muscles to the elbow before they insert on the radius and the dorsal side of the hand. Inclusion of this tendon could further stabilize the radius and resist its motion, increasing loads required to move the radius posterior. Also, further exploration of the representation of the capsule is necessary, as it has not yet been modeled in rigid body computational studies of the elbow. Its inclusion is necessary for evaluation

of all resistive forces, as its anterior attachments in the humerus, ulna, and annular ligament would work in concert to resist posterior motion.

5. RADIAL HEAD PROSTHETIC DESIGN IN THE TERRIBLE TRIAD INJURY

5.1. Overview

Further evidence of the efficacy of the 3D anatomically accurate computational model was demonstrated by replication of a more complex study concerning the terrible triad. “The biomechanical effect of prosthetic design on radiocapitellar stability in a terrible triad model” by Chanlalit et al. (2012) quantified the respective stabilizations of the elbow of various radial head prosthetics in a highly unstable injury [38]. The devastating but uncommon terrible triad injury commonly requires repair of lateral ligaments, fixation of the coronoid process, and finally replacement of the radial head. This study considered the most common prosthetics, mono- and bipolar non-anatomic, in comparison to the newly developed anatomic radial head prosthetic system (ARHS) in a joint in which ligament repair and coronoid fixation were implemented. Cadaver specimens were subjected to a coronoid process tip subtype 2 fracture and radial head replacement, as well as LCL incision and repair. Anterior and posterior subluxation was applied to the radius alongside axial compression upon the humerus. Chanlalit discovered that there was no statistical difference between the subluxating force of the native radial head and the anatomic radial head replacement, but there existed a definitive decrease in necessary force for the non-anatomic prosthetics. Of these, the monopolar design was more

representative of the force-displacement curve achieved by the intact state and the ARHS. This cadaveric study indicated that the newly-developed ARHS is the most reliable prosthetic at accurately representing the native radial head especially in states where elbow stability is compromised, but the monopolar replacement is also a consistently stabilizing option. The bipolar prosthetic is the least desirable of the three designs, given its tendency towards subluxation with tilt [38].

5.2. Experimental Method

Eight fresh-frozen cadaveric elbows with a mean age of 76 were used for the study, consisting of an even number of male and female specimens. The joint capsule and tendon origins around the elbow were left intact with complete removal of skin, muscle, and tendons. Near the humeral insertion site in the joint, a capsular incision removed all but the anterior bundle of the medial collateral ligament, which remained intact.

To mimic the ulnar portion of the terrible triad injury, a controlled tip subtype 2 fracture of the coronoid process was created involving less than 30% of the structure, as defined by an imaginary line extending from the anterior-most tip of the olecranon. The breakage was fixed by drilling a pilot hole and inserting a 2.7mm self-tapping cortical screw as a lag screw from posterior to anterior. The lateral collateral ligament complex was repaired using a single suture.

Two radial head replacement systems were utilized for efficacy comparison. The aforementioned Tornier SA Radial Head System, a non-anatomic bipolar prosthetic, was selected and a custom-designed metal cuff was implemented to the system to create monopolarity. The newer Anatomic Radial Head System (ARHS) (Acumed, Hillsboro, OR) was also selected for its novel design. Though monopolar in structure, the head of the ARHS is modified to better reflect the native geometry

of the radial head. It has an elliptical head shape, offset by 4° in both the anteroposterior and mediolateral planes. The proximal concavity for capitellar articulation is offset from the center of the head by 1mm with a varying radius of curvature, and reaches a depth of 2.0mm at its center. A variety of radial head and neck sizes are available commercially for the RHS and ARHS, and the appropriate size was selected for each specimen per manufacturer recommendations. The non-anatomic radial head was matched with the short axis of the native radial head, while the Acumed anatomic system matched with the long axis [38].

Specimens were fixed into a custom-made mechanical testing device as described in Section 4.2 [80]. Axial compression loads of 50N were applied to the humerus, while the radius was translated in a controlled fashion 6mm anteriorly from the starting position at a rate of 2mm/second, then returned to the starting position and tested in the posterior direction. Data was collected by a load cell attached to the radius at 45 Hz, measuring compressive force data between the radial head replacement and capitellum. Two cycles of the test were performed, though the second was utilized for data analysis. The experiment followed a particular sequence: the native radial head post-ligament repair (surgical control), post-radial head replacement (randomly selected between mono- or bipolar RHS), post-radial head replacement utilizing the RHS unused from the previous test, and post-ARHS replacement. Randomization between the non-anatomic mono- and bipolar radial head replacements eliminated variation of results possibly due to sequence [38].

5.3. Computational Method

5.3.1. Overview

The experimental setup was created within the SolidWorks design space as with the mono- and bipolar RHS cadaveric study (Chapter 4). The appropriate ligaments were activated, including the LUCL,

RCLs, anterior MCL and distal capsule bands; the anterior joint capsule and posterior MCLs were suppressed due to experimental protocol. The aforementioned humeral osteotomy was unnecessary as the surgical approach changed, instead using an incomplete circumferential excision of the capsule and displacement of the elbow to expose the radial neck. A repaired terrible triad injury was the focus of this study, so a shearing of the coronoid process was applied and the width of a standard oscillating bone saw blade was removed from the body of the coronoid before the tip was "repaired" back to the main body of the ulna. Ligament repair was designed based upon images and descriptions from the cadaveric experiment. The same Tornier bipolar radial head replacement with the monopolar option was utilized, as this particular study compared these two RHS conditions with the monopolar Acumed ARHS. Having an identical materials testing apparatus, this study required development of a model of the ARHS for testing. Axial loading was applied to the humerus while the radius displaced posterior, and the restraining loads in the X-direction were measured.

5.3.2. Radial Head Replacements

Three distinct types of radial head replacements were tested in this study. The previously modeled Tornier bipolar head as well as its monopolar variation were utilized as an example of a non-anatomic radial head design. Its perfectly circular footprint and symmetrical concavity upon its proximal surface do not accurately represent the geometry of the native radial head. In contrast, the Acumed ARHS was designed such that it more truthfully reflected the structure of the intact head, and thus it was chosen as a comparison to the non-anatomic system.

The Acumed anatomic radial head system was designed to better restore the elbow post-injury through improving stability, kinematics and radiocapitellar contact forces. This was achieved through closer consideration to anthropometric and cadaveric data to accurately design more advanced

instrumentation than what was previously available. Its monopolar structure reflects the bony structure of the radial head and neck. A greater variety of head and neck combinations exist for the ARHS than with the Tornier RHS. The head is 10mm in height as opposed to 12mm in the Tornier, and its elliptical shape contrasts with the circular one of the older design. The radial head replacement is measured and implanted using the long radius, or widest measurement of the native radial head, and comes in a range of sizes increasing in 2mm increments from 20 to 28mm. The head chosen for the model was 22mm along the long diameter, reflecting the 22.04mm measurement of the intact head. The short diameter of the implant, therefore, was 20.6mm per manufacturer's dimensions (Figure 5.3-1). Given that the structure of the stem was inconsequential, as the radial head in the computational model was fixed relative to the radius, the same stem was used for the Tornier system was implemented in the study as opposed to designing a new stem for the Acumed ARHS.

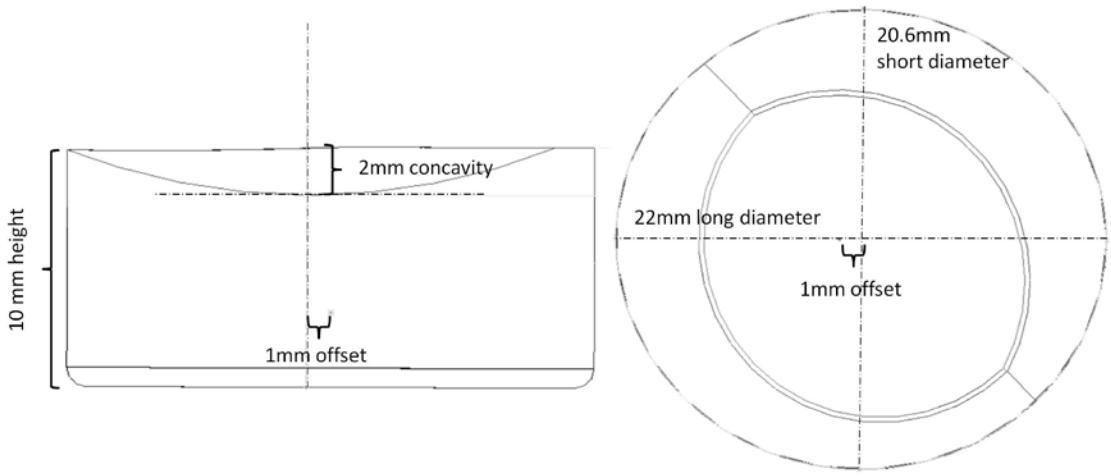

Figure 5.3-1: Dimensions and structure of the Anatomic Radial Head System, pre-4° angulation of proximal surface (L) and after (R)

According to the manufacturer's description, the depth of the concavity on the proximal surface of the radial head replacement was 2.0mm, despite synopsis of the head's structure in the cadaveric study which described it as 2.3mm. Thus, an overall depth of 2.0mm was implemented in the design, and it

was offset by 1mm anterior from the center. The articulating surface of the head was also canted in two planes by 4°, the mediolateral and anteroposterior (Figures 5.3-2, 5.3-3).

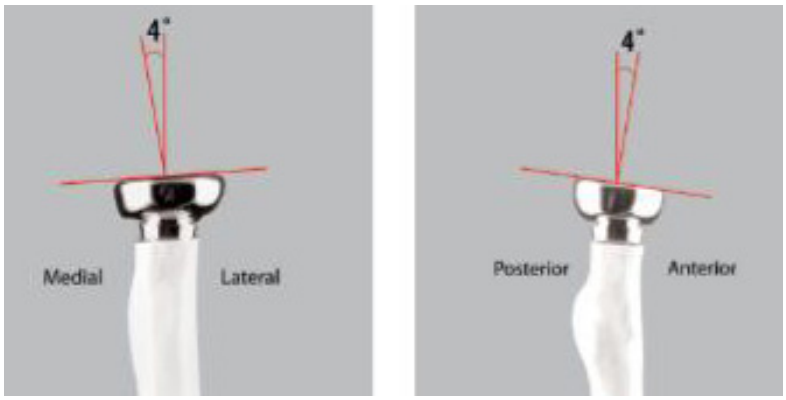

Figure 5.3-2: Acumed visual of the ARHS implanted upon a sawbone, canted surface shown (Acumed)

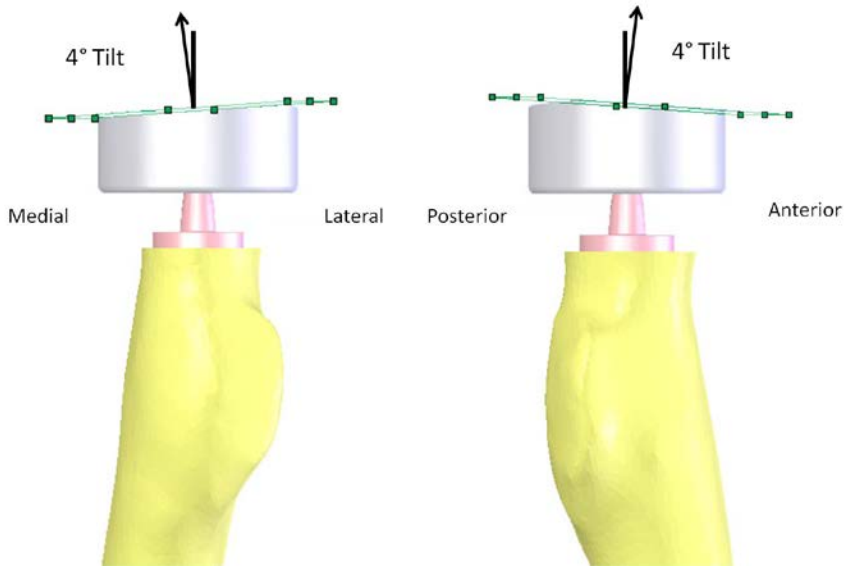

Figure 5.3-3: Modeled ARHS with tilt recreated using cut planes, shown

Given the precise geometry of the ARHS and its representation of native articular structures it was necessary to define a precise method of placing the prosthetic on the radial neck. The same radial neck cut plane was utilized as in the previous cadaveric study at 17mm from the most proximal point of the radial head (Chapter 4), and the implant attached at a position 5mm proximal to the radial neck cut.

This resulted in a 2mm understuffing of the joint, given the 10mm height of the structure. Though seeming contrary to clinical methodology for implantation, this was considered an appropriate measure given the imprecise description of the ARHS' placement on the stem in the cadaveric study. Little research has been afforded to the correct positioning of radial head replacements such that there is maintenance of the native height. It is known that in fitting radial head stem replacements to the widest diameter of the radial neck, considered a standard practice, the resulting stem and head combination have an average gap of 4mm between the radial head implant and the capitellum. A range of 1-7mm of shortening has been recorded [36]. Other researchers have demonstrated that shortening or lengthening of greater than 2.5mm can have detrimental effects on the overall kinematics of the elbow joint [28]. It is a reasonable assumption therefore, based upon the description supplied in the cadaveric study, that the radiocapitellar joint could be understuffed to an extent. However, in an effort to prevent this standard understuffing from affecting the overall joint stability, an understuffing of 2mm was deemed appropriate.

On the radius, the mediolateral and anteroposterior planes were created based upon the International Society of Biomechanics' suggestions, using the relative positions of the ulnar and radial styloids to determine the positioning planes of the radius [65]. Planes were then created based upon these that were offset by 4° in the appropriate directions, distally canted both medially and anteriorly. To position the prosthetic appropriately, the cut planes for the proximal surface of the ARHS were mated parallel to these, and the implant was locked through mates relative to the radius in this location. This ensured correct placement of the radial head system such that it represented fully the native geometry throughout the duration of the computational study.

5.3.3. Computational Implementation of Experimental Setup

The cadaveric study utilized a different approach for replacing the radial head than in the previous study (Chapter 4), therefore modeling of a lateral humeral condylar osteotomy was unnecessary. The humerus remained intact within the SolidWorks design space. However, the described surgical approach required an incomplete circumferential excision of the capsule and displacement of the elbow, exposing the radial neck. This rendered the previously described anterior capsule unwarranted and therefore it was removed from the study. The annular ligament remained intact for this study, and thus the distal bands of the capsule also remained intact and were modeled in the same fashion as in the prior computational model.

Instead of the humeral osteotomy, to mimic the terrible triad injury, the tip of the ulnar coronoid process was cut to mimic a tip subtype 2 fracture, indicating a break of more than 2mm of bone but involving less than 30% of the coronoid, a typical injury of the terrible triad [9]. This fracture was performed via a controlled transverse osteotomy and fixed to the body of the ulna using a 2.7mm self-tapping cortical screw inserted from posterior to anterior. In the computational study, this repair had to be modeled for accurate representation of the results, and 25% of the coronoid height was determined an appropriate representation of the fracture. As described by Morrey, 25% of the coronoid height was defined by a line demarcating the deepest margin of the sigmoid notch, as well as another perpendicular to this line extending to the most anterior tip of the coronoid process [9]. This was determined as the total height. A plane fitted to these two lines was created, representing the central ridge of the trochlear notch, and the cut plane for the osteotomy was designated as normal to this trochlear notch plane. Using these features, a cut at 25% of this height was implemented. This fragment was shortened by the width of the average saw blade, 1.2mm, and reattached to the ulna to represent the fixing of the tip injury (Figure 5.3-4). This state was indicated as CP-r, or coronoid process repaired.

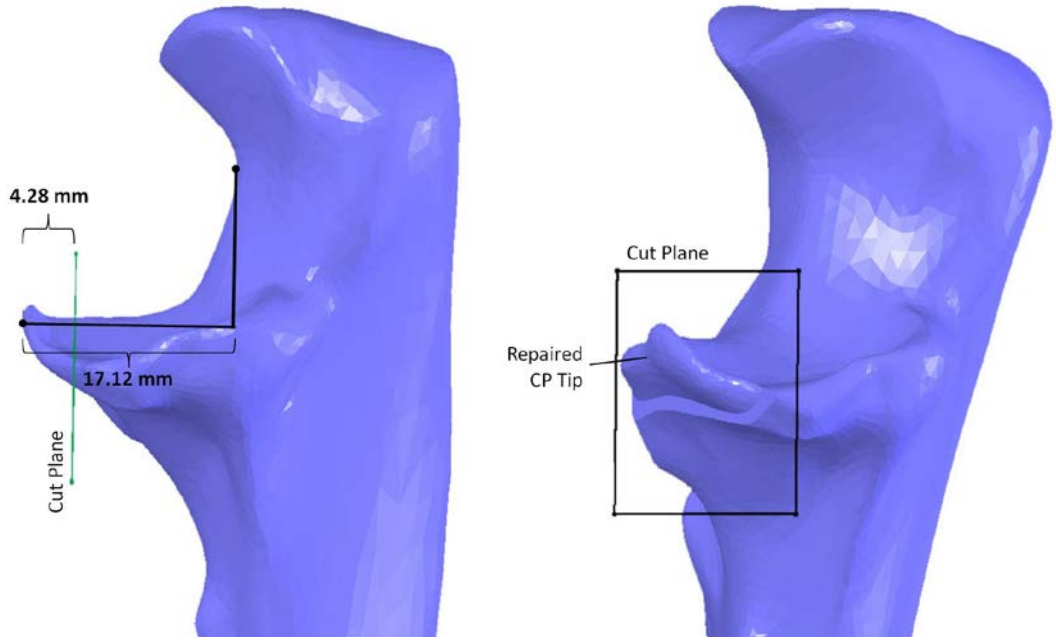

Figure 5.3-4: Proximal ulna and CP resection. Total height with 25% of height of CP indicated with cut plane in medial view (L). Repaired CP shown with cut plane and 1.2mm of bone removed, anteromedial view (R).

Within this study, the lateral collateral ligament complex was also detached and repaired, and results were taken for the repaired state. The repair method was described in the cadaveric study as a suture anchor with a 2.0 FiberWire suture implemented to reattach the dissected ligaments to their isometric origin. However, images within the published study indicate reattachment not to the lateral epicondyle per anatomic texts, but instead to a position on the lateral surface of the capitellum approximately at the center of the feature (Figure 5.3-5) [38].

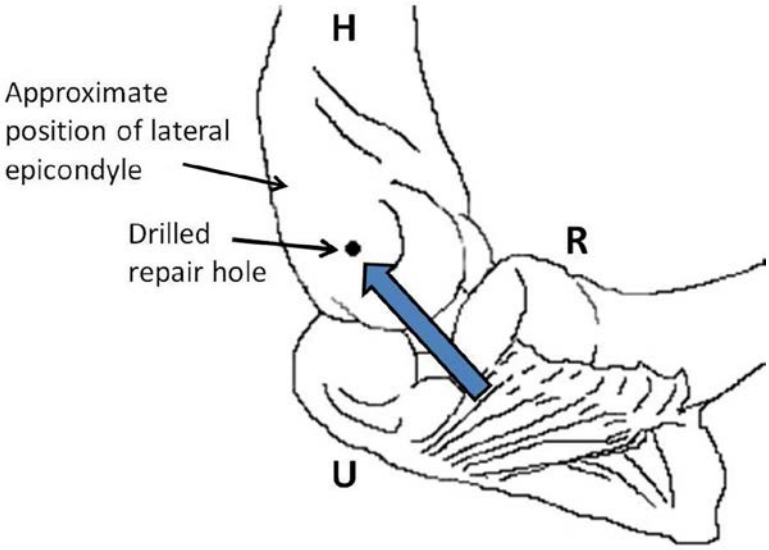

Figure 5.3-5: Rendering of the experimental reattachment of the lateral ligament complex to a location on the lateral surface of the capitellum. The repair site and origin are labeled. A blue arrow shows the soft tissue and its direction of reattachment (Chanlalit 2012)

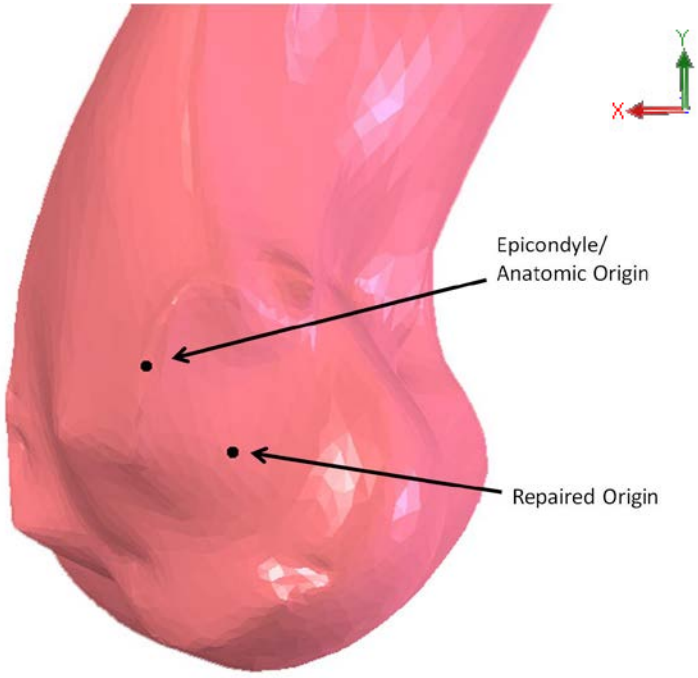

Figure 5.3-6: Modeled humerus, distolateral view, with marked unrepaired (anatomic) and repaired origins

This positioning of the lateral ligaments necessitated modeling of the repair in the computational experiment, described as LCL-r. The repaired origin was defined as the point on the lateral surface of the capitellum which pierced the axis of rotation (Figure 5.3-6). Given the change in position of the origin, new lengths and stiffnesses had to be determined for each lateral ligament to represent the repair while maintaining their properties. This was done by taking the equation for calculating stiffness presented in Equation 1 (Section 3.4.3), and modifying it to isolate the cross-sectional area and modulus of elasticity:

$$AE = kL \quad \text{Eq. 5}$$

Assuming that the modulus of elasticity and cross-sectional area of the repaired (r) ligament do not change from the intact form, this equation becomes:

$$k_1 L_1 = AE = k_2 L_2 \quad \text{Eq. 6}$$

$$k_1 L_1 = k_2 L_2 \quad \text{Eq. 7}$$

Using this final form of the stiffness equation, the repaired lengths were measured within the SolidWorks design space and stiffness calculated accordingly. The resulting values are listed in Table 5.3-1.

Ligament	Abbr.	Intact Length (mm)	Repaired Length (mm)	Intact Stiffness (N/mm)	Repaired Stiffness (N/mm)
Lateral Ulnar Collateral	LUCL	36.36	33.52	57.0	61.8286
Radial Collateral, Anterior	RCL-A	25.07	18.24	15.5	21.3061
Radial Collateral, Central	RCL-C	17.92	17.63	15.5	15.7553
Radial Collateral, Posterior	RCL-P	27.58	24.23	15.5	17.6446

Table 5.3-1: Material and Mechanical Properties of Repaired LCLs

The same materials testing apparatus was implemented, with a stage and platform to define and restrict motion of the radius to the X- direction as it was displaced 6mm posteriorly. The humerus

underwent 50N of axial loading, applied in the –Z-direction. Results were read as total forces in the X-direction and output to a spreadsheet with the same output parameters as described in the mono- vs. bipolar Chanlalit study (Chapter 4).

5.4. Results

As with Chanlalit et al. (2011), the subluxating force in the same direction as the applied radial distraction was tabulated throughout the study. Forces were slightly higher for the intact, monopolar, and bipolar states than in the previous study despite the lateral ligament repair and coronoid process repair.

Results for the constraining force within the cadaveric study were reported as the average peak load during displacement with standard deviations based upon eight separate specimens. A comparison between the experimental and computational studies for all four radial head states is graphically represented in Figure 5.4-1. A single standard deviation is represented for each experimental peak. Another chart showing the development of resistive forces over the course of the applied displacement for each state can be seen in Figure 5.4-2.

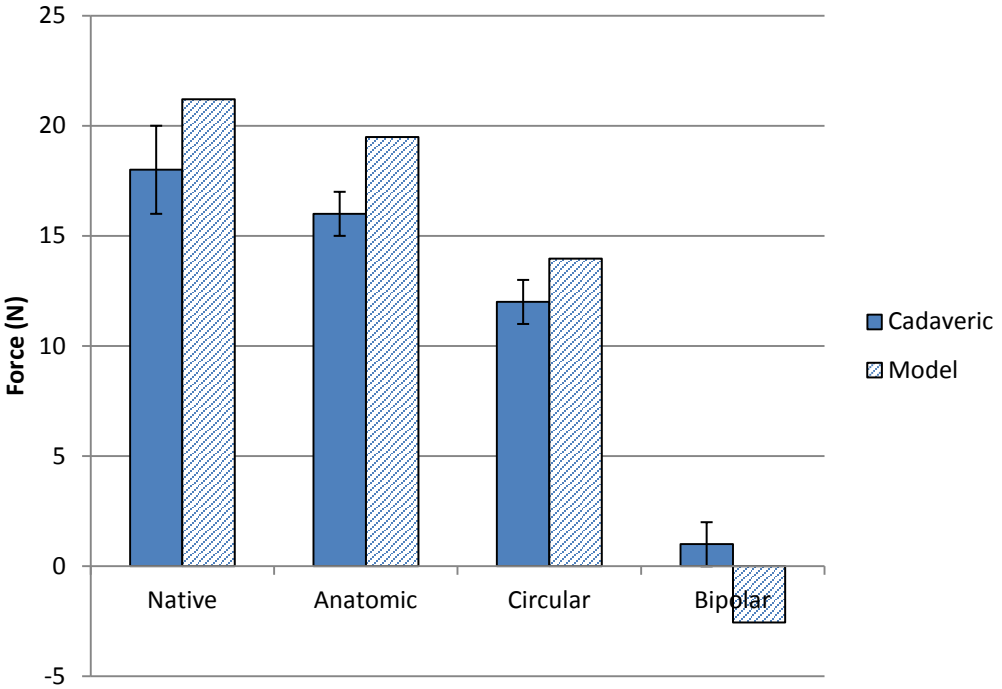

Figure 5.4-1: Comparison of peak resistive forces for intact radial head, anatomic, monopolar and bipolar replacements with LCL-r/CP-r in cadaveric study and computational model

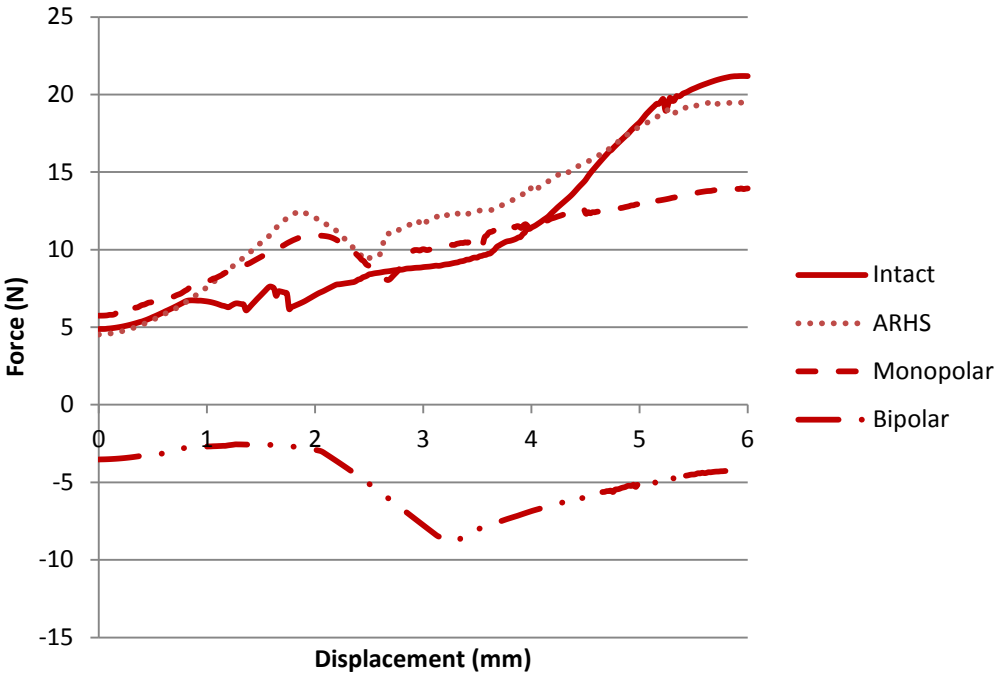

Figure 5.4-2: Forces resisting subluxation across displacement for all radial head states, with LCL-r/CP-r with replaced heads

The downward trend of the peak resistive forces across the various radial head states is evident in Figure 5.4-1, as is its similarity to the trend in the cadaveric data. Though the computational data exists outside of a single standard deviation for all cases, percent changes are more reflective of the behavior of the model and indicate its accurate representation of the experiment. Compared to the native, intact radial head, the percent decreases on constraining load are almost identical between the experimental and model results. In the cadaveric specimens, on average the peak subluxating force of the anatomic radial head system was 88.9% of the intact, while the computational study resulted in 91.9% of intact. The circular monopolar radial head exhibited nearly identical behavior between the experimental and model, resulting in decreases in load from intact of 66.7% and 65.8% respectively. Furthermore, the bipolar radial head system showed significant changes in loading in both cases. Experimentally, the study indicated that the bipolar RHS resulted in a decrease of 94.4% in the constraining load. Similarly, the model predicted a decrease of 112.1%, reflecting a change in direction of the load from the direction of displacement, instead toward the anterior, or –X-direction. Therefore, the model effectively predicted the changes in elbow stability across several different radial head replacements and demonstrated the dangerous instability created by the bipolar system.

Ligamentous loads were observed within the computational model, though not considered in the experimental study. They indicated that ligaments behaved appropriately based upon their activity at 30° of flexion, and resulted in similar physiological forces as described in Chapter 4. This occurred despite the repair of the lateral ligaments, indicating that their repair was appropriately modeled and ligaments maintained their contributions to stability. The ulnar tether was also affirmed to exhibit less than 1N of loading throughout the course of the displacement. The joint capsule was not considered, as it was considered ruptured in the semi-circumferential excision of the capsule.

5.5. Discussion

Exploration of the forces resisting posterior subluxation with four different radial head states in an elbow afflicted with the terrible triad brought to light the strengths and weaknesses of various radial head replacements. The terrible triad is a complex injury that is so named because of its inherent disruption of two key stabilizing elements: the coronoid process of the ulna and the lateral soft tissues. It also results in a fracturing of the radial head, forcing either its resection or replacement. This particular study sought not only to emphasize the importance of the radial head in this unstable state, but also to show that the replacement that most accurately restores stability is the anatomic radial head system. The ARHS is designed to best model the native geometry of the radial head, including its uneven radius of curvature, off-center proximal concavity, and the non-symmetrical footprint. The study demonstrated the benefits of the ARHS, showing the similarity between its peak restraining loads as well as its overall trend of force over displacement compared to the intact radial head. It also showed that another respectable replacement was the monopolar non-anatomic radial head prosthetic, though it afforded less stability at high displacements. The replacement with the least function in resisting subluxation was the bipolar head, which relied heavily on other stabilizing structures and allowed motion with very little prevention.

Peak subluxating forces of these four states follow closely with those presented in the cadaveric research. Forces were slightly higher for the intact, monopolar, and bipolar states than in the previous study despite the lateral ligament repair and coronoid process repair due to the lack of a humeral osteotomy, allowing more complete and natural contact between the capitellum and the concavity on the proximal surface of the radial head. Repositioning the capitellum by 1.2mm medial under application of the humeral osteotomy in the previous study caused the humeral articulating surface to contact more of the medial rim of the radial head, as opposed to the depths of the indention, thus decreasing loads in the X-direction slightly. In the terrible triad study, restoration of the humerus and

the position of the capitellum granted better contact between the humerus and radius throughout the computational run.

Compared to the native radial head, the anatomic radial head system only differs by fewer than 2N, while the peak force of the circular head fell to 13.9N, more than 7N lower than the intact. The bipolar, in contrast, peaked with forces directed in the opposite direction, at 2.557N in the anterior. These results reflect the close relationship between the model and cadaveric data, which showed no significant difference between the intact and anatomic replacement, but a statistical difference between the intact and monopolar. The cadaveric study also indicated that the bipolar state experienced a dramatic decrease in resistive forces. Similar differentials are demonstrated in Figure 5.4-1.

Following the trends of forces over displacement for each type of radial head, several details become evident. First, the intact, anatomic and monopolar heads undergo similar forces in the X-direction under solely axial loading. The capitellum interacts with each head such that they are under slight posterior loads, indicating its position slightly posterior in the proximal concavity on each radial head. These forces also increase at similar rates for the three testing states until reaching extremes in displacement. After approximately 4mm of posterior displacement, the rate of rise in forces for the monopolar radial head decreases and approaches a plateau. Its symmetrical shape and smaller overall diameter provide less resistance to posterior motion than the other radial heads. The capitellum instead rides up the slope of the proximal and anterior edge of the hardware, interacting more with the upper edge of the concavity as opposed to the cup shape which helps prevent posterior subluxation. In comparison, the ARHS and intact state follow similar trends until approximately 5mm of displacement where they diverge slightly, resulting in a slightly lower peak for the anatomic system. The anatomic radial head, more closely reflecting the native geometry, interacts with the capitellum for greater displacements than the monopolar because of its oblong shape in the anteroposterior direction. Its 4°

of angulation in two planes also affords more interaction with the lateral edge and on the posterior side of the capitellum, even amidst the posterior motion.

The bipolar head, the least representative of the intact state, exhibits opposite behavior and does not assist in stabilizing the elbow in the presence of a subluxating force. The forces measured during the displacement were directed opposite to those in the intact state, in the anterior direction. Under pure axial loading, the bipolar head is allowed to tilt slightly lateral and anterior, resulting in anteriorly-directed forces. Upon application of the displacement, the resistive forces rise slightly, shifting toward the posterior direction as the radius moves posterior and the capitellum begins to interact with the anterior edge of the head. However, after 2mm of displacement, the head tilts further downward anteriorly, approaching the fully allowed 10° of tilt, and primarily interacts with the capitellum posteriorly, resulting in an increase in anterior, negative loads. After full tilt of the radial head, the humerus moves downward to maintain 50N of load, resulting in a slight rise in forces toward the posterior direction as the capitellum interacts with some of triangular faces on the body which oppose motion. However, this gradual rise never results in overall magnitudes that resist posterior subluxation. This highlights a fundamental flaw in the design of the bipolar head. The ability to tilt redirects radiocapitellar forces opposite of their natural inclination, thus causing an inherently more unstable environment.

The model differed from the cadaveric data in that the results fell outside of a single standard deviation in all cases, while the anatomic and bipolar states were outside of two standard deviations. The native, anatomic, and circular radial heads resulted in higher peak forces than the cadaveric study, which could be due to the fact that the full viscoelastic behavior of the ligaments was not represented in the model. The use of a solid body to represent the annular ligament is not entirely representative of the natural soft tissue, though it does provide a method by which the ligament can “wrap” around the

head of the radius. The interaction between the radial head and the solid body of the annular ligament could also increase forces. The bipolar radial head exhibited loads in the opposite direction than those described by the raw data of the cadaveric study, though their standard deviation compared to the peak force reported calls to question their sample size of eight, and also indicates that there could be a greater variability in the data with further testing. Another figure presented in their study, represented as a line graph, indicates that the bipolar head followed a similar trend as that in the model, never reaching positive loads [38]. Despite the raw data, the aforementioned percent differences in the results are highly similar between the cadaveric study and the model. This indicates that though the numerical peaks were outside of a standard deviation, the model under the experimental design behaves appropriately, and radiocapitellar stability is affected by each radial head state in almost identical ways between the two sets of data. It accurately represents the behavior of the cadaveric study, and was able to predict effectively the behavior of the elbow under axial loading and posterior displacement in the complex terrible triad injury.

Soft tissue loads and articular contact forces were collected during the simulation for further understanding of the behavior of the repaired lateral ligaments and to consider the redistribution of forces across the various radial head states. Measured ligament loading remained similar between the intact and post-repaired states for most of the repaired ligaments, despite the repaired coronoid and suppression of the anterior capsule bands and posterior MCL. This indicated that the repaired ligaments were appropriately modeled and maintained their typical contributions to stability. However, though soft tissue forces remained comparable, peak forces during subluxation between the intact state and the repaired state of the intact radial head resulted in doubled contact forces between the RH and annular ligament solid body. With the affected anterior capsule, higher forces were also measured in the anterior MCL and the anterior distal band of the annular ligament, presumably as it resisted motion while the radial head subluxed. Forces were also measured in the repaired posterior RCL, which at 30°

of flexion should not be active. This could have been due in part to the manner in which the repaired ligaments were described in the study and therefore replicated; it may also be reflective of the RCL-P trying to compensate for the lack of soft tissues elsewhere in the presence of a displacement.

Also of note were similarities between the forces measured for the intact and anatomic radial head. Joint contact forces were comparable between the native radial head and the novel anatomic replacement, as were soft tissue tensions. Based upon the like distributions of forces in a compromised elbow for these two head states, the anatomic radial head seems to be a promising replacement for a patient with complex instabilities. In contrast, ligamentous restraining forces and solid body contact forces decreased for the monopolar radial head and especially the bipolar. Trends within individual ligaments over time were more similar between the monopolar and anatomic, though peaks were shorter. Meanwhile, restraining forces were extremely low in the bipolar head, resulting in little resistance to the subluxation.

The data gleaned from the model indicate clearly that replacement of the radial head with the anatomic radial head system is the most accurate manner by which radiocapitellar stability may be afforded to the joint, while the monopolar is another appropriate though less ideal option and the bipolar replacement should not be considered in the case where stability is an important outcome.

Aside from the solid body representation of the annular ligament, one limitation of this study could be the representation of the repaired lateral ligaments. The description of this repair in the cadaveric study was vague, and though it was modeled as closely as possible, there were still questions as to the exact location in which they were affixed and how they were pre-strained, if at all. Investigation into this method could result in a more accurate model. Another limitation is the exclusion of cartilaginous tissue on the articular surfaces, which provide damping upon bony contact, and the smoother surfaces decrease friction. Finally, expanding upon the method of modeling the ligaments to

include more viscoelastic properties would be ideal, and given greater computing power and new technologies, this may one day not increase run times towards being prohibitive.

It is also of note that, comparing the previously described mono- versus bipolar radial head study and the terrible triad study, the intact state for each resulted in similar peak resisting loads in the model. In contrast, the cadaveric model experienced a significant drop in the intact peak load with the application and repair of the terrible triad injury and release of the anterior capsule. This fact calls to question the robustness of the method by which the anterior capsule was modeled, and could indicate that the assumptions made to derive its mechanical properties underestimated the modulus of the capsule. It also draws attention to the repair of the lateral ligaments in the terrible triad cadaveric study compared to the model. The method of repair utilized in the model restored the function of the ligaments by modifying their stiffnesses to accommodate their changes in length with a relocated common origin. However, the repair in the cadaveric specimens may have affected the mechanical properties of these ligaments. Accordingly, this would also cause a decrease in peak intact loads in the cadaver study while not affecting the results of the model. A sensitivity analysis and uncertainty analysis of the model would be beneficial in determining the strength of these assumptions and could assist in the development of a final set of mechanical properties for the joint capsule and the repaired ligaments. Using a one-factor-at-a-time (OFAT) approach with these two features would be ideal to determine the modifications necessary to optimize the model for those uncertain inputs.

6. CONCLUSION

Expanding upon previous rigid body models of the elbow [15,17], a model was created to redirect emphasis on elbow research to the under-represented radial head. This model involved accurately represented 3D articular surfaces, while kinematics were determined by ligamentous constraints, articular contact forces and applied loadings. A dearth of research regarding the radial head, a key stabilizer, has resulted in an array of radial head replacements which do not all accurately recreate radiocapitellar stability, and until recently an prosthetic which tried to accurately represent native geometries did not exist. Different radial head prosthetic designs were explored by replication of two cadaveric studies, one considering the effects of mono- and bipolar circular radial head designs on elbow stability and their dependence on soft tissue integrity, the other observing these same heads as well as an anatomic design in an elbow under the effects of the terrible triad injury [37,38]. Accurate representations of the 3D anatomy were created using MIMICS, a software program designed to convert through careful selection 3D bodies out of computed topography scans. Using Hounsfield units to filter out soft tissue, bony material was selected and processed into triangulated surfaces, which were remeshed and processed into files of appropriate size which maintained the structures of the articular surfaces. Once bodies were created for the humerus, radius, and ulna, these were imported into the

commercially available CAD program SolidWorks, wherein a rigid body model was created. Within the SolidWorks design space, the solid bodies were manipulated to represent the cadaveric studies.

Representations of the experimental materials testing devices were created as well as two distinct radial head implants. The Tornier circular non-anatomic head was designed, which could be converted from mono- to bipolar, and another was built which represented the Acumed anatomic radial head system. Ligaments were represented in the model using insertions, origins, and action-reaction forces which utilized velocity-based damping and in situ strain to govern natural motion of the bones relative to one another. A joint capsule was added which expanded upon previously built models, affording more stability and physiologic behavior to the model than before. Motion was simulated and analyzed through the COSMOSMotion add-in. Thus, a computational model was developed which relied upon osseous structures, ligamentous constraints, and external perturbations to effectively predict the outcomes of cadaveric studies regarding applications of the radial head.

Validation of this model first involved replication of a cadaveric study observing the effects of a mono- and bipolar radial head replacement compared to the native head in both an intact state and with lateral ligaments compromised [37]. A second study simulated involved the terrible triad injury and incorporated a third radial head state using a modern anatomic radial head system [38]. For each study, the model was modified in the design space to reflect the respective experimental designs and the forces resisting subluxation, largely dependent on the radiocapitellar joint contact force, were evaluated. The model accurately represented the outcomes of each experiment, clearly resulting in the same trends as those exhibited in the cadaveric studies. Resistive forces were exhibited which indicated a distinct similarity between the anatomic implant and native radial head. It was also demonstrated that the monopolar radial head, though not fully restoring stability, adequately repaired the elbow without heavy reliance on lateral soft tissues. The model indicated that the bipolar radial head

replacement not only relied upon lateral ligaments, but also afforded a non-physiologic amount of freedom and little resistance to posterior distraction.

Not only did the model show the importance of radial head research when considering elbow stability but it also expanded on previous work through the incorporation of a joint capsule, which had previously been excluded. Few publications broach the subject of the mechanical properties of the joint capsule, despite its contribution to stability for elbows in low flexion angles or extension. Though assumptions were made regarding its properties and structure, these were necessary with the lack of data which currently exists. However, the designed joint capsule granted more resistance to motion and further strengthened the various applications of this computational model. The added stability improved the overall function of the model by more closely representing the native elbow joint.

Despite the validity of the model, several assumptions were made which could possibly affect outcomes and can be expanded upon. A primary assumption in this method of modeling involves representing bones as rigid bodies, which does not reflect the deformations which occur in the presence of articular cartilage. The deformation of cartilage, which covers articulating surfaces of the humerus, radius, and ulna, could modify the output maximum loading through dampening contact forces. Consideration of incorporating finite element analysis or deformable bodies would remedy this concern, though the time in which it would take to run the model could be prohibitive.

Another consideration is the modeling of ligaments as action-reaction force vectors, dependent on only the change in length to determine applied force. This method does not take into consideration the viscoelastic properties inherent to ligaments. The addition of a velocity-dependent damping helps to more effectively represent native ligamentous properties, though it does not represent viscoelastic function. One key component to representation of ligaments would be further research into the specific mechanical properties of each. Many ligaments of the elbow have not been fully researched regarding

these properties due to difficulties in testing small structures. More accurate information could lead to better governing statements for modeling of ligamentous tissue.

One other concern is the physiologic wrapping of ligaments about bony surfaces. Representing these ligaments as solid bodies, or by creating secondary insertions to reflect lines of action are not the most effective methods of modeling. The ideal would be the application of a deformable semi-rigid body over rigid surfaces, which attached on one structure, inserted on another, and maintained its own mechanical properties. However, this technology is not within the modeling package available, though its inclusion would be an exciting addition to the computational model.

An effort was made in this thesis to develop a rigid body model of the elbow which accurately predicted the outcomes of two cadaveric studies in an effort to highlight the contributions of the radial head to elbow stability. This model was able to represent an intact, ligament deficient, and injured elbow effectively and explore the effects of three different radial head replacements: a monopolar circular implant, a bipolar circular implant, and an anatomic system. It not only output the forces resisting subluxation, but it was also able to output myriad other types of data not easily gleaned experimentally, such as ligament tension. Further use of this particular model could be in the study of the effects of the radial head on elbow kinematics, a topic of interest which is under-researched in current publications. However, at a much lower cost than cadaveric studies, requiring fewer resources and utilizing commercially available software, this computational model was able to predict cadaveric results. The benefit of a customizable model which could be modified to reflect any cadaveric study enables the researcher to explore in-depth factors not easily tested experimentally, and without the usage of valuable cadaveric specimens. Computational modeling could be a key to not only furthering understanding of joint kinematics or other academic functions but also in a clinical setting, including the development of novel surgical approaches, the investigation of joint repair techniques, fixation devices,

and implants, and even patient-specific implant design or pre-operative decisions. Rigid body modeling, therefore, has great implications as a tool for a wide array of joint research and promise as a predictive tool in clinical settings.

REFERENCES

[1] Bhavikatti S. S., 2005, Finite Element Analysis, New Age International Publishers, New Delhi.

[2] Bendjaballah M. Z., Shirazi-Adl A., and Zukor D. J., 1997, "Finite element analysis of human knee joint in varus-valgus," Clinical Biomechanics, 12(3), pp. 139–148.

[3] Giddings V. L., Beaupre G. S., Whalen R. T., and Carter D. R., 2000, "Calcaneal loading during walking and running.," Medicine & Science in Sports & Exercise, 32, pp. 627–634.

[4] Herren D. B., Ploeg H., Hertig D., and Klabunde R., 2004, "Modeling and Finite Element Analysis of a New Revision Implant for the Elbow," Clinical Orthopaedics, (420), pp. 292–297.

[5] Koolstra J. H., and van Eijden T. M. G. J., 2005, "Combined finite-element and rigid-body analysis of human jaw joint dynamics," Journal of Biomechanics, 38(12), pp. 2431–2439.

[6] Moazen M., Jones A. C., Leonidou A., Jin Z., Wilcox R. K., and Tsiridis E., 2012, "Rigid versus flexible plate fixation for periprosthetic femoral fracture—Computer modelling of a clinical case," Medical Engineering & Physics, 34(8), pp. 1041–1048.

[7] Erdemir A., Guess T. M., Halloran J., Tadepalli S. C., and Morrison T. M., 2012, "Considerations for reporting finite element analysis studies in biomechanics," Journal of Biomechanics, 45(4), pp. 625–633.

[8] Davoodi R., Brown I. E., and Loeb G. E., 2003, "Advanced modeling environment for developing and testing FES control systems," Medical engineering & physics, 25(1), pp. 3–9.

[9] Morrey B. F., 2000, The Elbow and Its Disorders, Saunders, Philadelphia.

[10] Lemay M. A., and Crago P. E., 1996, "A dynamic model for simulating movements of the elbow, forearm, and wrist," Journal of Biomechanics, 29(10), pp. 1319–1330.

[11] Reich J., and J Daunicht W., 2000, "A rigid body model of the forearm," Journal of Biomechanics, 33(9), pp. 1159–1168.

[12] Wei F., Hunley S. C., Powell J. W., and Haut R. C., 2010, "Development and Validation of a Computational Model to Study the Effect of Foot Constraint on Ankle Injury due to External Rotation," Annals of Biomedical Engineering, 39(2), pp. 756–765.

[13] Delp S. L., Loan J. P., Hoy M. G., Zajac F. E., Topp E. L., and Rosen J. M., 1990, "An interactive graphics-based model of the lower extremity to study orthopaedic surgical procedures.," IEEE Transactions on Biomedical Engineering, 37(8), pp. 757–767.

[14] Barker T., Kirtley C., and Ratanapinunchai J., 1997, “Calculation of multi-segment rigid body joint dynamics using MATLAB,” Proceedings of the Institution of Mechanical Engineers, Part H: Journal of Engineering in Medicine, 211(6), pp. 483–487.

[15] Fisk J. P., and Wayne J. S., 2009, “Development and Validation of a Computational Musculoskeletal Model of the Elbow and Forearm,” Annals of Biomedical Engineering, 37(4), pp. 803–812.

[16] Majors B. J., and Wayne J. S., 2011, “Development and Validation of a Computational Model for Investigation of Wrist Biomechanics,” Annals of Biomedical Engineering, 39(11), pp. 2807–2815.

[17] Spratley E. M., and Wayne J. S., 2009, “The design and validation of a computational rigid body model of the elbow.,” Virginia Commonwealth University.

[18] Liacouras P. C., and Wayne J. S., 2007, “Computational Modeling to Predict Mechanical Function of Joints: Application to the Lower Leg With Simulation of Two Cadaver Studies,” J. Biomech. Eng., 129(6), pp. 811–817.

[19] Iaquinto J. M., and Wayne J. S., 2010, “Computational Model of the Lower Leg and Foot/Ankle Complex: Application to Arch Stability,” Journal of Biomechanical Engineering, 132(2), p. 021009.

[20] Elmore K. A., and Wayne J. S., 2012, “Soft tissue structures resisting anterior instability in a computational glenohumeral joint model,” Computer methods in biomechanics and biomedical engineering.

[21] Spratley E. M., and Wayne J. S., 2010, “Computational Model of the Human Elbow and Forearm: Application to Complex Varus Instability,” Ann Biomed Eng, 39(3), pp. 1084–1091.

[22] Chumbley E. M., O’Connor F. G., and Nirschl R. P., 2000, “Evaluation of Overuse Elbow Injuries,” American Family Physician, 61(3), pp. 691–700.

[23] Netter F. H., and Hansen J. T., 2003, Atlas of the Human Anatomy, Icon Learning Systems, Teterboro, N.J.

[24] Gray H., 1918, Anatomy of the Human Body, Lea & Febiger, Philadelphia.

[25] Bryce C. D., and Armstrong A. D., 2008, “Anatomy and Biomechanics of the Elbow,” Orthopedic Clinics of North America, 39(2), pp. 141–154.

[26] Duckworth A. D., Watson B. S., Will E. M., Petrisor B. A., Walmsley P. J., Court-Brown C. M., and McQueen M. M., 2011, “Radial Head and Neck Fractures: Functional Results and Predictors of Outcome.,” The Journal of Trauma: Injury, Infection, and Critical Care, 71(3), pp. 643–648.

[27] Coleman D. A., Blair W. F., and Shurr D., 1987, “Resection of the radial head for fracture of the radial head: long-term follow-up of seventeen cases.,” The Journal of Bone & Joint Surgery, 69-A(3), pp. 385–392.

[28] Van Glabbeek F., Van Riet R. P., Baumfeld J. A., Neale P. G., O'driscoll S. W., Morrey B. F., and An K. N., 2004, "Detrimental effects of overstuffing or understuffing with a radial head replacement in the medial collateral-ligament deficient elbow," The Journal of Bone & Joint Surgery, 86(12), pp. 2629–2635.

[29] Van Riet R. ., Van Glabbeek F., Baumfeld J. ., Neale P. ., Morrey B. ., O'Driscoll S. ., and An K.-N., 2004, "The effect of the orientation of the noncircular radial head on elbow kinematics," Clinical Biomechanics, 19(6), pp. 595–599.

[30] Kuhn S., Burkhart K. J., Schneider J., Muelbert B. K., Hartmann F., Mueller L. P., and Rommens P. M., 2012, "The anatomy of the proximal radius: implications on fracture implant design," Journal of Shoulder and Elbow Surgery, 21(9), pp. 1247–1254.

[31] Schiffern A., Bettwieser S. P., Porucznik C. A., Crim J. R., and Tashjian R. Z., 2011, "Proximal radial drift following radial head resection," Journal of Shoulder and Elbow Surgery, 20(3), pp. 426–433.

[32] Roidis N. T., Papadakis S. A., Rigopoulos N., Basdekis G., Poultsides L., Karachalios T., Malizos K., and Itamura J., 2006, "Current Concepts and Controversies in the Management of Radial Head Fractures," Orthopedics, 29(10), p. 904.

[33] Kumar V., and Wallace W. A., 2012, "Radial head fractures–update on classification and management," Orthopaedics and Trauma, 26(2), pp. 124–131.

[34] Iacobellis C., Visentin A., and Aldegheri R., 2012, "Open reduction and internal fixation of radial head fractures," MUSCULOSKELETAL SURGERY, 96(S1), pp. 81–86.

[35] Wretenberg P., Ericson A., and Stark A., 2006, "Radial head prosthesis after fracture of radial head with associated elbow instability," Archives of Orthopaedic and Trauma Surgery, 126(3), pp. 145–149.

[36] Beredjiklian P. K., Nalbantoglu U., Potter H. G., and Hotchkiss R. N., 1999, "Prosthetic radial head components and proximal radial morphology: A mismatch," Journal of Shoulder and Elbow Surgery, 8(5), pp. 471–475.

[37] Chanlalit C., Shukla D. R., Fitzsimmons J. S., Thoreson A. R., An K.-N., and O'Driscoll S. W., 2011, "Radiocapitellar stability: the effect of soft tissue integrity on bipolar versus monopolar radial head prostheses," Journal of Shoulder and Elbow Surgery, 20(2), pp. 219–225.

[38] Chanlalit C., Shukla D. R., Fitzsimmons J. S., An K.-N., and O'Driscoll S. W., 2012, "The Biomechanical Effect of Prosthetic Design on Radiocapitellar Stability in a Terrible Triad Model," Journal of Orthopaedic Trauma, 26(9), pp. 539–544.

[39] Brabston E. W., Genuario J. W., and Bell J.-E., 2009, “Anatomy and Physical Examination of the Elbow,” Operative Techniques in Orthopaedics, 19(4), pp. 190–198.

[40] Alcid J. G., Ahmad C. S., and Lee T. Q., 2004, “Elbow anatomy and structural biomechanics,” Clinics in Sports Medicine, 23(4), pp. 503–517.

[41] King G. J. W., Zarzour Z. D. S., Patterson S. D., and Johnson J. A., 2001, “An anthropometric study of the radial head: Implications in the design of a prosthesis,” The Journal of Arthroplasty, 16(1), pp. 112–116.

[42] Caputo A. E., Mazzocca A. D., and Santoro V. M., 1998, “The nonarticulating portion of the radial head: anatomic and clinical correlations for internal fixation,” The Journal of hand surgery, 23(6), pp. 1082–1090.

[43] Van Riet R. P., Van Glabbeek F., Neale P. G., Bimmel R., Bortier H., Morrey B. F., O’Driscoll S. W., and An K. N., 2004, “Anatomical considerations of the radius,” Clinical Anatomy, 17(7), pp. 564–569.

[44] Rettig A. C., 2003, “Athletic Injuries of the Wrist and Hand,” The American Journal of Sports Medicine, 31(6).

[45] Morrey B. F., Tanaka S., and An K. N., 1991, “Valgus stability of the elbow: a definition of primary and secondary constraints,” Clinical Orthopaedics and Related Research, (265), pp. 187–195.

[46] Reichel L. M., and Morales O. A., 2013, “Gross Anatomy of the Elbow Capsule: A Cadaveric Study,” The Journal of Hand Surgery, 38(1), pp. 110–116.

[47] M.S. Cohen, Schimmel D. R., Masuda K., Hastings H., and Muehleman C., 2007, “Structural and biochemical evaluation of the elbow capsule after trauma,” Journal of Shoulder and Elbow Surgery, 16(4), pp. 484–490.

[48] Morrey B. F., and An K.-N., 1983, “Articular and ligamentous contributions to the stability of the elbow joint,” The American journal of sports medicine, 11(5), pp. 315–319.

[49] Nielsen K. K., and Olsen B. S., 1999, “No stabilizing effect of the elbow joint capsule: a kinematic study.,” Acta Orthopaedica Scandinavica, 70(1), pp. 6–8.

[50] Noda K., Goto A., Murase T., Sugamoto K., Yoshikawa H., and Moritomo H., 2009, “Interosseous Membrane of the Forearm: An Anatomical Study of Ligament Attachment Locations,” The Journal of Hand Surgery, 34(3), pp. 415–422.

[51] Hotchkiss R. N., An K. N., Sowa D. T., Basta S., and Weiland A. J., 1989, “An anatomic and mechanical study of the interosseous membrane of the forearm: pathomechanics of proximal migration of the radius,” The Journal of Hand Surgery, 14(2), pp. 256–261.

[52] Wright T. W., 2001, “Interosseous membrane of the forearm,” Journal of the American Society for Surgery of the Hand, 1(2), pp. 123–134.

[53] Nakamura T., Yabe Y., and Horiuchi Y., 1999, “Functional anatomy of the interosseous membrane of the forearm — dynamic changes during rotation,” Hand Surgery, 4(1), pp. 67–73.

[54] Skahen J. R., Palmer A. K., Werner F. W., and Fortino M. D., 1997, “The interosseous membrane of the forearm: anatomy and function.,” The Journal of Hand Surgery, 22(6), pp. 981–985.

[55] Yi X., Pan J., and Guo X., 2011, “Anatomical and biomechanical study on the interosseous membrane of the cadaveric forearm,” Chinese Journal of Traumatology, 14(3), pp. 147–150.

[56] Agur A. M. R., and Dalley A. F., 2009, Grant’s atlas of anatomy, Lippincott Williams & Wilkins.

[57] Palmer A. K., and Werner F. W., 1981, “The triangular fibrocartilage complex of the wrist- anatomy and function,” Journal of Hand Surgery, 6(2), pp. 153–162.

[58] Kihara H., Short W. H., Werner F. W., Fortino M. D., and Palmer A. K., 1995, “The stabilizing mechanism of the distal radioulnar joint during pronation and supination,” The Journal of Hand Surgery, 20(6), pp. 930–936.

[59] Bottlang M., O’Rourke M. R., Madey S. M., Steyers C. M., Marsh J. L., and Brown T. D., 2000, “Radiographic determinants of the elbow rotation axis: Experimental identification and quantitative validation,” Journal of Orthopaedic Research, (18), pp. 821–828.

[60] Duck T. R., Dunning C. E., Armstrong A. D., Johnson J. A., and King G. J. W., 2003, “Application of screw displacement axes to quantify elbow instability,” Clinical Biomechanics, 18(4), pp. 303–310.

[61] Tanaka S., An K. N., and Morrey B. F., 1998, “Kinematics and Laxity of Ulnohumeral Joint Under Valgus-Varus Stress,” Journal of Musculoskeletal Research, 2(1), pp. 45–54.

[62] Beggs J. S., 1983, Kinematics, Hemisphere Publishing.

[63] Bottlang M., Madey S. M., Steyers C. M., Marsh J. L., and Brown T. D., 2000, “Assessment of elbow joint kinematics in passive motion by electromagnetic motion tracking,” Journal of Orthopaedic Research, (18), pp. 195–202.

[64] Morrey B. F., and Chao E. Y., 1976, “Passive motion of the elbow joint,” J Bone Joint Surg Am, 58(4), pp. 501–508.

[65] Wu G., van der Helm F. C. T., (DirkJan) Veeger H. E. J., Makhsous M., Van Roy P., Anglin C., Nagels J., Karduna A. R., McQuade K., Wang X., Werner F. W., and Buchholz B., 2005, “ISB recommendation on definitions of joint coordinate systems of various joints for the reporting of human joint motion--Part II: shoulder, elbow, wrist and hand,” Journal of Biomechanics, 38(5), pp. 981–992.

[66] Fisk J. P., and Wayne J. S., 2009, “Development and validation of a computational musculoskeletal model of the elbow and forearm,” Annals of biomedical engineering, 37(4), pp. 803–812.

[67] Hounsfield G. N., 1980, “Nobel Award Address: Computed medical imaging,” American Association of Physicists in Medicine, 7(4), pp. 283–290.

[68] Alcid J. G., Ahmad C. S., and Lee T. Q., 2004, “Elbow anatomy and structural biomechanics,” Clinics in sports medicine, 23(4), pp. 503–517.

[69] Ciccone W. J., Hunt T. J., Lieber R., Pedowitz R., Esch J., and Tasto J. P., 2000, “Multiquadrant digital analysis of shoulder capsular thickness,” Arthroscopy: The Journal of Arthroscopic & Related Surgery, 16(5), pp. 457–461.

[70] Voycheck C. A., Rainis E. J., McMahon P. J., Weiss J. A., and Debski R. E., 2010, “Effects of region and sex on the mechanical properties of the glenohumeral capsule during uniaxial extension,” Journal of Applied Physiology, 108(6), pp. 1711–1718.

[71] Bey M. J., Hunter S. A., Kilambi N., Butler D. L., and Lindenfeld T. N., 2005, “Structural and mechanical properties of the glenohumeral joint posterior capsule,” Journal of Shoulder and Elbow Surgery, 14(2), pp. 201–206.

[72] Kaltsas D. S., 1983, “Comparative study of the properties of the shoulder joint capsule with those of other joint capsules.,” Clinical Orthopaedics and Related Research, 173, pp. 20–26.

[73] Hogan M. J., Rupich R. C., Bruder J. B., and Barr L. L., 1994, “Age-related variability in elbow joint capsule thickness in asymptomatic children and adults.,” Journal of Ultrasound in Medicine, 13(3), pp. 211–213.

[74] Fuss F. K., 1991, “The ulnar collateral ligament of the human elbow joint. Anatomy, function and biomechanics.,” Journal of anatomy, 175, p. 203.

[75] Regan W. D., Korinek S. L., Morrey B. F., and An K. N., 1991, “Biomechanical study of ligaments around the elbow joint,” Clinical Orthopaedics and Related Research, 271, pp. 170–179.

[76] Williams G. M., Chan E. F., Temple-Wong M. M., Bae W. C., Masuda K., Bugbee W. D., and Sah R. L., 2010, “Shape, loading, and motion in the bioengineering design, fabrication, and testing of personalized synovial joints,” Journal of Biomechanics, 43(1), pp. 156–165.

[77] Chan S. M. T., Neu C. P., Komvopoulos K., and Reddi A. H., 2011, “The role of lubricant entrapment at biological interfaces: Reduction of friction and adhesion in articular cartilage,” Journal of Biomechanics, 44(11), pp. 2015–2020.

[78] Gear C. W., 1971, Numerical Initial Value Problems in Ordinary Differential Equations, Prentice-Hall, Inc., Englewood Cliffs, NJ.

[79] 2007, “SolidWorks Help Guide.”

[80] Berglund L., Samson M., and An K. N., 1994, “Four Axial Structural and Material test Machine,” Biomed. Sci Instrum., 30, pp. 213–217.

[81] 2006, “Surgical Technique: RHS Radial Head System.”

[82] Pfaeffle H. J., Tomaino M. M., Grewal R., Xu J., Boardman N. D., Woo S. L.-Y., and Herndon J. H., 1996, “Tensile properties of the interosseous membrane of the human forearm,” Journal of Orthopaedic Research, 14, pp. 842–845.

APPENDIX

General Abbreviations

2D	Two-dimensional
3D	Three-dimensional
ADAMS	Automatic Dynamic Analysis of Mechanical Systems
ARHS	Anatomic Radial Head system
CAD	Computer aided design
CoCr	Cobalt chromium
CT	Computer topography
DICOM	Digital Imaging and Communications in Medicine
FEA	Finite element analysis
GSTIFF	Gear stiff integrator
HU	Hounsfield units
ISB	International Society of Biomechanics
MIMICS	Materialise's Interactive Medical Imaging Control System
MRI	Magnetic resonance imaging
MSC	MacNeal-Schwendler Corporation
OFAT	One factor at a time
PMMA	Polymethyl methacrylate
RBM	Rigid body modeling
RHS	Radial head system
ROI	Region of interest
SDA	Screw displacement axis
STL	Stereolithography

Anatomy Abbreviations

AC	Anterior Capsule
ACx	Anterior capsule resected
AL-AD	Annular ligament, anterior distal
AL-AP	Annular ligament, anterior proximal
AL-PD	Annular ligament, posterior distal
AL-PP	Annular ligament, posterior proximal
CP	Coronoid process
CP-r	Coronoid process repaired
DC-AB	Distal capsule, anterior band
DC-PB	Distal capsule, posterior band
DRUJ	Distal radioulnar joint

EJC	Elbow joint complex
EM	Medial epicondyle
EL	Lateral epicondyle
IOM-AB	Interosseous membrane, accessory band
IOM-CB	Interosseous membrane, central band
IOM-DOB	Interosseous membrane, distal oblique band
LCL-r	Lateral collateral ligaments repaired
LCLx	Lateral collateral ligaments excised
LUCL	Lateral ulnar collateral ligament
MCL-A	Medial collateral ligament, anterior
MCL-PA	Medial collateral ligament, posterior, anterior bundle
MCL-PP	Medial collateral ligament, posterior, proximal bundle
MPPRH	Most proximal point of radial head
RCL-A	Radial collateral ligament, anterior band
RCL-C	Radial collateral ligament, central band
RCL-P	Radial collateral ligament, posterior band
RH	Radial head
PC-I	Posterior capsule of shoulder, inferior band
PC-M	Posterior capsule of shoulder, medial band
PC-S	Posterior capsule of shoulder, superior band
TFCC	Triangular fibrocartilage disc

VITA

Cassandra Alan Woodcock was born in February of 1988 and raised on a farm in Chesterfield County, Virginia. She attended Manchester High School where she was a section leader in her show choir as well as a member and leader of a number of honors and special interest organizations. She also participated in school musicals, choreographed a middle school chorus, and contributed to a number of mural projects at her high school, middle school and local elementary schools. Cassandra also attended the summer Regional Governor's School for the Visual and Performing Arts. Her weekends were filled with extracurricular science courses at the Mathematics and Science Center and volunteering at a local hospital in the in-patient physical therapy department.

Upon graduating as salutatorian in June of 2005 she enrolled at Virginia Commonwealth University to study Biomedical Engineering. While in attendance at VCU, Cassandra became actively involved in Theta Tau, a co-ed professional engineering fraternity, as well as the United Methodist campus ministry and the "Notochords" a cappella ensemble. She also participated in a research laboratory through the Virginia Commonwealth University Reanimation Engineering Science Center and volunteered at a local free clinic. Outside of the University, Cassandra was also a member of her church choir and a leader in the Rainbow Girls, a Masonic youth service organization for girls. In May of 2009, Cassandra graduated cum laude with her Bachelor of Science degree as well as minors in biology and chemistry. After a brief summer respite, she returned to Virginia Commonwealth University to pursue a Masters Degree in Biomedical Engineering.